technische universität
dortmund

EXPERIMENTELLE PHYSIK V
FAKULTÄT PHYSIK
TECHNISCHE UNIVERSITÄT DORTMUND

Physik E5

Leptonic and hadronic radiation production in flaring blazars

A theoretical analysis of the temporal development of the emergent synchrotron, gamma-ray and neutrino intensity

Dissertation

zur Erlangung des akademischen Grades eines
Doktors der Naturwissenschaften
(Dr. rer. nat.)

vorgelegt von

Dipl.-Phys. Björn Eichmann

Dortmund, Juni 2012

Contents

Motivation

From a human perspective the Universe is full of questions about its mechanism and while in general theoretical physics tries to find an order in the chaos of phenomena, interface the physical experiments the mathematical patterns with the considered objects. Thereby, physics always operates between the philosophical antipodes of realism and phenomenalism. According to this, the physical answers are still overshadowed by the discrepancy of the unknown relation between the phenomena and the things in itself. Furthermore, astrophysics in particular, mostly deals with a small amount of theory-loaded observations, so that even the phenomena have to be made accessible by a certain approach to the object of observation. Apparently, there seems to be an insuperable gap between an astrophysical observation and the observed object itself. However, the creation of pictures of these objects is still right, when they are according to Hertz (1999) used in a logically self-consistent way, so that the phenomena are a logically necessary consequence of the pictures, as well as an inherently necessary consequence of the pictured objects. Taking Hertz's condition into account the limits of an accurate picture become clear and in the following there need no further distinction to be drawn between an object and its picture. But still this heuristic approach gives not a satisfying solution to the epistemological problem, so that the interested reader is referred to a soon be published monograph by Soler Gil (2012), since this thesis will no longer focus on that gap of explanation.
Being aware of the basic problem of epistemology the astrophysical motivation behind this thesis can be stated by one of the eleven most profound questions that human beings have posed about the cosmos due to the Committee On The Physics Of The Universe (2003): "How do cosmic accelerators work and what are they accelerating". Commonly, the most powerful particle accelerators in the known universe are denoted by active galactic nuclei (AGN) and gamma-ray bursts (GRBs). Here, the particles are expected to gain energies up to 10^{21} eV and subsequently propagate through the Universe, where they interact with intergalactic magnetic fields, matter fields (like molecular clouds) and photon fields (like the cosmic microwave background, CMB) till some are detected by a satellite or a ground-based instrument. The Fig. 0.1 shows a compilation of recent observations of the resulting energy spectrum of energetic charged subatomic particles (i.e. cosmic rays, CRs) that reached the Earth's atmosphere, in which the main constituent ($\sim 85\,\%$ above 1 GeV) are protons. Hence, the isotropic CR flux $F(E) = \mathrm{d}N/\mathrm{d}E$ can be described by a combination of power-laws (Voigt et al., 1999):

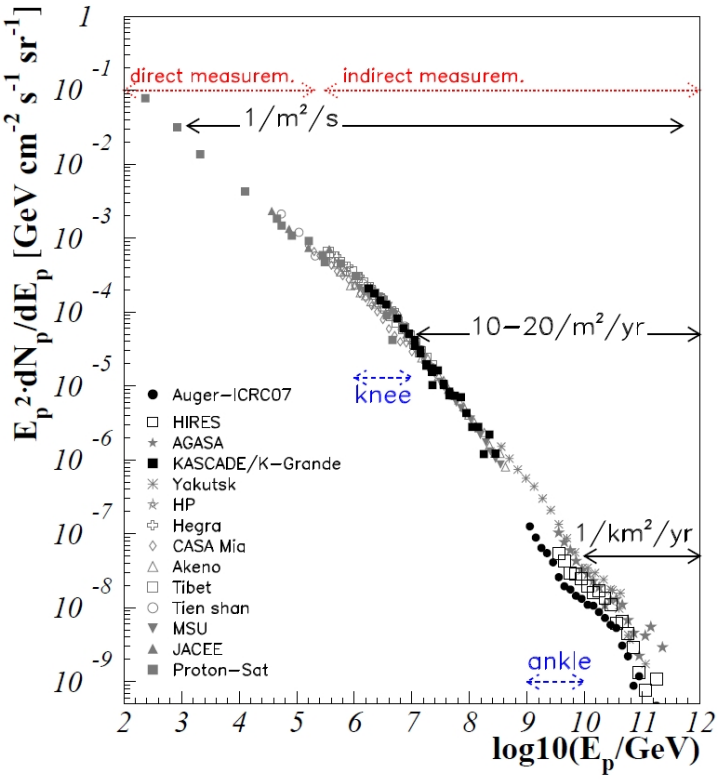

Figure 0.1: The weighted cosmic ray spectrum, where the kind of observation, the kinks in the spectral slope, as well as the approximated particle flux per time and area are indicated (Becker, 2008).

$$F(E) \propto \begin{cases} E^{-2.67}\,, & E < 10^{15.4}\,\mathrm{eV} \\ E^{-3.10}\,, & 10^{15.4}\,\mathrm{eV} < E < 10^{18.5}\,\mathrm{eV} \\ E^{-2.75}\,, & E > 10^{18.5}\,\mathrm{eV}\,. \end{cases} \tag{0.1}$$

The two kinks in the spectral slope are the so-called “knee” and “ankle”, which commonly result from different source populations. So, the CRs below the ankle can be produced within our Galaxy, whereas the particles with higher energies are of extragalactic origin due to isotropy and confinement arguments (Becker, 2008). In addition, recent results of the Pierre Auger Observatory have indicated two further kinks in the highest energetic part of the cosmic ray energy spectrum (The Pierre Auger Collaboration, 2011).
However, the CRs cannot be traced back to their source, as they are deflected by intergalactic magnetic fields and thus, other, uncharged messenger particles (like photons or neutrinos) have to be considered in order to spot the primary particle accelerator (see Fig. 0.2). The most promising AGN with reference to the open questions of cosmic accelerators belong to the blazar class because of their strong non-thermal and highly variable radiation phenomena over a broad frequency range. Nevertheless, the primary particle nature (as well as the radiation mechanism) of the observed radiation is especially at

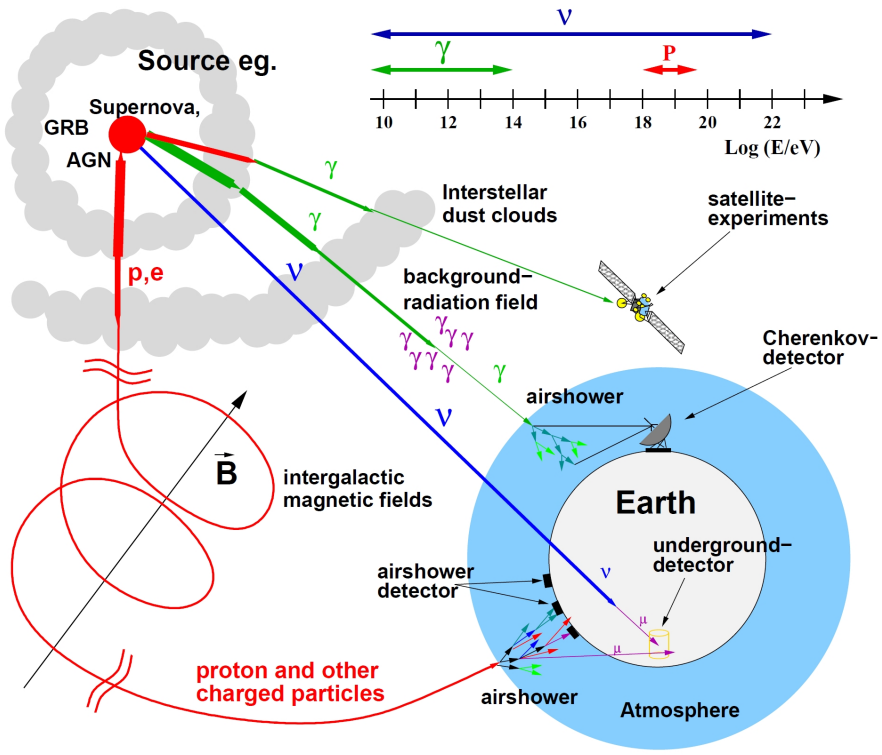

Figure 0.2: Propagation and detection of different messenger particles from high energy cosmic accelerators (Wagner 2004).

γ-ray energies still unclear, as a couple of different approaches lead to accurate results without being mutually exclusive. Hence, for more than one decade there is in particular the leptonic and the hadronic ansatz coexisting, whereas the in 2007 and 2008, respectively, launched AGILE and FERMI satellite missions together with the new generation of ground-based air Cherenkov telescopes such as MAGIC, H.E.S.S. and VERITAS provide unprecedented accurate coverage of our Universe at GeV to TeV photon energies. The new observational opportunities yield an increase in the AGN phenomena and the observations of so-called orphan flares (i. e. a high energy flare without a simultaneous enhancement in the low energy emission) have favored a hadronic explanation, while other data are better described by a leptonic model. In addition, several multifrequency campaigns on flaring blazars have recently shown a strong correlation between the optical, the X-ray and the TeV emission (Aharonian et al., 2009; Donnarumma et al., 2009; Vercellone et al., 2010) and hence the same origin of all this non-thermal radiation suggests itself. But still there is no general unification of the emission scenario of AGN found, so that the detection of extragalactic high energy neutrinos could finally become the smoking gun evidence of a hadronic signature in the emission process. But to date even IceCube, the most sensitive high energy neutrino observatory, that has recently been completed in 2011, has shown in different analysis (R. Abbasi et al., 2011a, 2011b, 2011c) no hint of a significant flux of extragalactic neutrinos. The current status of observations and theoretical predictions of the astrophysical neutrino flux is depicted in Fig. 0.3.

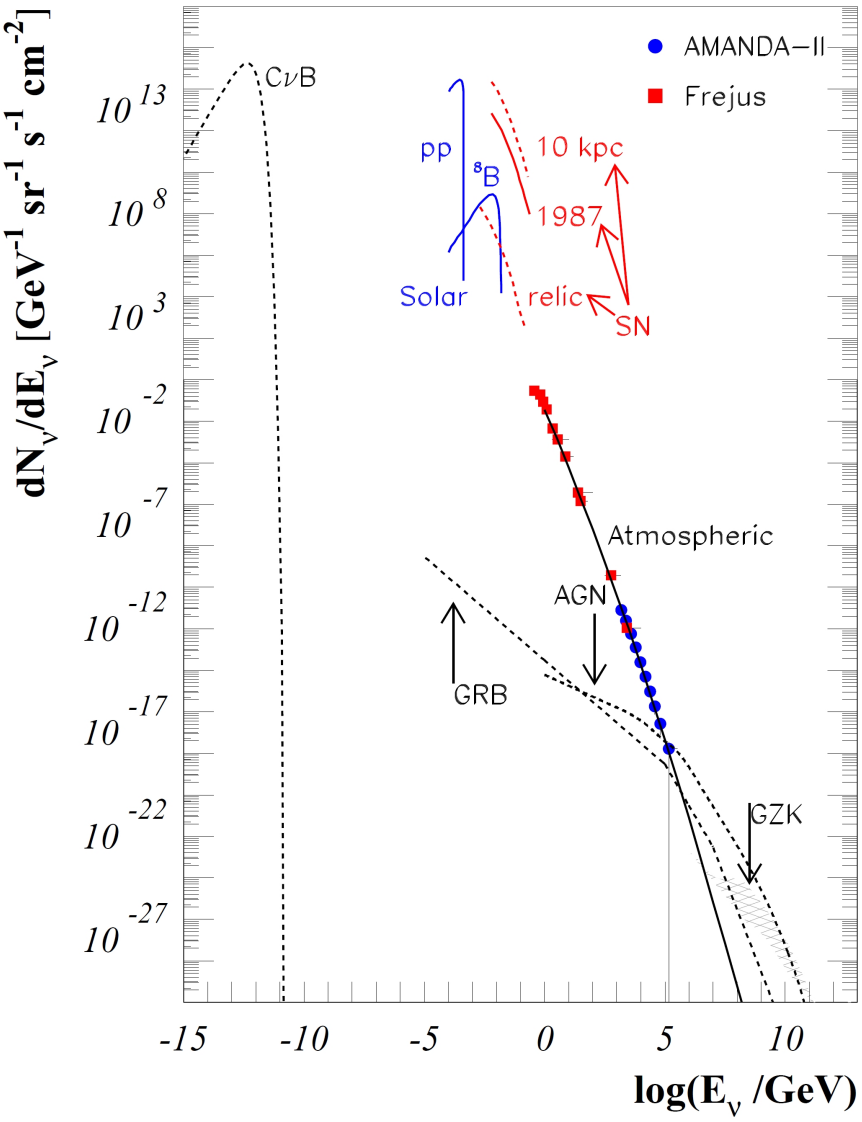

Figure 0.3: The astrophysical neutrino spectrum which has been observed from the sun (blue lines) and the supernova explosion 1987A (red lines), as well as the theoretical flux predictions (dashed lines) from AGN, GRB and the Cosmic Neutrino Background (CνB) which has been decoupled in the Early Universe. In addition, the measured spectrum of atmospheric neutrinos with energies $> 0.1\,\mathrm{GeV}$ and the expected neutrino flux that results from the absorption of protons by the GZK effect is indicated (Becker, 2008).

So, the increasing observational opportunities also require theoretical models which give testable predictions and criteria for exclusion concerning the different emission scenarios. Especially, a reasonably prediction of a time slot for the expected high energy neutrinos from a hadronic emission scenario is a useful tool in order to increase the significance of neutrino observations. Furthermore, every non-thermal radiation model is associated with

a typical and well-known cooling rate relating to the radiating particles, so that another possible distinguishing feature results from the imprint of the cooling scenario in the observed light curves. Summing up, there are four effects determining the temporal behavior of the emission volume: (1) The initial condition of relativistic particles, its subsequent (2) spatial diffusion and (3) continuous cooling processes, as well as (4) propagation effects of the generated particles (i.e. photons and neutrinos, respectively) in the emission region. Consequently, this thesis will develop a model for leptonic and hadronic emission where the effects (1)–(4) are considered. But first the Chap. 1 gives some further introductions into the astrophysical object class of AGN and blazars in particular, as well as the general ideas behind the leptonic and hadronic emission approaches, respectively. Then, the Chap. 2 leads to the general formalisms of the primary particle transport, as well as its possible acceleration and cooling mechanisms. Subsequently, in Chap. 3 the particle transport equation is specified and solved for the considered case of relativistic electrons and protons being picked up into the emission knot of an AGN. The resulting emergent synchrotron intensity which describes the low energy flaring of AGN is investigated in Chap. 4 and gives some useful formulas of its temporal features. The Chap. 5 models the high energy flare of AGN by a leptonic, as well as a hadronic ansatz and finally the time lags of the different approaches are exposed. In addition, both last-mentioned chapters conclude with a comparison between the results and the simultaneous observations of the low and high energy flaring of PKS 2155-304 in July 29–30 2006. The thesis closes with a summary of testable temporal features of a flaring AGN from optical to γ-ray energies and highlights the differences between the considered leptonic and hadronic emission scenarios.

Chapter 1
Introduction

1.1 Active Galactic Nuclei

The name Active Galactic Nuclei (AGN) refers to the compact region at the center of a galaxy, when its energy output exceeds the emission of the host galaxy, i. e. its constituents (stars, dust and interstellar medium), at least in some parts of the electromagnetic spectrum. Except for Gamma Ray Bursts (GRBs) with a luminosity $L_{GRB} \sim 10^{49} - 10^{51}\,\mathrm{erg\,s^{-1}}$ during a few seconds, AGN are the most luminous source class in the sky with $L_{AGN} \sim 10^{44} - 10^{47}\,\mathrm{erg\,s^{-1}}$ on considerably longer time scales (Becker, 2008). About 50 years after the first observations of point sources with an exceptional high luminosity by M. Schmidt (1963) or strong broadened emission lines by C. K. Seyfert (1943), the different phenomena are unified by the current picture of AGN (Antonucci, 1993; Urry & Padovani, 1995), that is sketched in Fig. 1.1. Thus, the different types of objects mainly result from their different orientation to the observer, as well as their luminosity. Due to the compactness and the extreme luminosity, it is commonly believed, that a rotating, super-massive black hole is the central engine of the AGN. The matter close to the black hole forms an accretion disk, which is fed by a dust torus. As a result of the accretion, the matter is transferred to electromagnetic radiation, as well as elementary particles like electrons and protons, that are partially emitted in form of discrete and relativistic plasmoids perpendicular to the disk. In consequence of the strong magnetic fields, the plasma outflow is highly collimated and aligned by two opposite jet structures. However, the jets get decelerated by the ambient medium and expand at a distance of some tens of kilo-parsec to a much wider structure, the so-called lobes or (in case of a more elongated form) plumes, which are very luminous at radio wavelengths. A further constituent of an AGN at a distance of one to ten milli-parsec is the Broad Line Region (BLR), where cold matter is revolving around the black hole with a high angular velocity, so that its emission lines are broad due to strong varying Doppler shifts. At larger distances of several parsec the material is less effected by the central engine and hence the emission lines are narrower, whereby this region is called the Narrow Line Region (NLR). Consequently, it becomes apparent, that the visibility of the different constituents of the AGN and therefore the viewing angle determine different phenomena, i.e. different subclasses of an AGN. Another convenient classification criterion distinguishes between radio-

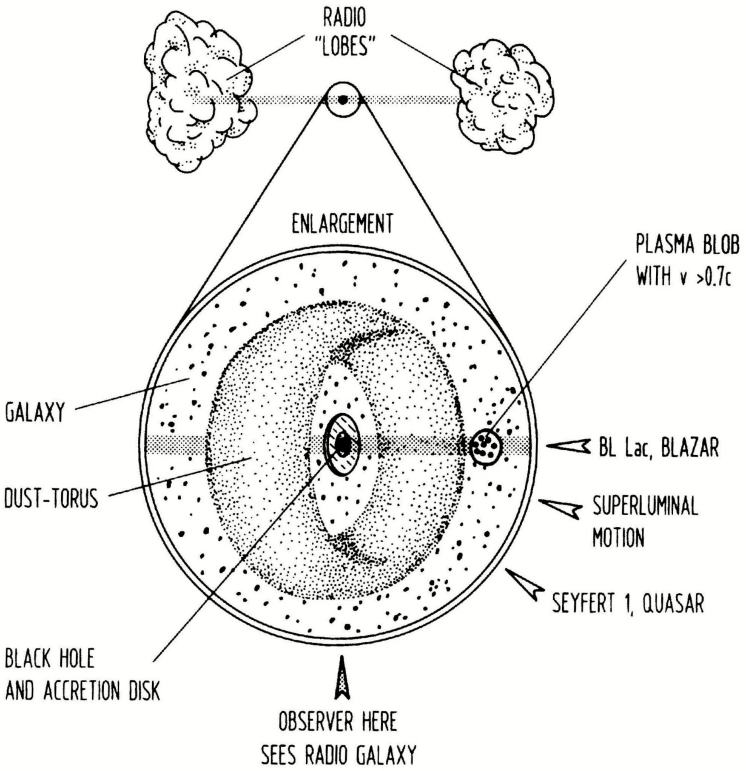

Figure 1.1: Sketch of the current picture of an AGN with its different classifications according to the viewing angle (Schlickeiser, 2002).

quite and radio-loud AGN , so that collectively the so-called "AGN zoo" is obtained, which is shown in Fig. 1.2. In order to attain a detailed insight into the different forms of appearance of an AGN the reader is referred to the monographs of Krolik (1999) or Schneider (2006), since the following examinations will focus on blazars.

Blazar

This subclass of AGN contains the BL Lacertaes (BL Lacs) and Flat Spectrum Radio Quasars (FSRQs), whereby the FSRQs are more luminous, more distant and have stronger emission lines.
Blazars are commonly observed when the angle α between the line of sight and the jet of the AGN is negligible. In this case, the physics of the jet determines the observation of the AGN due to the relativistic beaming of the jet particles and radiation, respectively. Thus, the observed specific intensity $I^*(\nu)$ of the jet radiation is Doppler boosted, according to $I^*(\nu) = \delta^3\, I(\nu/\delta)$ (see Appendix A for more details), where $\delta = [\Gamma(1 - \beta\cos\alpha)]^{-1}$ is the relativistic Doppler factor of an emission knot with a bulk velocity βc and the corresponding Lorentz factor Γ. Apart from measurements of superluminal motion (e. g. Zhang & Fan, 2008), there is an increasing list of observational support for this thesis (Ghisellini, 1993) and in addition, the Doppler enhanced emission yields an observational bias, so that the blazars constitute the largest subclass of the observed AGN.

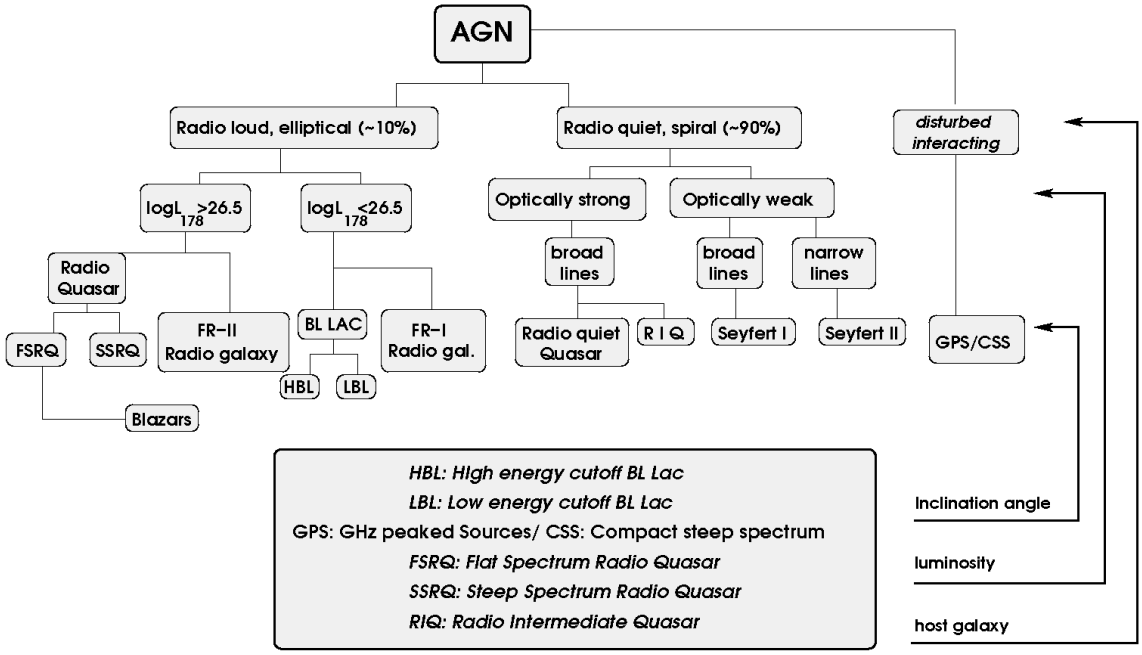

Figure 1.2: Classification schema of AGN (Becker, 2008).

Further characteristics of the blazar class are a high non-thermal emission from radio to high γ-ray frequencies with two distinct bumps in its spectral energy distribution (SED), as well as variability on short timescales (down to minutes; Albert et al., 2007; Aharonian et al., 2007) and a high degree of polarization ($5 - 10\,\%$; Homan, 2005). As a result of the observed variability timescale Δt the maximal extension R of the emission knot is determined by $R \leq \delta\, \Delta t\, c$, since the radiation has to escape the emission volume before it varies in order to observe temporal variability. In reference to the frequencies of the peaks in the SED one distinguishes FSRQs and LBLs (Low-frequency peaked BL Lacs), where the first spectral maximum is at sub-mm to IR wavelengths and the second at GeV energies from the HBLs (High-frequency peaked BL Lacs), which have their maxima about a factor of 10^3 higher. However, the ratio of both peak frequencies stays approximately constant (Fossati et al., 1998). Furthermore, the intrinsic power increases in the sequence HBL $\rightarrow$ LBL $\rightarrow$ FSRQ and hence the properties of these classes can be well-defined by the importance of an external radiation field (Ghisellini et al., 1998).
Although there are some convenient explanations of the different blazar phenomena, the primary nature of the non-thermal emission spectrum is still an unsolved question. It is generally agreed due to the imprint of polarization that the low energy peak in the electromagnetic spectrum of a blazar is a result of the relativistic electrons. But still it is unclear, whether these electrons are of primary nature or what mechanism accelerates them to relativistic energies. Before the details of particle transport are discussed in the subsequent chapter, a brief overview about the current approaches (which can be separated in leptonic and hadronic models) to explain the radiation of an AGN are given in the following.

1.1.1 Leptonic emission models

Using ultra-relativistic electrons (and positrons) to explain the blazar spectrum, a natural correlation between the low and the high energy regime is obtained. On the one hand, the relativistic electrons (or positrons) interact with a magnetic field and consequently emit synchrotron radiation, referring to the observed low energy bump of the SED. On the other hand, the same relativistic electrons (or positrons) transfer momentum to photons with a lower energy by inverse Compton scattering, which yields the high energy bump. This scenario is called synchrotron self Compton (SSC) emission, when the synchrotron photons produced within the jet are the target photons and external Compton (EC) emission in case of an external target photon field from the accretion disk or the BLR.
The observed spectral and variability properties are mostly well described by leptonic emission models and also the sequence HBL $\rightarrow$ LBL $\rightarrow$ FSRQ can be unified by the increasing importance of EC processes (Böttcher, 2007). However, there are still blazar observations (e.g. Böttcher et al., 2009) that are hard to explain by a simple one zone leptonic emission model. And especially the observed orphan flares of 1ES 1959+650 (Krawczynski et al., 2004) or Mkn 421 (Blażejowski et al., 2005) suggest an hadronic emission scenario or a at least a complexer leptonic model. Introducing multiple emission knots is an obvious ansatz, since observations of radio-galaxies have often shown a more structured jet (e.g. Abdo et al., 2010; Aharonian et al., 2009). But the more complex the emission model becomes, the less understanding is gained about the astrophysical object, as the number of free parameters increases and the importance of the additional emission region is uncertain.

1.1.2 Hadronic emission models

In hadronic emission models relativistic protons are a significant constituent of the plasma and influence the non-thermal jet emission. The favored scenarios are inelastic interactions with cosmic matter or photon fields, as well as proton synchrotron radiation. The dominant channel in hadron-hadron and photo-hadron interactions is the production of charged (with a fraction of $\sim 1/3$) and neutral (with a fraction of $\sim 2/3$) pions:

$$p + p \rightarrow \begin{cases} p + p + \pi^0 \\ p + n + \pi^+ \end{cases}, \qquad p + \gamma \rightarrow \begin{cases} \pi^0 + p \\ \pi^+ + n \end{cases}. \tag{1.1}$$

In contrast to the mean neutron lifetime of about 15 minutes is the mean lifetime of the pion less than 1 μs and also its unstable decay product, the muon, has only a mean lifetime of about 2 μs. Hence, in reference to the emission timescales of minutes to hours the decay of pions and muons can be considered as instantaneous when the particles' Lorentz factor is less than $\sim 10^7$. The main decay modes (with a probability of more than 98%) of the generated pions are listed below:

$$\begin{aligned} &\pi^0 \rightarrow 2\gamma\,, \\ &\pi^+ \rightarrow \mu^+ + \nu_\mu \rightarrow\ e^+ + \nu_e + \bar{\nu}_\mu + \nu_\mu\,. \end{aligned} \tag{1.2}$$

Consequently, in both pion production scenarios the generation of gamma-rays has to go along with an enhancement in the neutrino emission, so that a neutrino signal from AGN

is expected, when pion production is a significant interaction mechanism. Furthermore, the generated secondary electrons need to be examined in matters of their influence on the radiation production according to the leptonic emission scenarios of the previous section. In contrast, a pure proton synchrotron model yields no leptonic counterpart emission, as the high energy bump in the blazar's SED results from the gyration of relativistic protons around a magnetic field. But in order to obtain the observed jet luminosities and TeV energies, as well as the rapid time variability, one requires a high magnetic field strength of at least some tens of Gauss and the existence of extremely high energy (EHE; $E \geq 10^{19}$ eV) protons (Aharonian, 2000). However, Sect. 2.2.3 shows that also in case of pion production by photo-hadron interactions with a low-frequency radiation field a high proton energy is needed in order to generate pions.
Using the hadronic emission models one can also differentiate the BL Lac subclasses, since the high energy bump in the SED of HBLs can be explained by dominant proton synchrotron radiation, whereas in LBLs the pion production mechanism becomes significant due to the increasing photon field strength (Mücke et al., 2003).
In a nutshell, the hadronic approach often yields an accurate explanation of the observed AGN phenomena, but also the pure leptonic approach mostly does, so that further distinguishing features in the emitted messenger particles of AGN are needed in order to understand the mechanism of these giant cosmic accelerators.

Chapter 2
Primary particle interactions

2.1 Particle transport equation

In order to obtain an accurate description of the flaring behavior of AGN, as well as suitable conclusions on the primary particles, the transport of the primary particles has to be investigated. The statistical mechanics of charged particles and their mutual interactions by electromagnetic fields have already been treated in great detail by many monographs. So, only the basic ideas are subsequently presented and in order to obtain a detailed insight into the calculations the reader is referred to Schlickeiser (2002).
Starting with a relativistic charged particle of the sort a, located at $\mathbf{r}$ with the spherical coordinates p, $\mu = \cos\theta$, ϕ in momentum space, it interacts with a cosmic plasma and an external magnetic field. Based on the high conductivity of the AGN plasmas the absence of large-scale electric fields can be assumed. Thus, the dynamics of the charged cosmic ray particles are determined by particle-wave interactions with electromagnetic fields, which can mostly be separated into a leading field structure F and a superposed fluctuating field δF. In general, the starting point to determine the collisionless transport of the particles is the Vlasov equation, where the influence of the electromagnetic fields is described by the Lorentz force. Furthermore, the detailed fluctuations of the phase space density f_a are not of interest, but only its average $\mathcal{F}_a = \langle f_a \rangle$ over all members of the ensemble. Using a quasilinear approach, where the fluctuations are of small amplitude, one finally obtains the Fokker-Planck equation including 25 Fokker-Planck coefficients, that account for the random electromagnetic forces of the weak plasma turbulence. However, in most applications this equation cannot be solved and only its diffusion approximation is considered. Here the magnetohydrodynamic phase speed v_{ph} is assumed to be much less than the individual cosmic ray particle speed v, so that the particle is scattered appreciably in gyrophase ϕ and pitch angle μ, whereby the distribution function $\mathcal{F}_a(\mathbf{r}, p, \mu, \phi, t)$ becomes quickly close to an isotropic equilibrium distribution $\mathcal{N}_a(\mathbf{r}, p, t)$. Consequently, one can substitute

$$\mathcal{F}_a(\mathbf{r}, p, \mu, \phi, t) = \mathcal{N}_a(\mathbf{r}, p, t) + \mathcal{G}_a(\mathbf{r}, p, \mu, \phi, t)\,, \tag{2.1}$$

where

$$\mathcal{N}_a(\mathbf{r}, p, t) = \frac{1}{4\pi} \int_0^{2\pi} \mathrm{d}\phi \int_{-1}^{1} \mathrm{d}\mu\ \mathcal{F}_a(\mathbf{r}, p, \mu, \phi, t)\,, \tag{2.2}$$

so that the anisotropic part $\mathcal{G}_a(\mathbf{r}, p, \mu, \phi, t)$ of the distribution function is determined by

$$\frac{1}{4\pi}\int_0^{2\pi} \mathrm{d}\phi \int_{-1}^{1} \mathrm{d}\mu \; \mathcal{G}_a(\mathbf{r}, p, \mu, \phi, t) = 0\,. \tag{2.3}$$

After averaging the Fokker-Planck equation over μ and ϕ, the resulting equation has to be subtracted from the not averaged equation in order to obtain the subsequent diffusion-convection equation

$$\frac{\partial \mathcal{N}_a}{\partial t} - S(\mathbf{r}, p, t) = \Lambda_{\mathbf{r}} \mathcal{N}_a + \Lambda_p \mathcal{N}_a\,. \tag{2.4}$$

Here $S(\mathbf{r}, p, t)$ denotes the source function and the three dimensional spatial operator $\Lambda_{\mathbf{r}}$, as well as the momentum operator Λ_p are defined by

$$\Lambda_{\mathbf{r}} \mathcal{N}_a \equiv \nabla \cdot \left[D(\mathbf{r}, p, t) \nabla \mathcal{N}_a - \mathbf{V} \mathcal{N}_a \right] \tag{2.5}$$

and

$$\Lambda_p \mathcal{N}_a \equiv \frac{1}{p^2}\frac{\partial}{\partial p}\left(p^2 D_p(\mathbf{r}, p, t) \frac{\partial \mathcal{N}_a}{\partial p} + \frac{p^3}{3} \nabla \cdot \mathbf{V}\, \mathcal{N}_a - p^2 \dot{\tilde{p}}\, \mathcal{N}_a \right) - \frac{\mathcal{N}_a}{T(\mathbf{r}, p)}\,, \tag{2.6}$$

respectively. In doing so, the spatial and momentum diffusion coefficients $D(\mathbf{r}, p, t)$ and $D_p(\mathbf{r}, p, t)$, respectively, as well as the effective cosmic ray bulk velocity $\mathbf{V}$ are determined by integrals of different Fokker-Planck coefficients over the pitch angle. Furthermore, $T(\mathbf{r}, p)$ denotes the time scale of catastrophic momentum losses and $\dot{\tilde{p}}$ describes the continuous momentum loss rate. Hence, the momentum convection terms can be merged with

$$\dot{p} = \dot{\tilde{p}} - p\, \nabla \cdot \mathbf{V}/3\,, \tag{2.7}$$

where the influence of the divergence of the bulk velocity due to adiabatic expansion is discussed in Sect. 2.2, as well as the different continuous momentum losses of relativistic electrons and protons.

Dependent on the properties of the plasma turbulence and the background medium arises a specific physical situation, that defines the influence of the different transport parameters of Eq. (2.4). In the following, there is no significant particle acceleration within the emission region assumed, so that momentum diffusion, which refers to the first term in Eq. (2.6), can be neglected. Additionally, the transport of the injected particles is expected to be dominated by spatial parallel diffusion due to the high particle velocities and $T(\mathbf{r}, p)$ has to be much larger than the time scale on which the considered continuous losses operate, in order to obtain significant emission from the radiating particles. Thus, the transport Eq. (2.4) can be simplified to

$$\frac{\partial \mathcal{N}_a}{\partial t} - S(\mathbf{r}, p, t) = \nabla \cdot \left[D(\mathbf{r}, p, t) \nabla \mathcal{N}_a \right] - \frac{1}{p^2}\frac{\partial}{\partial p}\left(p^2 \dot{p}\, \mathcal{N}_a \right)\,. \tag{2.8}$$

According to the separation (2.1), the total number density $N_a(\mathbf{r}, t)$ is defined by

$$N_a(\mathbf{r}, t) \equiv \int \mathrm{d}^3 p \; \mathcal{F}_a(\mathbf{r}, p, \mu, \phi, t) = 4\pi \int \mathrm{d}p \; p^2 \mathcal{N}_a(\mathbf{r}, p, t) = \int \mathrm{d}p \; n_a(\mathbf{r}, p, t), \tag{2.9}$$

as the anisotropic part vanishes by definition (2.3). Subsequently, the isotropic, differential particle density $n_a(\mathbf{r}, p, t)$, as well as the isotropic, differential source term $q(\mathbf{r}, p, t) = 4\pi\, p^2\, S(\mathbf{r}, p, t)$ are considered, so that the kinetic equation (2.8) yields

$$\frac{\partial n_a}{\partial t} = \nabla \cdot \left[D(\mathbf{r}, \gamma, t) \nabla n_a\right] + \frac{\partial}{\partial \gamma}\left(|\dot{\gamma}|\; n_a\right) + q(\mathbf{r}, \gamma, t)\,, \tag{2.10}$$

where the relativistic momentum $p = \gamma m_a c$ is substituted by the Lorentz factor $\gamma \gg 1$ and the algebraic sign of the loss term is already taken into account.
In general, the three-dimensional spatial diffusion Eq. (2.10) is solved by spherical Bessel functions and spherical harmonics, as shown in the Appendix B.1. But due to pitch angle diffusion, the influence of anisotropy quickly decreases with increasing time and thus, further calculations idealize that the distribution of relativistic particles is independent of its solid angle. The temporal and spatial dependence of the diffusion coefficient $D(\mathbf{r}, \gamma, t)$ possibly refer to the variation of the magnetic energy density according to the influence of the kinetic energy density of the radiating particles (Schlickeiser & Lerche, 2008). But in order to obtain an analytical solution of Eq. (2.10), the nonlinear behavior of spatial diffusion is neglected and the magnetic field, as well as its turbulence are assumed to have a constant ratio. However, based on the momentum-dependent Larmor radius of the relativistic particles the spatial diffusion coefficient is still considered to depend on the particles' Lorentz factor. Finally, the transport equation becomes

$$\frac{\partial n_a}{\partial t} = \frac{1}{r^2}\frac{\partial}{\partial r}\left(r^2\, D(\gamma)\, \frac{\partial n_a}{\partial r}\right) + \frac{\partial}{\partial \gamma}\left(|\dot{\gamma}|\; n_a\right) + q_1(\gamma, t)\, q_2(r)\,, \tag{2.11}$$

with the separable source term $q(r, \gamma, t) = q_1(\gamma, t)\, q_2(r)$.

2.2 Particle acceleration and cooling

In order to specify the physical conditions of the transport equation (2.11), the acceleration and cooling processes of the relativistic particles have to be discussed. Generally, an astrophysical system loses its energy by interactions of its constituents or an adiabatic expansion of the system itself. Considering the latter in the simple case of a uniformly expanding sphere of radius $R = 10^{15}\, R_{15}$ cm with an expansion velocity $V_0 = \beta_0\, c$ at the boundary of the emission knot. Thus, the radial velocity distribution inside the sphere at a radius r is determined by $V = V_0(r/R)$, so that $\nabla \cdot \mathbf{V} \simeq 3R^{-1}\, v_0$. Corresponding to Eq. (2.7) the energy loss of the particles within the expanding volume by adiabatic cooling can be approximated by (Longair, 1992)

$$|\dot{\gamma}_{ad}| = \frac{1}{3}\left(\nabla \cdot \boldsymbol{V}\right)\gamma \simeq 3 \cdot 10^{-5}\, \beta_0\, R_{15}^{-1}\, \gamma\, \mathrm{s}^{-1}\,. \tag{2.12}$$

The competing cooling processes according to the interactions of the relativistic particles with its environment are specified in the Sect. 2.2.2 and 2.2.3. While the astrophysical environment sets a distinct cooling scenario, there are several possible acceleration scenarios explaining the relativistic particle energy, as listed by Böttcher (2007). A favored scenario is the acceleration of particles at an integrated or isolated shock front in the jet, according to the so-called first order Fermi acceleration. In order to compete with the radiation

losses, the acceleration process has to be fast. Hence, the particle spectrum obtains a high energy cut-off, instead of a low energy cut-off, which is in contrast to the required cut-offs to model the observed radiation spectra of a blazar (Pohl & Schlickeiser, 2000). A rather general problem of the mechanism of shock acceleration is related to the multiplicity of basic assumptions (e. g. the nature of the magnetohydrodynamic turbulence in the jet, the shock structure itself, etc.), which can hardly be verified, especially in the case of multiple shocks or relativistic shocks with an anisotropic pitch angle distribution.

2.2.1 Pickup model

An alternative explanation based on much less constrains is the pickup model, that describes kinematically the injection of particles into an ultra-relativistic plasma outflow: Due to the conversion of electromagnetic into plasma kinetic energy a plasmoid volume with a particle density N_b escapes with a high Lorentz factor $\Gamma \gg 1$ from the central engine along the magnetic field structure, through intergalactic and interstellar matter with a much lower particle density N_i. In the rest frame of the plasmoid the ambient medium constitutes a relativistic particle beam of mostly electrons and protons parallel to the magnetic field, that aligns the jet and has as a first approximation the constant strength B_0. This antiparallel plasma streams generate two-stream instabilities, which amplify small initial plasma fluctuations to electrostatic and electromagnetic waves. In case of standard AGN jet parameters the beam of ambient electrons and protons is quickly relaxed to a plateau-distribution in parallel momentum by the electrostatic waves (Pohl et al., 2001). On considerably longer (but still short in reference to its emission) time scales

$$\tau_{iso} \simeq 0.02\, N_b^{1/2}\, N_i^{*\,-1}\, \Gamma^{-1}\, \mathrm{s}\,, \tag{2.13}$$

the plateau distributed particles become spatially isotropic by the electromagnetic waves (Pohl & Schlickeiser, 2000) and hence they are picked up by the outflowing plasmoid volume. Consequently, there is no re-acceleration considered and the pickup process is already determined by the initial conditions, e. g. Lorentz factor Γ of the plasmoid, as well as the ambient particle density N_i^* in the rest frame of the plasmoid. In case of a nonuniform ambient interstellar medium $N_i^* \neq const.$ the pickup process is highly variable and thus, can easily explain the observed short time variability of the non-thermal radiation. However, the examinations of Vainio (2004) have shown, that the isotropic particle distribution quickly propagates back to the boundary of the plasmoid volume and leaks outside, while forming a magnetized shock front ahead of the outflow due to the interaction with the ambient medium. This shock front may shield charged particles from free streaming into the plasmoid volume and therefore challenge the simple pickup scenario. But the neutral particles of the partially ionized interstellar medium still stream unaffectedly into the plasmoid volume, where they are ionized according to charge-exchange (electron-impact) interactions with electron-proton (electron-positron) plasma (Gerbig & Schlickeiser, 2007). Therewith, the neutral particles sustain the simple form of the pickup model.
After isotropization at a time τ_{iso} the energy of relativistic protons is about a factor of 1840 higher than the energy of the relativistic electrons (according to their higher mass), so that relativistic proton interactions in the outflowing plasma are attractive candidates for the origin of the high energy radiation of blazars. However, there are about as many

cooling as acceleration scenarios and thus, the commonly discussed interaction processes of cosmic ray electrons and protons are investigated in sequence.

2.2.2 Relativistic electron cooling

The dominant interactions of relativistic electrons with their astrophysical environment are of electromagnetic nature. Hence, there is a clear relation between the observed electromagnetic radiation spectra and the properties of the radiating electrons, which in turn are affected by the corresponding energy loss rate. As these interactions and their exact derivations are the topic of plenty publications since many decades, this thesis will not emanate from the first principles, but concentrate on the link between the continuous energy loss rate of the particles and the resulting electromagnetic radiation.

Synchrotron radiation

In the presence of a magnetic field a charged particle is forced to follow the magnetic field line on a spiral path as a result of the Lorentz force. Thus, the particle 's trajectory is deflected by an angle $\alpha = \lambda_B / r_L$, where λ_B is the coherence length of the magnetic field and r_L is the Larmor radius of the charged particle. In doing so, the particle emits radiation at a beaming angle $\theta \propto \gamma^{-1}$, where γ is the Lorentz factor of the particle. As

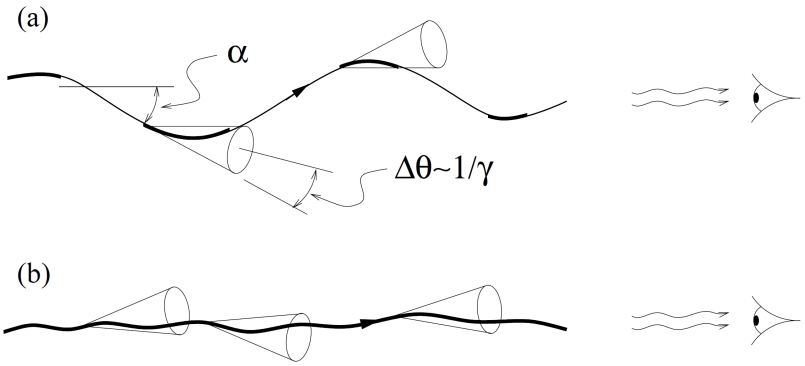

Figure 2.1: Distinguishing features of synchrotron (a) and jitter (b) radiation according to the emission from different points along the particle's trajectory (Medvedev, 2000).

shown in Fig. 2.1 one has to distinguish two different radiation regimes, that depend on the magnetic field structure: In the case (a) of large scale weakly inhomogeneous magnetic fields, the particles deflection angle is much larger than the beaming angle and thus one can average over the pitch angle to derive the so-called synchrotron radiation. However, in the opposite case (b) of small-scale inhomogeneities, the deflection of the particle's trajectory is smaller than the beaming cone and the particle suffers high frequency jittering in perpendicular direction. The resulting jitter radiation occurs in γ-ray burst (GRB) shocks where $\lambda_B \sim 10^2$ cm (Dermer, 2009), whereas the magnetic field in the jet of an AGN is commonly supposed to be less inhomogeneous, so that subsequently the synchrotron radiation is in the focus.

Here a single relativistic particle with a mass m produces a broad continuum of synchrotron photons with a frequency ν, which can be described by an integral over the modified Bessel function of the second kind $K_{5/3}(x)$. An accurate approximation of the pitch angle averaged spectral synchrotron power in vacuum (Crusius & Schlickeiser, 1986, 1988) yields

$$P_s(\nu,\gamma) \simeq P_0 \left(\frac{\nu}{\nu_s\gamma^2}\right)^{\frac{1}{3}} \exp(-\frac{\nu}{\nu_s\gamma^2}) \,, \tag{2.14}$$

where $P_0 = 2.647 \times 10^{-10}\,\mathrm{eV\,s^{-1}\,Hz^{-1}}$. Below the characteristic frequency

$$\nu_c = \nu_s\,\gamma^2 = 3eB\gamma^2/(4\pi mc) \tag{2.15}$$

the spectral power exhibits a $\nu^{1/3}$–dependency, whereas for $\nu \gg \nu_s\gamma^2$ the synchrotron power cuts off exponentially and becomes negligibly small. Integrating the power spectrum (2.14) over all frequencies ν the pitch angle averaged synchrotron losses in the ultra-relativistic limit $\gamma \gg 1$ yields

$$-\dot{\gamma}_{syn} = \frac{4}{3}\,\frac{\sigma_T\,U_B}{m_e c}\left(\frac{m_e}{m}\right)^3 \gamma^2\,\mathrm{s^{-1}} \,, \tag{2.16}$$

with the energy density $U_B = B^2/8\pi$ of the magnetic field of strength B and the Thomson cross-section $\sigma_T = 6.65 \cdot 10^{-25}\,\mathrm{cm^2}$. Apparently, the synchrotron cooling is most efficient in the case of light charged particles, like electrons.
According to Schlickeiser & Crusius (1988) this energy loss rate is accurate at a Lorentz factor $\gamma \gg \gamma_R$ and exponentially damped when $\gamma \ll \gamma_R$, where

$$\gamma_R = 2.1 \cdot 10^{-3}\,(N_b/1\,\mathrm{cm^{-3}})^{1/2}\,(B/1\,\mathrm{G})^{-1} \tag{2.17}$$

denotes the Razin-Tsytovich Lorentz factor in a random magnetic field. But also in the Razin-Tsytovich regime the modification of Eq. (2.16) has no influence on the total energy loss rate, as the energy losses by Coulomb, bremsstrahlung or inverse Compton scattering are mostly dominant. Starting with the latter, these interaction process will be investigated in turn.

Inverse Compton radiation

The interaction of a single electron at rest with a photon was in mathematical detail first explained by Arthur Holly Compton in 1923. However, in the case of relativistically moving electrons the energy exchange is inverted and the electron transfers a part of its kinetic energy to the lower energetic (compared to the rest mass of the electron) target photon, which is accordingly scattered to a higher frequency. Hence, this so-called inverse Compton (IC) scattering may constitute a crucial source of high energy photons, as pointed out in Sect. 1.1.1.
Here a spatially isotropic particle distribution is considered and thus, the probability that an electron with the Lorentz factor γ scatters a photon of energy ϵ up to an energy E_γ is given by the differential cross-section (Blumenthal & Gould, 1970)

$$\sigma_{IC}(E_\gamma,\epsilon,\gamma) = \frac{3\sigma_T}{4\epsilon\gamma^2}\,G(q,\Gamma_e)\,\mathrm{cm^2\,eV^{-1}} \,, \tag{2.18}$$

with

$$G(q, \Gamma_e) = 2q \ln q + (1 + 2q)(1 - q) + \frac{(\Gamma_e q)^2 (1 - q)}{2(1 + \Gamma_e q)} , \tag{2.19}$$

where

$$\Gamma_e = \frac{4\epsilon\gamma}{m_e c^2} \text{ and } q = \frac{E_\gamma}{\Gamma_e(\gamma m c^2 - E_\gamma)} . \tag{2.20}$$

Due to the kinematics of this process the range of values is confined by

$$0.25\,\gamma^{-2} \leq q \leq 1 . \tag{2.21}$$

Using the cross-section (2.18) the IC power of a single relativistic electron in a target photon field of differential number density $n_{ph}(\epsilon, \boldsymbol{r})$ is determined by (Schlickeiser, 2002)

$$P_{IC}(E_\gamma, \gamma, \boldsymbol{r}) = c\, E_\gamma \int_0^\infty \mathrm{d}\epsilon\, n_{ph}(\epsilon, \boldsymbol{r})\, \sigma_{IC}(E_\gamma, \epsilon, \gamma)\, \mathrm{erg\,s^{-1}\,eV^{-1}} . \tag{2.22}$$

The resulting energy loss of the relativistic electrons is calculated by integration of the IC power (2.22) over all scattered photon energies E_γ. In order to obtain an antiderivative the calculations are in the following restricted by the Thomson limit ($\Gamma_e \ll 1$), so that the energy loss is accurately approximated by

$$-\dot{\gamma}_{IC} \simeq \frac{4}{3} \frac{\sigma_T\, U_{ph}(\boldsymbol{r})}{m_e c}\, \gamma^2\, \mathrm{s^{-1}} , \tag{2.23}$$

with the target photon energy density

$$U_{ph}(\boldsymbol{r}) = \int_0^\infty \mathrm{d}\epsilon\, \epsilon\, n_{ph}(\epsilon, \boldsymbol{r}) . \tag{2.24}$$

Here the loss term (2.23) shows the same γ^2-dependence as the synchrotron radiation losses (2.16), whereas in the extreme Klein-Nishina limit, i. e. $\Gamma_e \gg 1$, the IC scattering loss rate increases only with $\ln \gamma$.

Non-thermal bremsstrahlung

In the case of non-thermal bremsstrahlung cooling a relativistic electron of energy $E = \gamma m_e c^2$ is deflected by the Coulomb potential of the atoms, ions or molecules in the traversed medium and emits a γ-ray of energy E_γ. The scattering properties of the electrostatic target are described by the scattering functions $\phi_1(\Delta)$ and $\phi_2(\Delta)$, which depend on the energy-dependent parameter

$$\Delta = \frac{E_\gamma m_e c^2}{4\alpha E(E - E_\gamma)} . \tag{2.25}$$

In terms of these functions (listed in Tab. 2.1) the differential cross-section for the non-thermal bremsstrahlung interaction, as first derived by Bethe & Heitler in 1934, yields

$$\sigma_B(E_\gamma, E) = \frac{3\alpha\sigma_T}{8\pi} \left[\left(1 + (1 - E_\gamma/E)^2\right) \phi_1 - \frac{2}{3}(1 - E_\gamma/E)\phi_2 \right] \mathrm{cm^2\,eV^{-1}}, \tag{2.26}$$

with the fine structure constant $\alpha = 1/137.037$. When an unshielded charge Ze is the target one obtains (Blumenthal & Gould, 1970) $\phi_1 \simeq \phi_2 \simeq Z^2\phi_u$ (see Tab.2.1), where

$$\phi_u = 4 \ln\left[\frac{2E}{m_e c^2}\left(\frac{E-E_\gamma}{E_\gamma}\right)\right] - 2 \tag{2.27}$$

describes the scattering by a proton or an electron. In the case of a general atom the scattering functions become more complex due to the shielding effect that reduces the cross-section for small Δ. However, at large Δ the scattering system becomes unshielded, so that the expression (2.27) is convenient.
Hence, the spontaneously emitted non-thermal bremsstrahlung power of a charged particle that traverses a medium with j different atoms, ions or molecules with the number density N_j yields (Schlickeiser, 2002)

$$P_B(E, E_\gamma) = c\, E_\gamma \sum_j N_j\, \sigma_{B,j}(E, E_\gamma)\, \mathrm{erg\,s^{-1}\,eV^{-1}}\,. \tag{2.28}$$

In order to obtain the bremsstrahlung cooling of a single relativistic electron one has to integrate the power (2.28) over all photon energies E_γ, but an explicit expression is only derived in the limiting cases of strong-shielding ($\Delta \ll 1$) and weak-shielding ($\Delta \gg 1$) limits. Consequently, one obtains for an overall neutral and completely ionized plasma the energy loss rate

$$-\dot{\gamma}_B = \frac{3\alpha c \sigma_T}{2\pi}\gamma\left(\ln\gamma + \ln 2 - \frac{1}{3}\right)\sum_j N_j\, Z_j(Z_j+1)\,\mathrm{s^{-1}} \quad \text{(weak-shielding)}\,. \tag{2.29}$$

Beyond this plasma conditions the expression is still appropriate for $\gamma \lesssim 30/Z$. However, in the strong-shielding limit ($\gamma \gtrsim 30/Z$) the neutral components of the medium have constant scattering functions with $\phi_{1,j} \simeq \phi_{2,j} \simeq \phi_j$, as seen in Tab.2.1 and thus the energy loss rate yields

$$-\dot{\gamma}_B = \frac{3\alpha c \sigma_T}{8\pi}\gamma \sum_j N_j\, \phi_j\, \mathrm{s^{-1}} \quad \text{(strong-shielding)}\,. \tag{2.30}$$

Only at small particle energies the difference between the equation (2.29) and (2.30) becomes significant. So, in contrast to the previous energy loss rates, the non-thermal bremsstrahlung energy loss rate basically depends linearly on the Lorentz factor γ.

Excitation- and Ionization losses

A relativistic particle of energy $E = \gamma mc^2$, which traverses a medium of atomic matter or fully ionized plasma transfers a part of its kinetic energy to the particles of the medium. In atomic matter the energy loss results from the excitation and ionization of the bound atomic levels. Whereas the energy loss in a plasma arises from the energy gain of individual plasma constituents (especially the electrons of particle density N_e) by scattering, as well as the excitation of plasma oscillations, when the particle energy $E \geq h\nu_p$, where $\nu_p = (N_e e^2/\pi m_e)^{1/2}$ is the plasma frequency.

Table 2.1: The scattering function ϕ_u for a proton (or electron), as well as ϕ_1 and ϕ_2 when the scattering system is H, He^+ or He (Blumenthal & Gould, 1970).

Δ	ϕ_u	$\phi_{1,H}$	$\phi_{2,H}$	ϕ_{1,He^+}	ϕ_{2,He^+}	$\phi_{1,He}$	$\phi_{2,He}$
0	∞	45.79	44.46	∞	∞	134.60	131.40
0.01	33.33	45.43	44.38	113.50	111.14	133.85	130.51
0.05	26.89	44.11	43.65	105.67	104.13	130.86	129.26
0.1	24.12	42.64	42.49	101.28	100.34	127.17	126.76
0.5	17.68	34.97	34.93	84.90	84.87	104.60	105.21
1	14.91	29.97	29.78	74.00	73.72	89.94	89.46
5	8.49	18.09	17.28	44.66	43.04	54.26	51.84
10	5.70	13.65	12.41	32.99	30.52	40.94	37.24

Consequently, the energy loss depends, like in the case of bremsstrahlung, on the traversed medium, so that the energy loss rate of a relativistic electron yields (Schlickeiser, 2002)

$$-\dot{\gamma}_C = \frac{3}{4} c\sigma_T N_e \left(\ln\gamma + 2\ln\frac{m_e c^2}{h\nu_p} \right) \mathrm{s}^{-1} \quad \text{(in a plasma)} \tag{2.31}$$

and

$$-\dot{\gamma}_C = \frac{9}{4} c\sigma_T \sum_j N_j Z_j \left(\ln\gamma + \frac{2}{3}\ln\frac{mc^2}{\langle\Delta E\rangle_j} \right) \mathrm{s}^{-1} \quad \text{(in atomic matter)}\,, \tag{2.32}$$

respectively. Here $\langle\Delta E\rangle_j$ denotes the average energy to excite a bound electron of the atomic species j. Thus, in both cases there is only a logarithmic energy dependence and the energy loss rate is basically independent of γ.
The traversed medium becomes heated by the interactions and therefore emits thermal radiation, so that there is an indirect link between the thermal emission and the relativistic electrons. Another significant source to heat the cosmic medium are elastic interactions with relativistic protons, which will be among others discussed in the following section.

2.2.3 Relativistic proton cooling

The previous section has shown that the point-like electromagnetic energy losses of relativistic electrons involve the Thomson cross-section σ_T, which is proportional to the square of the radius of the radiating electron. According to the bigger proton mass m_p the cross-section of electromagnetic interactions of a proton is about a factor of $(m_e/m_p)^2$ smaller, so that these interactions can be neglected in most of the astrophysical applications.
However, some of the observed γ-ray spectra of AGN (like Mrk 501 or Mrk 421) are also well described by a proton synchrotron emission model (Mücke & Protheroe, 2001), when a high magnetic field strength, as well as high particle Lorentz factors are assumed. Referred to Eq. (2.16) the relativistic protons are cooled down about a factor $(m_p/m_e)^3 \simeq 6 \cdot 10^9$ less than electrons, when both particle species have the same Lorentz factor. Furthermore, the characteristic frequency ν_c of synchrotron radiation is by a factor m_p/m_e smaller for protons than for electrons. But using significant particle acceleration the balance of shock

acceleration and synchrotron losses yields the ratio $\gamma_{p,max}/\gamma_{e,max} \geq m_p/m_e$ (Mücke & Protheroe, 2001) of the maximal Lorentz factor of protons and electrons. Therefore, the maximal synchrotron emission of the relativistic protons is nevertheless expected at much higher energies than the emission of relativistic electrons. However, these ultra-relativistic protons are at the same time harder to confine in the emission region, since their Larmor radius is proportional to the particles' momentum. In addition, an efficient particle acceleration within the emission region is needed (but in this thesis excluded) in order to obtain a sufficiently high Lorentz factor of the protons and therefore significant synchrotron losses.
As a consequence, the remaining hadronic interaction processes are collisions with cosmic matter (i. e. mostly protons and α particles) and photon fields. In the general case of inelastic collisions in the center-of-momentum system, the two colliding particles a and b with the masses m_a and m_b, as well as the four-momenta $P_a = (\epsilon_a/c, \boldsymbol{p}_a)$ and $P_b = (\epsilon_b/c, \boldsymbol{p}_b)$ have to satisfy the threshold energy relation

$$\epsilon_a \epsilon_b - \boldsymbol{p}_a \boldsymbol{p}_b c^2 = m_a m_b c^4 + \Delta m c^4 \left(m_a + m_b + \Delta m/2\right) \tag{2.33}$$

in order to create particles with a mass difference Δm. When both incoming particles have non-zero masses the relation yields

$$\gamma_a \gamma_b - \sqrt{(\gamma_a^2 - 1)(\gamma_b^2 - 1)}\, \cos\theta = 1 + \Delta m \left(\frac{1}{m_a} + \frac{1}{m_b} + \frac{\Delta m}{2 m_a m_b}\right) , \tag{2.34}$$

whereas in case of particle-photon collision ($m_b = 0$), one obtains

$$\epsilon_b \left(\gamma_a - \sqrt{\gamma_a^2 - 1}\, \cos\theta\right) = \Delta m c^2 \left(1 + \frac{\Delta m}{2 m_a}\right) . \tag{2.35}$$

Here θ denotes the particles' collision angle in the lab-system.

Interactions with photon fields

There are commonly two important proton-photon interaction scenarios in astrophysical environments, which are on the one hand, pair production (especially e^+e^-) in the field of the proton and on the other hand, photo-hadron (mostly photo-pion) production. Assuming an isotropic photon distribution in space and a mean photon energy $\langle\epsilon\rangle$, the minimum threshold Lorentz factor γ_{min} results from head-on collisions ($\theta = \pi$). Thus, the e^+e^--production threshold yields with Eq. (2.35)

$$\gamma_{min}^{e^+e^-} \simeq m_e c^2 / \langle\epsilon\rangle \tag{2.36}$$

and the minimal Lorentz factor of producing K pions with a mass m_π becomes

$$\gamma_{min}^{\gamma\pi} \simeq \frac{K m_\pi c^2}{2\langle\epsilon\rangle} \left(1 + \frac{K m_\pi}{2 m_p}\right) . \tag{2.37}$$

Both interaction processes have already been treated in detail by Blumenthal (1970), Chodorowski et al. (1992) and Sikora et al. (1987), respectively, whereon the interested reader is referred, since this thesis limits itself in the following to the energy losses of these

interactions without the associated derivation.
A prominent astrophysical application of the photo-pair production is the interaction of cosmic ray protons with a blackbody radiation field, like the cosmic microwave background. Here the energy loss of a proton at its threshold Lorentz factor (2.36) is determined by (Mannheim & Schlickeiser, 1994)

$$-\dot{\gamma}_{e^+e^-} = 2.6{\cdot}10^{-4}\frac{u_\gamma}{\mathrm{erg\,cm^{-3}}}\left(\frac{\langle k_b T\rangle}{\mathrm{eV}}\right)^{-2}\mathrm{s}^{-1} \quad (\text{for } \gamma \simeq \gamma_{min}^{e^+e^-} \text{ in a thermal photon field}), \tag{2.38}$$

whereas in the case of a power-law distributed photon density $n_{ph}(\epsilon) \propto \epsilon^{-2}$

$$-\dot{\gamma}_{e^+e^-} = 2.9\cdot10^{-16}\frac{u_\gamma}{\mathrm{erg\,cm^{-3}}}\gamma^2\,\mathrm{s}^{-1} \quad (\text{for a general } \gamma \text{ in a non-thermal photon field}). \tag{2.39}$$

The photon energy density u_γ is expressed by the Stefan-Boltzman law ($u_\gamma = \sigma T^4$, with $\sigma = 7.56\cdot10^{-15}\,\mathrm{erg\,cm^{-3}\,K^{-4}}$).
EHE protons with a Lorentz factor $\gamma \gg \gamma_{min}^{\gamma\pi}$ lose their energy in interactions with a photon field predominantly by photo-pion production (see Fig. 2.2). In contrast to the previous case, this interaction leads to a significant flux of secondary neutrinos (as already investigated in Sect. 1.1.2). Similar to the previous case, the resulting energy loss of a proton yields (Mannheim & Schlickeiser, 1994)

$$-\dot{\gamma}_{\gamma\pi} = 19\frac{u_\gamma}{\mathrm{erg\,cm^{-3}}}\left(\frac{\langle k_b T\rangle}{\mathrm{eV}}\right)^{-2}\mathrm{s}^{-1} \quad (\text{for } \gamma \simeq \gamma_{min}^{\gamma\pi} \text{ in a thermal photon field}), \tag{2.40}$$

as well as

$$-\dot{\gamma}_{\gamma\pi} = 4.0\cdot10^{-16}\frac{u_\gamma}{\mathrm{erg\,cm^{-3}}}\gamma^2\,\mathrm{s}^{-1} \quad (\text{for a general } \gamma \text{ in a non-thermal photon field}). \tag{2.41}$$

Beyond the thresholds (2.36) and (2.37), the general behavior of the energy loss time of EHE protons in a thermal radiation field is shown in Fig. 2.2.

Interactions with matter fields

Another important collision scenario in astrophysical environments are the interactions with atoms and molecules of the interstellar and intergalactic medium.
First, the inelastic p-p and p-α collisions are investigated which give a hadronic explanation of the γ-ray flares of AGN (see Sect. 1.1.2) according to the production of secondary particles (predominantly charged and neutral pions) and its subsequent decay products. Based on Eq. (2.34) the proton energy threshold $E_{th} = \gamma_{th} m_p c^2 = 1.22\,\mathrm{GeV}$ of hadronic pion production is much lower than in the case of photo-pion production. With Fermi's theory of pion production (Fermi, 1950), the mean Lorentz factor of the generated pions in the rest frame of one of the initial protons yields $\bar{\gamma}_\pi = \gamma_p^{3/4}$, so that the differential

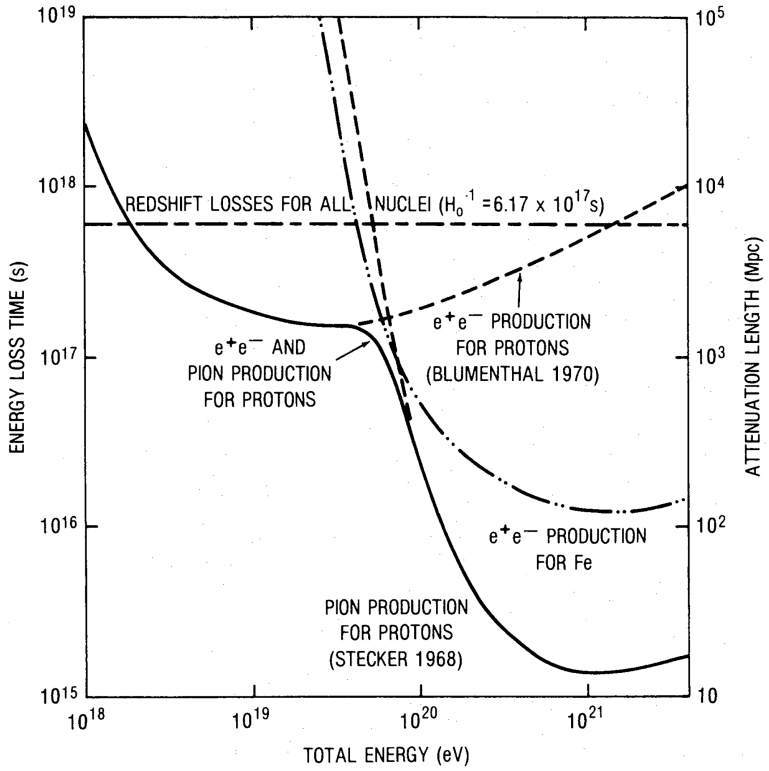

Figure 2.2: The energy loss time and attenuation length of relativistic protons in the 2.7 K microwave background radiation field according to pair production and photo-pion production, in comparison with the redshift expansion loss time. Additionally, the pair production losses of ^{56}Fe is depicted (Puget et al., 1976).

cross section $\sigma^{\pi}_{k,pp}(E_\pi, E_p)$ for the k'th interaction can be approximated by a δ-function (Schlickeiser, 2002)

$$\sum_k \sigma^{\pi}_{k,pp}(E_\pi, E_p) \simeq K \sigma^{\pi}_{pp}(E_p) \frac{\delta(\gamma_\pi - \bar{\gamma}_\pi)}{m_\pi c^2} \,. \tag{2.42}$$

Here K denotes the multiplicity of the reaction and the total inclusive cross-section $\sigma^{\pi}_{pp}(E_p)$ is accurately evaluated by (Kelner et al., 2006)

$$\sigma^{\pi}_{pp}(E_p) \simeq (34.3 + 1.88\,(E_p/1\,\mathrm{TeV}) + 0.25\,(E_p/1\,\mathrm{TeV})^2)\,\left(1 - (E_{th}/E_p)^4\right)^2 \,\mathrm{mb}. \tag{2.43}$$

The pion (i. e. π^0, $\pi^\pm$) power of a single relativistic proton of energy $E_p = \gamma_p m_p c^2$ in a target particle density $N_t(\boldsymbol{r}) = N_{H1}(\boldsymbol{r}) + 2N_{H_2}(\boldsymbol{r})$ that mostly consists of hydrogen is determined by (Schlickeiser, 2002)

$$P(E_\pi, E_p) = 1.30\, c\, \gamma_\pi\, N_t(\boldsymbol{r})\, \sigma^{\pi}_{pp}(E_p)\, \delta(\gamma_\pi - \gamma_p^{3/4})\, H[E_p - E_{th}]\,\mathrm{erg\,s^{-1}\,eV^{-1}}\,. \tag{2.44}$$

The factor 1.30 takes into account the chemical composition of a target medium comparable to the interstellar medium and the Heaviside function H refers to the threshold energy

of this interaction. Laboratory measurements have shown, that the number of generated pions per interaction increases slowly and the multiplicity can generally be approximated by $K \simeq \gamma_p^{1/4}$ (Mannheim & Schlickeiser, 1994). Hence, after integration of the pion power (2.44) over all pion energies E_π, the energy loss of a single relativistic proton by pion production yields

$$-\dot{\gamma}_\pi^{pp} = 4.9 \frac{m_\pi}{m_p}\, c\, N_t\, \sigma_{pp}^{\pi}(E_p)\, H[E_p - E_{th}] \gamma_p \,\mathrm{s}^{-1}\,, \tag{2.45}$$

where the floating point number accounts for the production of the three different π-mesons, as well as the different collision targets in the target medium. When the target medium consists of a thermal plasma of protons and electrons, only proton-proton pion production may occur, so that the factor 4.9 shifts to 3.
Secondly, the excitation of nuclei has to be considered, i. e. the collision of fast protons with α particles or heavier nuclei at rest. The observation of these spectral features reveal a lot about the composition and state of the observed medium, since the excited nucleus emits a characteristic γ-ray due to the nuclear transition to its ground state. However, the resulting energy losses of the relativistic protons are negligibly small compared to the energy losses by Coulomb and ionization interactions, which will be discussed at last.
Like in the case of relativistic electrons the energy loss rate due to Coulomb and ionization processes has to be distinguished by the target medium:
In a fully ionized plasma, the Coulomb collisions are dominated by scattering off the thermal electrons of particle density N_e and velocity $c\beta_e$, where $\beta_e = 0.026\,(T_e/2{\cdot}10^6\,\mathrm{K})^{1/2}$. At large proton velocities βc with $\beta \geq 0.0286\,\beta_e$ the energy loss rate of a single proton yields

$$-\dot{\gamma}_C = 3.3 \cdot 10^{-16}\, N_e\, \frac{\beta^2}{1.3\beta_e^3 + \beta^3}\,\mathrm{s}^{-1} \quad \text{(in a plasma)}. \tag{2.46}$$

In neutral matter, the relativistic protons lose most of their energy by ionization. In case of atomic hydrogen the ionization losses have a maximum at 49 keV, which equals the kinetic energy of the orbit electrons with the velocity $\beta_0\, c = 1.4e^2\hbar^{-1} = 0.01\, c$. For protons with $\gamma_p \leq 918$ the energy loss rate due to ionization of a target gas like the interstellar medium can be approximated by

$$-\dot{\gamma}_{Io} = 1.9{\cdot}10^{-16}\, N_t\, (1{+}0.0185\, \ln\beta\, H[\beta{-}\beta_0])\, \frac{2\beta^2}{\beta_0^3 + 2\beta^3}\,\mathrm{s}^{-1} \quad \text{(in atomic matter)}. \tag{2.47}$$

Comparing the different interaction processes (2.45–2.47) with matter shows that the pion production sets the dominating energy loss (2.45) of relativistic protons with $\gamma \gg 1$ in cosmic matter environments. The energy losses by Coulomb (2.46) and ionization (2.47) effects only have to be taken into account below the energy threshold E_{th} of hadronic pion production.

Chapter 3
Primary particle distribution in the emission knot

In the following all physical quantities are calculated in a coordinate system comoving with the radiation source. Furthermore, a couple of default parameters (dimensionless parameters like R_{15}, etc.) are in the course of this thesis investigated which are set to one, unless otherwise stated, in order to display the results.

3.1 Solution of the particle transport equation

In this section, a general solution of the transport Eq. (2.11) of relativistic electrons (index e) and protons (index p) is given and afterwards, the physical content is specified using the knowledge of the previous chapter for a certain astrophysical environment.
Since the spatial diffusion operator is of Sturm-Liouville type, the kinetic transport Eq. (2.11) is solved in the eigenspace of the operator, where the eigenfunctions are determined by

$$\frac{1}{r^2}\frac{\partial}{\partial r}\left(r^2\frac{\partial f}{\partial r}\right)+\lambda^2 f=0\,. \tag{3.1}$$

Here a general function $f(r)$ is applied which corresponds to the relativistic particle density $n_{e,p}(r,\gamma,t)$. Using two spatial boundary conditions the eigenfunctions, as well as the eigenvalue λ, are well-defined.
On the one hand, there has to be a finite density of particles in the center of the emission knot, i. e.

$$n_{e,p}(r=0,\gamma,t)<\infty\,. \tag{3.2}$$

On the other hand, the particle flux at the boundary surface of the knot is exclusively outward directed. Hence, the radial velocity of the particle has to be positive at $r=R$ and the total leakage flux j_l of particles with relativistic velocity ($v\simeq c$) yields

$$j_l(r=R)=\int_0^1 \mathrm{d}\mu\; c\,\mu\, n_{e,p}=\frac{1}{2}\,c\,n_{e,p}\,. \tag{3.3}$$

This leakage is also described by Fick's law of diffusion

$$j_d = D(\gamma)\,\frac{\partial n_{e,p}}{\partial r}\,, \tag{3.4}$$

so that the second boundary condition becomes

$$\left[\frac{\partial n_{e,p}}{\partial r} + \frac{c}{2\,D(\gamma)}\,n_{e,p}\right]_{r=R} = 0\,. \tag{3.5}$$

Considering the diffusion limit $D(\gamma) \ll c\,R$ the second term dominates the condition and the Eq. (3.5) is well approximated by

$$n_{e,p}(r = R, \gamma, t) = 0\,. \tag{3.6}$$

With the first boundary condition (3.2) the differential equation (3.1) is solved by

$$f(r) = \sum_{k=1}^{\infty} c_k f_k(r) = \sum_{k=1}^{\infty} c_k \frac{\sin(\lambda_k\, r)}{r}\,, \tag{3.7}$$

where f_k is the k'th eigenfunction and c_k denote its coefficient of expansion. Using the second boundary condition (3.5), the eigenvalues λ_k are generally determined by the transcendental equation

$$\frac{\tan(R\lambda_k)}{R\lambda_k} = \frac{1}{1 - \frac{cR}{2\,D(\gamma)}}\,. \tag{3.8}$$

In the case of full diffusion ($D(\gamma) \ll c\,R$) this equation, as well as the constraint (3.6), yield the eigenvalues

$$\lambda_k = \frac{k\pi}{R}\,, \qquad k = 1, 2, 3, \ldots\,. \tag{3.9}$$

Therewith, the orthonormality relation of the eigenfunctions $f_k(r)$ is given by

$$\int_0^R \mathrm{d}r\, r^2\, f_k(r)\, f_i(r) = \frac{R}{2}\,\delta_{ki}\,. \tag{3.10}$$

Consequently, the spatial source term $q_2(r)$, as well as the particle density $n_{e,p}(r, \gamma, t)$ are expanded into the spatial eigenfunctions (3.7) in order to simplify the transport Eq. (2.11):

$$n_{e,p}(r, \gamma, t) = \sum_{k=1}^{\infty} n_k^{e,p}(\gamma, t) \frac{\sin(\lambda_k\, r)}{r} \tag{3.11}$$

and

$$q_2(r) = \sum_{k=1}^{\infty} b_k \frac{\sin(\lambda_k\, r)}{r}\,, \tag{3.12}$$

where due to the Eq. (3.10)

$$b_k = \frac{2}{R}\int_0^R \mathrm{d}r\; q_2(r)\, r\, \sin(\lambda_k r)\,. \tag{3.13}$$

Inserting the expansions (3.11) and (3.12) into the kinetic Eq. (2.11) and using the orthonormality relation (3.10) yields for the particle expansion functions $n_k^{e,p}(\gamma,t)$ the equation

$$\frac{\partial n_k^{e,p}(\gamma,t)}{\partial t} + D(\gamma)\,\lambda_k^2\,n_k^{e,p}(\gamma,t) - \frac{\partial}{\partial\gamma}\left(|\dot{\gamma}|\;n_k^{e,p}(\gamma,t)\right) = b_k\,q_1(\gamma,t)\,. \tag{3.14}$$

The ansatz

$$n_k^{e,p}(\gamma,t) = r_k^{e,p}(\gamma,t)\,\exp\left(\lambda_k^2\int \mathrm{d}\gamma\,D(\gamma)/\,|\dot{\gamma}|\right) \tag{3.15}$$

leads to the equation

$$\frac{\partial r_k^{e,p}(\gamma,t)}{\partial t} - \frac{\partial}{\partial\gamma}\left(|\dot{\gamma}|\;r_k^{e,p}(\gamma,t)\right) = b_k\,q_1(\gamma,t)\,\exp\left(-\lambda_k^2\int \mathrm{d}\gamma\,D(\gamma)/\,|\dot{\gamma}|\right)\,, \tag{3.16}$$

that is solved by

$$r_k^{e,p}(\gamma,t) = b_k\int_{-\infty}^{\infty}\mathrm{d}t'\int_0^{\infty}\mathrm{d}\gamma'\;q_1(\gamma',t')\,\exp\left(-\lambda_k^2\int \mathrm{d}\gamma'\,D(\gamma')/\left|\dot{\gamma}'\right|\right)\;g_k^{e,p}(\gamma,\gamma',t,t')\,, \tag{3.17}$$

where the Green's function $g_k^{e,p}(\gamma,\gamma',t,t')$ is defined by

$$\frac{\partial g_k^{e,p}(\gamma,t)}{\partial t} - \frac{\partial}{\partial\gamma}\left(|\dot{\gamma}|\;g_k^{e,p}(\gamma,t)\right) = \delta(t-t')\,\delta(\gamma-\gamma')\,. \tag{3.18}$$

Substituting $G_k^{e,p}(x,x',t,t') = |\dot{\gamma}|\;g_k^{e,p}(\gamma,\gamma',t,t')$ with

$$x(\gamma) = -\int \mathrm{d}\gamma\;|\dot{\gamma}|^{-1}\;. \tag{3.19}$$

the differential Eq. (3.18) becomes

$$\frac{\partial G_k^{e,p}(x,t)}{\partial t} + \frac{\partial\,G_k^{e,p}(x,t)}{\partial x} = \delta(t-t')\,\delta(x-x')\,. \tag{3.20}$$

Using Laplace transformation (Appendix B.2) the solution of Eq. (3.20) is finally determined by

$$G_k^{e,p}(x,x',t,t') = H[t-t']\,\delta\left(x-(x'+t-t')\right)\,, \tag{3.21}$$

where $H[t-t']$ denotes Heaviside's step function. In order to express the expansion coefficients in terms of the Lorentz factor, the relation

$$\delta(f(\gamma')) = \sum_i \frac{\delta(\gamma'-\gamma_i)}{|f'(\gamma_i)|} \tag{3.22}$$

is applied for the function

$$f(\gamma') = x(\gamma) - (x(\gamma') + t - t') \tag{3.23}$$

and hence

$$g_k^{e,p}(\gamma,\gamma',t,t') = H[t-t']\ |\dot{\gamma}|^{-1} \sum_i |\dot{\gamma}_i|\ \delta(\gamma'-\gamma_i)\,, \tag{3.24}$$

in which γ_i is the i'th zero of $f(\gamma')$. After inserting in Eq. (3.17), the delta and the Heaviside function are passed to account, so that the expansion function (3.15) finally yields

$$n_k^{e,p}(\gamma,t) = b_k\ |\dot{\gamma}|^{-1} \int_{-\infty}^{t} \mathrm{d}t' \sum_i |\dot{\gamma}_i|\ q_1(\gamma_i,t')\, E_k^{e,p}(\gamma,\gamma_i)\,, \tag{3.25}$$

with

$$E_k^{e,p}(\gamma,\gamma_i) = \exp\left[-\lambda_k^2\left(\int \mathrm{d}\gamma_i \frac{D(\gamma_i)}{|\dot{\gamma}_i|} - \int \mathrm{d}\gamma \frac{D(\gamma)}{|\dot{\gamma}|}\right)\right]\,. \tag{3.26}$$

So, in the case of full diffusion the particle transport equation (2.11) is solved without loss of generality by

$$n_{e,p}(r,\gamma,t) = \sum_{k=1}^{\infty} b_k \frac{\sin(\lambda_k\, r)}{r}\ |\dot{\gamma}|^{-1} \int_{-\infty}^{t} \mathrm{d}t' \sum_i |\dot{\gamma}_i|\ q_1(\gamma_i,t')\, E_k^{e,p}(\gamma,\gamma_i)\,. \tag{3.27}$$

Subsequently, the general content of the relativistic particle density (3.27) is specified by the assumed AGN conditions of this thesis, so that further conclusions can be drawn.

3.2 Specification of the particle transport

The previous sections provide an extensive description of charged cosmic rays in an astrophysical environment, which are in this section going to be merged with respect to the underlying AGN model. In doing so, the model should obey the purpose to include known macrophysical details and neglect the rather unknown microphysical details in order to obtain an analytical term of the primary particles. Therefore, the simple pickup model, which has been investigated in Sect. 2.2.1, is used, as well as a spatial and temporal independent diffusion coefficient in the limit of full diffusion. A spherical emission knot of radius $R = 10^{15} R_{15}$ cm is considered that is Doppler boosted towards the observer and consists of a non-relativistic plasma of electrons and protons of density $N_b = 10^{10} N_{10}\,\mathrm{cm}^{-3}$. Using such a high particle density in the emission volume, a significant pion production by p-p interactions (Pohl & Schlickeiser, 2000) is obtained, as well as a diffusive buildup of synchrotron photons in the interior, since the optical depth $\tau = \sigma_T N_b R > 1$.
Furthermore, a magnetic field of strength $B = 1\,b\,\mathrm{Gauss}$, that is randomly distributed on scales much larger than the Larmor radii of the injected particles, is frozen in the highly conducting thermal plasma of the AGN jet.

Specification of the particle source

Since the intergalactic medium mostly consists of ionized hydrogen, the relativistic pickup particles are very likely electrons and protons. The particle density of the plasmoid is

much higher than the density of the ambient medium and thus the plasmoid conditions, i. e. the magnetic field and the background plasma, determine the distribution of the injected particles and the transport equations of the relativistic electrons and protons are not entangled. According to Eq. (2.13) the injected particles are quasi instantaneously isotropized and plateau distributed, so that the resulting particle distribution can be considered in terms of the source term $q_1(\gamma, t)\, q_2(r)$. Therefore, an angular independent $q_2(r)$, as well as (i) an instantaneous injection with plateau distributed energy due to

$$q_1(\gamma, t) = \frac{q_0}{\gamma_0 - 1}\, H[\gamma_0 - \gamma]\, \delta(t - t_0) \tag{3.28}$$

are quite reasonable. In addition, Chap. 4 examines also the case of (ii) a monoenergetic, instantaneous injection

$$q_1(\gamma, t) = q_0\, \delta(\gamma - \gamma_0)\, \delta(t - t_0)\,, \tag{3.29}$$

since it allows some analytical conclusions, as well as the influence of (iii) an instantaneous injection with power-law distributed energy

$$q_1(\gamma, t) = q_0\, \gamma^{\alpha}\, \delta(t - t_0) \tag{3.30}$$

and (iv) a monoenergetic injection of the duration T

$$q_1(\gamma, t) = q_0\, \delta(\gamma - \gamma_0) H[t] H[T - t]\,. \tag{3.31}$$

There is no a priori knowledge of the exact spatial injection region in the emission knot. Thus, the emergent intensity of the low and high energy radiation is generally determined and specified afterwards, so that other spatial injection assumptions can easily be adopted. Here, two illustrative examples are chosen, which result in a high significance of the first eigenvalues and a good approximation by the first 100 terms of the summation in Eq. (3.27).
On the one hand, the mathematical convenient case of ultra-relativistic particles being injected homogeneously in the whole plasmoid volume, i. e. $q_2(r) = 1$ is considered, which yields with Eq. (3.13)

$$b_{k,1} = \frac{2R}{k\pi}(-1)^{k+1}. \tag{3.32}$$

On the other hand, a homogeneous injection within an outer shell of the emission knot of radius $r_1 < R$ is assumed (and compared with the previous results), so that $q_2(r) = H[r - r_1]$ and the expansions coefficient becomes

$$b_{k,2} = -\frac{2R}{k^2\pi^2}\left(k\pi\, \cos(k\pi) + \sin\Big(\frac{k\pi r_1}{R}\Big) - \frac{k\pi r_1}{R}\cos\Big(\frac{k\pi r_1}{R}\Big)\right). \tag{3.33}$$

Specification of the spatial diffusion

Based on the assumed pickup process, the relativistic particles excite electromagnetic turbulences (mostly Alfvén waves) that pitch angle scatter the particles without the loss of momentum. In order to quantify this scattering the magnetic turbulence tensor has to

be specified. Guided by the calculations of Schlickeiser (2002), the wave propagation along the ordered magnetic field has the largest growth rate, which motivates a slab turbulence model, where only the parallel and antiparallel wave vectors in reference to the background magnetic field are non-vanishing. Since most of the microphysical details of the magnetic turbulence in the emission knot of an AGN are unknown, this thesis uses the mathematical convenient case of isospectral turbulence where the magnetic helicities are independent of the wavenumber, as well as a power-law dependent turbulence spectrum with a spectral index $1 \leq q \leq 3$. Consequently, the spatial diffusion coefficient is determined by

$$D(\gamma) = \frac{c\sqrt{1-\gamma^{-2}}}{2\pi(q-1)} \left(\frac{B}{\partial B}\right)^2 R_L(\gamma)^{2-q}\, k_{min}^{1-q}\, F(Z, H_c, \sigma_{f,b})\,, \tag{3.34}$$

with the magnetic turbulence ∂B, the minimum wavenumber k_{min} and the Larmor radius $R_L(\gamma) = m_{e,p}c^2\sqrt{\gamma^2-1}/(eB)$ of the relativistic electrons and protons, respectively. In the special case of $q = 2$ the Eq. (3.34) becomes independent of the Larmor radius and even though a nonlinear behavior of the magnetic field is taken into account, the diffusion coefficient yields a constant, as a similar spatial and temporal dependency of the magnetic field B and its perturbation δB is expected. The function F is determined by the charge Z of the particle, as well as the spectral index q and the helicity parameters which are all independent of the energetic properties of the particle. In the same way the minimum wavenumber k_{min} only refers to the maximum Alfvén wavelength $\lambda_{max} = 2\pi k_{min}^{-1}$, which has to be smaller than the size R of the emission knot. Thus, most of the energy independent parameters of Eq. (3.34) are summarized in the following by a constant mean free path $l_{e,p}$ of the electrons and protons, respectively, with $l_e = (m_e/m_p)^{2-q}\, l_p$, which has to obey the condition of full diffusion, i. e.

$$l_{e,p}\gamma_0^{\beta} \ll R\,. \tag{3.35}$$

Consequently, the spatial diffusion coefficient at relativistic particle energies ($\gamma \gg 1$) yields

$$D(\gamma) = \frac{c\, l_{e,p}}{3}\gamma^{\beta}\,, \tag{3.36}$$

where $\beta = 2 - q$.
Finally, the dominant continuous energy loss process of the relativistic electrons and protons, respectively, in the emission volume of the AGN has to be quantified, so that a distinct distribution of these particles can be given.

Specification of the energy losses of relativistic electrons

First, the significant energy loss of relativistic electrons in an AGN jet is investigated. Since the jet plasma is approximately fully ionized, the excitation and bremsstrahlung losses according to Eq. (2.31) and Eq. (2.29), respectively, have to be considered. Taking a background particle density of $N_b = 10^{10}\, N_{10}\,\mathrm{cm}^{-3}$ into account, the latter loss term yields

$$|\dot{\gamma}_B| = 5.0 \cdot 10^{-7}\, N_{10}\, \gamma\, \mathrm{s}^{-1}\,, \tag{3.37}$$

and the loss rate by excitation processes becomes

$$|\dot{\gamma}_{ex}| \simeq 0.008\, N_{10}\, \mathrm{s}^{-1}\,, \tag{3.38}$$

when the logarithmic energy dependence is neglected in both cases.
Furthermore, the initial synchrotron-self Compton (SSC) energy losses are negligible compared to the synchrotron energy losses if the injection parameter $\alpha_0 = (\gamma_0/\gamma_B)^2$ is less than unity (Schlickeiser et al., 2010), where $\gamma_B = 2.17 \cdot 10^{27}\, R_{15}/Q^{1/2}$. Here a total number of injected particles

$$Q = \int dr^3 \int d\gamma \int dt\; q_1(\gamma, t)\, q_2(r) \tag{3.39}$$

is adopted, so that $Q < Q_B = \left(2.17 \cdot 10^{27}\, R_{15}/\gamma_0\right)^2$ and $\alpha_0 < 1$. Hence, the target photon field of the IC scattering is provided by the external thermal radiation field from the central engine of the AGN, which becomes isotropic at a radial extent R_{sc} with the mean scattering depth τ_{sc} by scattering clouds (Sikora et al., 1994). More details to the external radiation field and its non-radial components are given in Sect. 5.2. In the comoving frame of the emission knot with a Doppler factor $\delta = 10\,\delta_1$ the gyrophase-averaged photon energy density can be approximated by (Dermer & Schlickeiser, 1994, Sikora et al., 1994)

$$U_{ph}(R_{sc}) = \frac{L_{ad}\,\tau_{sc}\,\delta^2}{4\pi\, c\,(R_{sc}^2 + R^2)}\,, \tag{3.40}$$

where L_{ad} denotes the total luminosity emitted by the accretion disk. According to Eq. (2.16) and (2.23) the synchrotron and IC losses show the same γ^2 dependence, so that these losses are merged by

$$|\dot{\gamma}_{SE}| = 1.3 \cdot 10^{-9}\, \gamma^2 \left(b^2 + l_{EC}\right) \mathrm{s}^{-1}\,. \tag{3.41}$$

Here, the EC cooling is defined by

$$l_{EC} = 0.093\, \frac{L_{46}\,\delta_1^2\,\tau_{-2}}{R_{pc}^2 + R_{15}^2}\,, \tag{3.42}$$

with the standard parameters $L_{ad} = 10^{46}\, L_{46}\,\mathrm{erg\ s^{-1}}$, $\tau_{sc} = 10^{-2}\,\tau_{-2}$ and $R_{sc} = 1\, R_{pc}\,\mathrm{pc}$, so that the energy loss rate (3.41) is dominated by synchrotron losses when $b^2 \gg l_{EC}$ and EC losses are significant in the opposite case.
Consequently, the energy losses $|\dot{\gamma}_{ad}|$ and $|\dot{\gamma}_B|$ are smaller than $|\dot{\gamma}_{SE}|$ for a Lorentz factor $\gamma > \gamma_c$, where

$$\gamma_c = \left(387\, N_{10} + 1.5 \cdot 10^4\, \beta_0\, R_{15}^{-1}\right) \left(b^2 + l_{EC}\right)^{-1}\,. \tag{3.43}$$

Thus, the Fig. 3.1a shows that the synchrotron and EC losses, respectively, are dominant at high Lorentz factors $\gamma > \gamma_q$, whereas at $\gamma < \gamma_q$ the relativistic electrons lose their energy by excitation of the non-relativistic background particles. Equalizing the corresponding loss rates (3.41) and (3.38) yields

$$\gamma_q = \sqrt{\frac{D_{ex}}{D_s}} \simeq 2481 \left(b^2 + l_{EC}\right)^{-1/2}\, N_{10}^{1/2}\,, \tag{3.44}$$

with $D_{ex} = 0.008\, N_{10}\, \mathrm{s}^{-1}$ and $D_s = 1.3 \cdot 10^{-9}\ (b^2 + l_{EC})\, \mathrm{s}^{-1}$. Summing up, the significant total energy loss rate of relativistic electrons in the emission knot of the AGN is determined by

$$|\dot{\gamma}^e_{tot}| = D_{ex} + D_s\, \gamma^2\,. \tag{3.45}$$

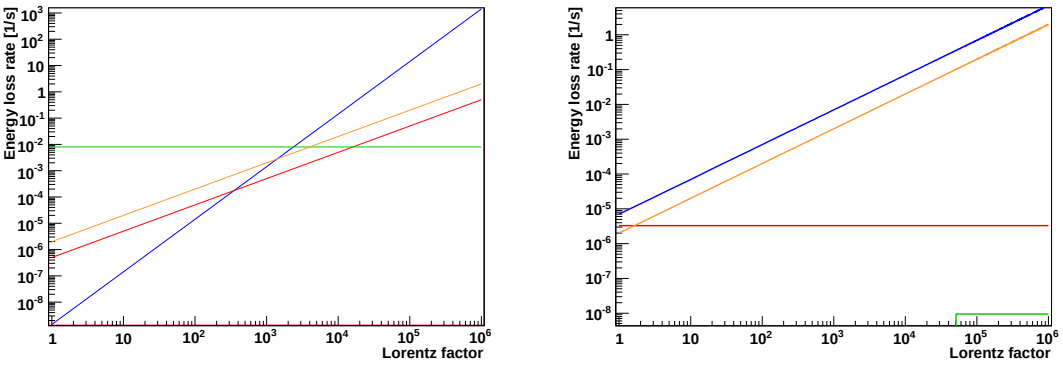

(a) Synchrotron and EC losses (blue), bremsstrahlung losses (red), adiabatic cooling (orange), as well as excitation losses (green) of relativistic electrons

(b) Hadronic pion production (blue), adiabatic cooling (orange), Coulomb losses (red) and photo-pair production at threshold (green) of relativistic protons

Figure 3.1: Energy loss rates of relativistic electrons (a) and protons (b) using the parameters $b = 1$, $l_{EC} = 0.0093$, $N_{10} = 1$, $\beta_0 = 0.1$ and $R_{15} = 1$.

Conclusions to the relativistic electron distribution

Using the total loss rate (3.45) in Eq. (3.19), the root of Eq. (3.23) is determined by

$$\gamma_i \equiv \gamma_t(\gamma, t, t') = \frac{\gamma_q \gamma + \gamma_q^2 \tan(D_s \gamma_q (t - t'))}{\gamma_q - \gamma \tan(D_s \gamma_q (t - t'))} \tag{3.46}$$

and in consideration of the spatial diffusion coefficient (3.36) the Eq. (3.26) yields

$$\begin{aligned} E^e_k(\gamma, \gamma_t) &= \exp\left(\frac{\lambda_k^2\, c\, l_e}{3 D_{ex} (\beta + 1)} \left[\gamma^{\beta+1}\, {}_2F_1\left(1, \frac{\beta+1}{2}; \frac{\beta+3}{2}; \frac{\gamma^2}{\gamma_q^2}\right) \right.\right. \\ &\qquad \left.\left. - \gamma_t^{\beta+1}\, {}_2F_1\left(1, \frac{\beta+1}{2}; \frac{\beta+3}{2}; \frac{\gamma_t^2}{\gamma_q^2}\right) \right] \right) \\ &= \begin{cases} \left(\frac{(\gamma/\gamma_q)^2+1}{(\gamma_t/\gamma_q)^2+1} \right)^{\frac{\lambda_k^2\, c\, l_e}{6\, D_s}}, & \text{for } \beta = 1 \\ \exp\left(\frac{\lambda_k^2\, c\, l_e}{3\, D_s\, \gamma_q} \left[\arctan\left(\frac{\gamma}{\gamma_q}\right) - \arctan\left(\frac{\gamma_t}{\gamma_q}\right) \right] \right), & \text{for } \beta = 0 \\ \left(\frac{(\gamma_q/\gamma_t)^2+1}{(\gamma_q/\gamma)^2+1} \right)^{\frac{\lambda_k^2\, c\, l_e}{6\, D_{ex}}}, & \text{for } \beta = -1\,, \end{cases} \end{aligned} \tag{3.47}$$

where the hypergeometric function ${}_2F_1(a, b; c; z)$ is simplified for an integer β. Defining the timescale

$$\tau_{ul}^{e} = \frac{\pi}{2D_s\,\gamma_q} + t', \tag{3.48}$$

two limiting cases are subsequently discussed: When $t \ll \tau_{ul}^{e}$ the tangent functions in Eq. (3.46) can be approximated by its argument, so that

$$\gamma_t(\gamma, t \ll \tau_{ul}^{e}) \simeq \frac{\gamma}{1-\gamma D_s(t-t')} + \frac{\gamma_q^2 D_s(t-t')}{1-\gamma D_s(t-t')} \simeq \gamma \tag{3.49}$$

and thus $E_k^e(\gamma, \gamma_t = 1) \simeq 1$ at small timescales. However, at later times $t \to \tau_{ul}^{e}$ the tangent functions in Eq. (3.46) diverge and with l'Hôpital's rule one obtains

$$\lim_{t\to\tau_{ul}^{e}} \gamma_t(\gamma, t, t') = -\gamma_q^2/\gamma\,. \tag{3.50}$$

Consequently, $\max(\gamma_t/\gamma) = \gamma_q^2$, as well as $\min(\gamma_t/\gamma) = \gamma_q^2/\gamma_0^2$ and with the full diffusion limit (3.35) the three integer cases of Eq. (3.47) lead to similar results, as shown in Fig. 3.2. Using the energy loss rate (3.45) and the root (3.46) the relativistic electron density (3.27) in the emission volume of the AGN is specified to

$$n_e(r, \gamma, t) = \sum_{k=1}^{\infty} b_k\,\frac{\sin(\lambda_k\, r)}{r}\int_{-\infty}^{t} \mathrm{d}t'\,\frac{1+(\gamma_t/\gamma_q)^2}{1+(\gamma/\gamma_q)^2}\,q_1(\gamma_t, t')\,E_k^e(\gamma, \gamma_t)\,. \tag{3.51}$$

Since this thesis is restricted to the case of full diffusion (3.35), the diffusion coefficient (3.36) has no influence on the distribution of relativistic electrons, so that subsequent calculations are without loss of generality confined by a constant mean free path ($\beta = 0$). Due to the delta function in Eq. (3.24) the timescale of cooling the relativistic electrons down to $\gamma = 1$ is determined by $\gamma' = \gamma_t(\gamma = 1, t, t')$, which results in

$$t - t' = \frac{1}{D_s\gamma_q}\,\arctan\left(\frac{\gamma'-1}{\frac{\gamma'}{\gamma_q}+\gamma_q}\right)\,. \tag{3.52}$$

When $\gamma' > (\gamma_q+1)/(1-1/\gamma_q)$ the argument of the arc tangent function is > 1 and the arc tangent function is accurately approximated by $\pi/2$. Since no reacceleration inside of the emission knots is considered, the Eq. (3.52) refers to the maximal duration of an AGN flare that is generated by relativistic electrons. The variables γ' and t' are mostly defined by the injection assumption $q_1(\gamma', t')$ and in the case of an injection duration $T \ll \pi/(2\,D_s\,\gamma_q)$ the upper limit yields the well-known timescale (see Eq. 3.48)

$$\tau_{ul}^{e} \simeq \frac{\pi}{2\,D_s\,\gamma_q} = \frac{4.9\cdot 10^5\,\mathrm{s}}{(b^2+l_{EC})^{1/2}\,N_{10}^{1/2}}\,. \tag{3.53}$$

At high Lorentz factors where the synchrotron and EC losses, respectively, are dominant, i. e. $\gamma_q \ll \gamma$, the Eq. (3.46) is simplified to

$$\tilde{\gamma}_t(\gamma, t, t') \simeq \frac{\gamma}{1-D_s\gamma\,(t-t')} \tag{3.54}$$

and according to Eq. (3.26) one obtains

$$\tilde{E}_k^e(\gamma \gg \gamma_q, t, t') = \exp\left(-\frac{\lambda_k^2\, c\, l_e\, \gamma^{\beta-1}}{3\, D_s\, (\beta-1)}\left[(1 - D_s\gamma(t-t'))^{1-\beta} - 1\right]\right) . \tag{3.55}$$

As previously shown, the energy dependency of the diffusion coefficient (3.36) is negligible in the full diffusion limit, so that in the mathematically convenient case of $\beta = 0$ the relativistic electron density at $\gamma \gg \gamma_q$ yields

$$\tilde{n}_e(r, \gamma, t) = \sum_{k=1}^{\infty} b_k\, \frac{\sin(\lambda_k\, r)}{r} \int_{-\infty}^{t} \mathrm{d}t'\, \frac{\exp(-\lambda_k^2\, c\, l_e(t-t')/3)}{(1 - D_s\gamma(t-t'))^2}\, q_1(\tilde{\gamma}_t, t') . \tag{3.56}$$

In order to obtain a detailed description of the flare behavior that results from the relativistic electrons, the differential densities (3.51) and (3.56) are used in Chap. 4 to calculate the emergent synchrotron intensity and in Sect. 5.2 to derive the emergent gamma-ray intensity, that results from EC scattering.

Specification of the energy losses of relativistic protons

Finally, the dominant energy loss rate of the injected relativistic protons has to be discussed. Based on the thermal radiation field of the accretion disk with a photon energy $\theta = 10\,\theta_1$ eV the production of K pions by photohadronic interactions occurs with reference to Eq. (2.37) only for ultra-relativistic protons whose minimal Lorentz factor is $\gamma_{min}^{\pi} \simeq 7.3 \cdot 10^6\, K\, \theta_1^{-1}$. As the assumed simple pickup model gains rather small Lorentz factors, the photohadronic pion production is negligible when

$$\gamma_6 < 7.3\, K\, \theta_1^{-1} . \tag{3.57}$$

According to Eq. (2.36) the pair production losses in the field of the relativistic proton has a smaller minimal Lorentz factor of $\gamma_{min}^{e^\pm} \simeq 5.1 \cdot 10^4\, \theta_1^{-1}$ and with the thermal isotropized radiation density (3.40) of the accretion disk the pair production energy loss rate (2.38) for protons at threshold yields

$$|\dot{\gamma}|_{e^\pm}^{p\gamma} \simeq 9.5 \cdot 10^{-9}\, \frac{\delta_1^2\, L_{46}\tau_{-2}}{R_{pc}^2\, \theta_1^2}\, \mathrm{s}^{-1} . \tag{3.58}$$

The proton interactions with the background plasma is determined by pion production and after Eq. (2.45) the loss rate is given by

$$|\dot{\gamma}|_{\pi}^{pp} \simeq D_c\, \gamma\,, \quad D_c = 7 \times 10^{-6}\, N_{10}\ \ \mathrm{s}^{-1}\,, \tag{3.59}$$

when $\gamma > 1.30$. Comparing the adiabatic energy loss rate (2.12) with the particle interaction loss rates (3.58) and (3.59) yields a dominant cooling by hadronic pion production (Fig. 3.1b) at a background particle density

$$N_{10} > 2.7 \cdot 10^{-8}\, \delta_1^2\, L_{46}\tau_{-2}\, R_{pc}^{-2}\, \theta_1^{-1} + 4.3\, \beta_0\, R_{15}^{-1} . \tag{3.60}$$

Since the parameters of AGN jets are rather unknown this thesis subsequently uses parameters which obey the constraints (3.57) and (3.60).

Conclusions to the relativistic proton distribution

The total energy loss of relativistic protons is described by Eq. (3.59), so that the root of Eq. (3.23) yields

$$\gamma_i \equiv \gamma_r(\gamma, t, t') = \gamma \, \exp(D_c \, (t - t')) \tag{3.61}$$

and the Eq. (3.26) is with the spatial diffusion coefficient (3.36) simplified to

$$E_k^p(\gamma, \gamma_r) = \begin{cases} \exp\left(\frac{\lambda_k^2 \, c \, l_p}{3 \, D_c \, \beta} \, (\gamma^\beta - \gamma_r^\beta)\right) , & \text{for } \beta \neq 0 \\ (\gamma/\gamma_r)^{\frac{\lambda_k^2 \, c \, l_p}{3 \, D_c}} , & \text{for } \beta = 0 \, . \end{cases} \tag{3.62}$$

At small timescales where γ_r is close to γ, both cases in Eq. (3.62) can be simplified to similar exponential functions whose arguments are vanishing small in the full diffusion limit (3.35). As shown in Fig. 3.2, the diffusion coefficient consequently has in this limit no influence on the relativistic proton distribution (analogous to the case of relativistic electrons).
Using the previous specifications (3.59), (3.61) and (3.62) the relativistic proton density in the emission knot of the AGN is according to Eq. (3.27) determined by

$$n_p(r, \gamma, t) = \sum_{k=1}^{\infty} b_k \, \frac{\sin(\lambda_k \, r)}{r} \int_{-\infty}^{t} \mathrm{d}t' \, \frac{\gamma_r}{\gamma} \, q_1(\gamma_r, t') \, E_k^p(\gamma, \gamma_r) \, . \tag{3.63}$$

Based on the delta function in Eq. (3.24) the relation $\gamma' = \gamma_r(\gamma = 1, t, t')$ defines the cooling timescale

$$t - t' = \frac{\ln \gamma'}{D_c} \, , \tag{3.64}$$

which also gives the maximal duration τ_{ul}^p of an AGN flare that is generated by the relativistic protons. In the special case of a monoenergetic ($\gamma' = \gamma_0 = 10^6 \, \gamma_6$) particle injection of duration $T \ll \ln \gamma_0 / D_c$ the upper flare limit yields

$$\tau_{ul}^p = \frac{\ln \gamma_0}{D_c} = 2.0 \cdot 10^6 \, N_{10}^{-1} \, (1 + \ln(\gamma_6)/\ln(10^6)) \, \mathrm{s} \, . \tag{3.65}$$

Consequently, an AGN flare generated by relativistic protons can last significantly longer than a flare that is produced by relativistic electrons, when the background particle density $N_{10} < 16.7 \, (b^2 + l_{EC}) \, (1 + \ln(\gamma_6)/\ln(10^6))^2$. Due to the assumed AGN parameters the relativistic protons (3.63) generate gamma rays and high energy neutrinos exclusively by inelastic proton-proton interactions with the background plasma, which will be discussed in detail in Sect. 5.3.

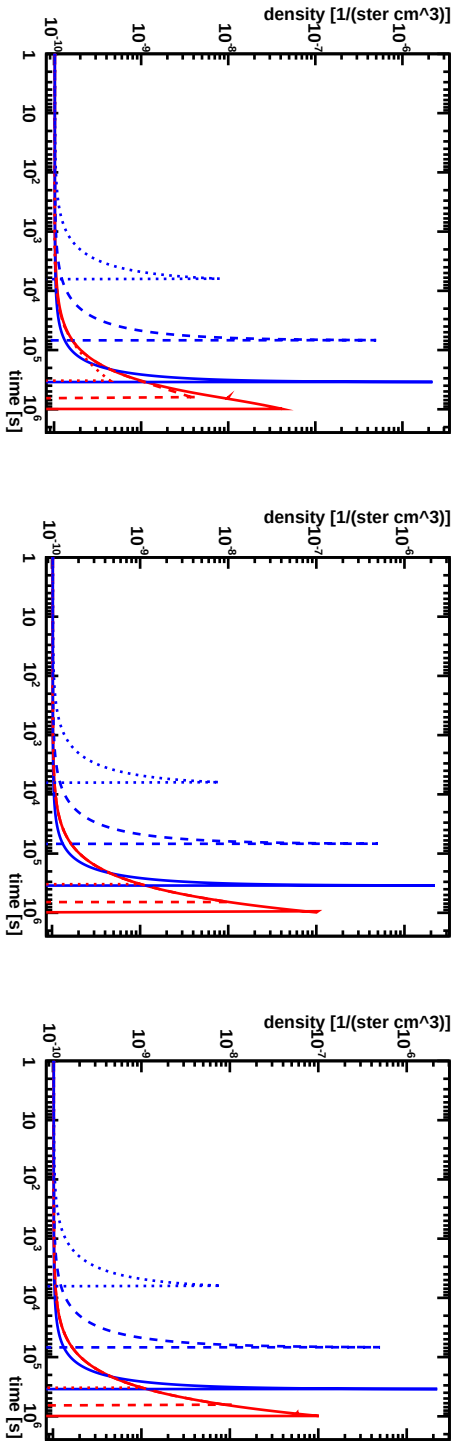

Figure 3.2: Temporal development of the differential number density of relativistic electrons (blue) and protons (red) at $r = 0.1\,R$ in the full diffusion limit, resulting from a spatial homogeneous injection of energetically plateau distributed particles into the whole emission knot. A Lorentz factor of $\gamma = 10^3$ (solid line), $\gamma = 10^4$ (dashed line) and $\gamma = 10^5$ (dotted line) is considered, as well as a spatial diffusion assumption according to $\beta = 1$ (left panel), $\beta = 0$ (middle panel) and $\beta = -1$ (right panel). The remaining parameters are determined by $R_{15} = 1$, $\gamma_6 = 1$, $\gamma_{-4} = 1$ and $b = 1$.

Chapter 4
Modeling low energy flares

The low energy flare of an AGN commonly refers to the synchrotron emission of relativistic electrons. Using the previously derived distribution of primary relativistic electrons (3.51) and (3.56), respectively, the temporal development of the synchrotron flare is examined in this chapter.
In order to give an analytical description of the temporal flare development, the complexity of the problem has to be simplified. At first, a monochromatic approximation of the synchrotron power spectrum is applied, which yields some rough characteristics of the synchrotron flare. Afterwards, the influence of the broadband nature of the synchrotron emission of a single electron is analyzed with respect to the different particle injection assumptions (3.29)–(3.28). In doing so, the considered synchrotron photon energies are confined by $\epsilon > E_q$, where

$$E_q = h\,\nu_s \gamma_q^2 = 1.74 \cdot 10^{-8} \gamma_q^2\,\mathrm{eV} = 0.11\,(b^2 + l_{EC})^{-1}\,N_{10}\,\mathrm{eV}\,, \tag{4.1}$$

so that in a first approach the continuous excitation losses of the relativistic electrons are negligible and the differential electron density of Eq. (3.56) is used. Finally, the emergent synchrotron intensity is examined when the excitation losses as included in Eq. (3.51) are taken into account.

4.1 Spontaneous synchrotron emission coefficient

The gyrating relativistic electrons $n_e(r, \gamma, t)$ in the magnetic field of the emission knot spontaneously emit synchrotron radiation at the beaming angle θ, that is commonly determined by

$$j_s(r, t, \nu, \theta) = \frac{1}{4\pi} \int_1^\infty \mathrm{d}\gamma\, n_e(r, \gamma, t)\, P_s(\nu, \theta, \gamma)\,. \tag{4.2}$$

However, the assumed large-scale (i. e. on length scales of the emission volume) isotropy of the magnetic field leads to an isotropic synchrotron emission on large length scales, so that the pitch angle averaged spectral synchrotron power $P_s(\nu, \gamma)$ of Eq. (2.14) can be used and the spontaneous emission coefficient becomes angular independent. In order to express the

synchrotron emission in terms of the photon energy $\epsilon = h\,\nu$, the relation $j_s(\nu)\,\mathrm{d}\nu = j_s(\epsilon)\,\mathrm{d}\epsilon$ is used so that the differential expression (4.2) is substituted by $j_s(r,t,\epsilon) = j_s(r,t,\nu)/h$. Consequently, the spontaneous synchrotron emission coefficient yields with Eq. (3.51) and (2.14) the general expression

$$\begin{aligned} j_s(r,t,\epsilon) = \frac{P_0}{4\pi\,h}\left(\frac{\epsilon}{\epsilon_s}\right)^{\frac{1}{3}} \int_1^\infty \mathrm{d}\gamma\;\gamma^{-\frac{2}{3}}\;\exp(-\frac{\epsilon}{\epsilon_s\gamma^2})\;\sum_{k=1}^{\infty} b_k\,\frac{\sin(\lambda_k\,r)}{r} \\ \times \int_{-\infty}^{t} \mathrm{d}t'\,\frac{1+(\gamma_t/\gamma_q)^2}{1+(\gamma/\gamma_q)^2}\,q_1(\gamma_t,t')\,E_k^e(\gamma,\gamma_t)\,, \end{aligned} \tag{4.3}$$

where $\epsilon_s = h\,\nu_s = 17.4\cdot 10^{-9}\,b\,\mathrm{eV}$. The energy and time dependent functions γ_t and $E_k^e(\gamma,\gamma_t)$ are defined by Eq. (3.46) and (3.47), respectively.
According to Schlickeiser & Röken (2008) the optical thickness effects due to synchrotron self absorption are negligible from optical to γ-ray frequencies. As the subsequent calculations are confined to the case of optical thin synchrotron emission, the considered photon energies mostly satisfy the condition $\epsilon > E_q$. Thus, the relativistic electron distribution according to Eq. (3.56) can be used and the spontaneous synchrotron emission coefficient yields

$$\begin{aligned} \tilde{j}_s(r,t,\epsilon) = \frac{P_0}{4\pi\,h}\left(\frac{\epsilon}{\epsilon_s}\right)^{\frac{1}{3}} \int_1^\infty \mathrm{d}\gamma\;\gamma^{-\frac{2}{3}}\;\exp(-\frac{\epsilon}{\epsilon_s\gamma^2})\;\sum_{k=1}^{\infty} b_k\,\frac{\sin(\lambda_k\,r)}{r} \\ \times \int_{-\infty}^{t} \mathrm{d}t'\,\frac{\exp(-\lambda_k^2\,c\,l_e(t-t')/3)}{(1-D_s\gamma(t-t'))^2}\,q_1(\tilde{\gamma}_t,t')\,. \end{aligned} \tag{4.4}$$

The relativistic electrons emit most of their energy at $\epsilon = \epsilon_s\gamma^2$. Hence, a first crude estimation of the emergent synchrotron intensity is given by taking the monochromatic approximation (Felten & Morrison, 1966) of the synchrotron spectral power in vacuum

$$P_s^0 = \frac{c\sigma_T B^2\gamma^2 h}{6\pi}\,\delta(\epsilon-\epsilon_s\gamma^2)\,, \tag{4.5}$$

so that the spontaneous synchrotron emission coefficient becomes

$$\begin{aligned} \tilde{j}_s^0(r,t,\epsilon) &= \frac{c\sigma_T B^2}{48\pi^2\,\epsilon_s}\sqrt{\frac{\epsilon}{\epsilon_s}}\;\tilde{n}_e(r,\,\gamma=\sqrt{\epsilon/\epsilon_s},\,t) \\ &= \frac{c\sigma_T B^2}{48\pi^2\,\epsilon_s}\sqrt{\frac{\epsilon}{\epsilon_s}}\;\sum_{k=1}^{\infty} b_k\,\frac{\sin(\lambda_k\,r)}{r}\int_{-\infty}^{t}\mathrm{d}t'\,\frac{\exp(-\lambda_k^2\,c\,l_e(t-t')/3)}{\left(1-D_s\sqrt{\frac{\epsilon}{\epsilon_s}}(t-t')\right)^2}\,q_1(\tilde{\gamma}_t^0,t')\,, \end{aligned} \tag{4.6}$$

where $\tilde{\gamma}_t^0 = \tilde{\gamma}_t(\gamma=\sqrt{\epsilon/\epsilon_s},\,t,\,t')$.
The spontaneous synchrotron emission coefficient is the key parameter to determine the optical thin synchrotron emission, however, the finite volume of the emission knot accounts for effects due to causality and retardation relating to the generated photon number density inside the emission volume.

4.2 Photon propagation and retardation

The relativistic electrons emit photons according to Eq. (4.3), (4.4) and (4.6), respectively, at every point $\boldsymbol{r} = r(\sqrt{1-\mu^2}\cos\phi, \sqrt{1-\mu^2}\sin\phi, \mu)$ within the spherically-symmetric

source where r, ϕ and $\mu = \cos\theta$ denote the photon's spherical coordinates. Let $\rho(r', \epsilon, t')$ denote the omnidirectional photon production rate per unit volume at a time t' and a distance r' from the center of the source. If the source is optically thin, then the photon density at a time t, a radius r and an energy ϵ is given by integrating over all emission points inside the source, generalizing Gould's (1979) formula for non-stationary sources:

$$M(r, \epsilon, t) = \frac{1}{c} \int_{-\infty}^{\infty} \mathrm{d}t' \int d^3r' \frac{\rho(r', \epsilon, t')}{4\pi s^2} \delta(t - t' - \frac{s}{c}) \,, \tag{4.7}$$

with the distance

$$s = |\boldsymbol{r} - \boldsymbol{r'}| = \left(r^2 + r'^2 - 2rr'[\mu\mu' + \sqrt{1-\mu^2}\sqrt{1-\mu'^2}\cos(\phi - \phi')]\right)^{1/2}. \tag{4.8}$$

Because of the assumed spherically-symmetric emission the spherical coordinates can be chosen in a way that $\mu = 1$, which leaves

$$s = \sqrt{r^2 + r'^2 - 2rr'\mu'} \,, \tag{4.9}$$

so that Eq. (4.7) becomes

$$M(r, \epsilon, t) = \frac{1}{2c} \int_0^R \mathrm{d}r'\, r'^2 \int_{-1}^{1} \mathrm{d}\mu' \frac{\rho(r', \epsilon, t - \frac{s}{c})}{s^2} = \frac{1}{2cr} \int_0^R \mathrm{d}r'\, r' \int_{|r-r'|}^{r+r'} \frac{\mathrm{d}s}{s} \rho\left(r', \epsilon, t - \frac{s}{c}\right) \,, \tag{4.10}$$

where s is substituted from Eq. (4.9) for the variable μ'.
In addition, the Eq. (4.10) has to take into account the loss of photons according to their escape from the emission volume. But instead of a full diffusive description of the synchrotron photon propagation, the much simpler escape probability concept of Lightman & Zdziarski (1987), as well as Coppi (1992) is employed. Here the photons are impeded from escaping in a time $\sim R/c$ by scattering off the thermal background electrons, so that

$$\dot{M}_{esc} = -\frac{\partial M}{\partial t} = \frac{c\, g(x)}{R} M(r, \epsilon, t) \tag{4.11}$$

where $x = \epsilon/(m_e c^2)$ denotes the dimensionless photon energy and the function

$$g(x) = \begin{cases} [1 + \tau_{KN}(x)]^{-1} & \text{for} \quad x \leq 0.1 \\ [1 + \tau_{KN}(x)(1-x)/0.9]^{-1} & \text{for} \quad 0.1 < x < 1 \\ 1 & \text{for} \quad x \geq 1 \end{cases} , \tag{4.12}$$

results from detailed Monte Carlo calculations of photon transport (Lightman & Zdziarski, 1987). In doing so, the Klein-Nishina scattering depth is defined by

$$\tau_{KN}(x) = (\sigma_T R N_b) \frac{\sigma_{KN}(x)}{3\sigma_T}, \tag{4.13}$$

with the Klein-Nishina cross-section

$$\begin{aligned}\sigma_{KN}(x) &= \frac{3\sigma_T}{8x}\left[\frac{4}{x}+\frac{2x(1+x)}{(1+2x)^2}-\frac{2+2x-x^2}{x^2}\ln(1+2x)\right] \\ &\simeq \begin{cases}\sigma_T & \text{for} \quad x \ll 1 \\ \frac{3\sigma_T}{16x}[1+2\ln(2x)] & \text{for} \quad x \gg 1\end{cases},\end{aligned} \tag{4.14}$$

which can be accurately approximated by the Thomson cross-section σ_T at small photon energies.
Using the light travel time $t = s/c$, the differential Eq. (4.11) yields

$$M(r,\epsilon,s) \propto \exp\left(-\frac{g(x)}{R}\,s\right) \tag{4.15}$$

and thus, the escape probability concept represents the fact that, while traversing the distance s, a photon has the survival probability $\exp(-gs/R)$. In the non-relativistic photon energy regime $\epsilon < m_e c^2$ this expression includes the effects of multiple Compton scattering and gives an accurate approximation of the probability of photon escape according to Sunyaev & Titarchuk (1980). In the relativistic photon energy regime $\epsilon \geq m_e c^2$ the large energy shift in a single Compton scattering removes a photon of an energy ϵ upon scattering. At these photon energies an energy diffusion by Comptonization in the source interior no longer occurs (Fabian et al., 1986; Lightman & Zdziarski, 1987). A photon either scatters and appears at a much lower ϵ, or it escapes in a time R/c from the source. Because there are relatively few photons in this relativistic energy region, it is a good approximation to remove these photons in proportion to their probability for scattering and to neglect their reappearance at low energies.
In consideration of poton escape, the photon intensity at the source surface $r = R$ is finally given by

$$I(R,\epsilon,t) = cM(R,\epsilon,t) = \frac{1}{2R}\int_0^R \mathrm{d}r'\,r' \int_{R-r'}^{R+r'} \frac{\mathrm{d}s}{s}\,\rho\left(r',\epsilon,t-\frac{s}{c}\right)\exp\left(-\frac{g(x)}{R}\,s\right), \tag{4.16}$$

where the omnidirectional photon production rate is related to the spontaneous photon emission coefficient by

$$\rho\left(r,\epsilon,t-\frac{s}{c}\right) = 4\pi j_s\left(r,t-\frac{s}{c},\epsilon\right). \tag{4.17}$$

As noted before, the near isotropy of the synchrotron photon intensity at the edge of the emission knot results from the chaotic magnetic field in the emission knot and multiple Compton scatterings of the generated synchrotron photons of the thermal electrons, which allows to use the diffusion approximation for the spatial transport of synchrotron photons (Sunyaev & Titarchuk, 1980).
When the surface of the emission volume is reached, the photons can propagate freely to the observer. The emergent photon intensity therefore equals the surface intensity $I(R,\epsilon,t)$.

4.3 Synchrotron radiation in a first crude approach

Since the emergent synchrotron intensity, that results from the monochromatic approximation of the synchrotron power spectrum has already been discussed in great detail in the diploma thesis (Eichmann, 2009), this section resumes only the basic results, that will be used in the following sections.
Here, the mathematical convenient case of an instantaneous injection of monoenergetic ultra-relativistic electrons (3.29) is considered, so that the spontaneous synchrotron emission coefficient (4.6) yields after some simple transformations in the argument of the delta function

$$\begin{aligned}\tilde{j}_s^0(r,\epsilon,t) =& \frac{c\sigma_T q_0 B^2}{24\pi^2} H[t-t_0]\delta\left(\epsilon - \frac{E_0}{[1+D_s\gamma_0(t-t_0)]^2}\right)\frac{\epsilon}{\epsilon_s} \\ &\times \sum_{k=1}^{\infty} b_k \frac{\sin(\lambda_k r)}{r}\exp\left(-cl_e\lambda_k^2(t-t_0)/3\right),\end{aligned} \tag{4.18}$$

where the initial synchrotron photon energy

$$E_0 = \epsilon_s\gamma_0^2 = 17.4b\gamma_6^2 \text{ keV} \tag{4.19}$$

is introduced. Using the Eq. (4.17) and (4.16), as well as multiple transformations and the definition of an energy dependent time scale

$$t_s \equiv t_0 + \frac{1}{D_s\gamma_0}\left(\sqrt{\frac{E_0}{\epsilon}} - 1\right), \tag{4.20}$$

the subsequent expression can be integrated analytically. Thus, the emergent synchrotron intensity becomes

$$\begin{aligned}I(R,\epsilon,t) =& \frac{c\sigma_T q_0 B^2\gamma_0}{24\pi D_s R}\frac{H[E_0-\epsilon]}{(\epsilon E_0)^{1/2}} H[t-t_s]H\left[\frac{2R}{c}+t_s-t\right]\frac{\exp\left(-\frac{g(x)c(t-t_s)}{R}\right)}{t-t_s} \\ &\times \sum_{k=1}^{\infty}\frac{b_k}{\lambda_k}\exp\left(-\frac{cl_e\lambda_k^2}{3D_s\gamma_0}(\sqrt{\frac{E_0}{\epsilon}}-1)\right)\left[\cos\left(\lambda_k\left(R-c(t-t_s)\right)\right)-\cos\left(\lambda_k R\right)\right],\end{aligned} \tag{4.21}$$

which gives the following immediate conclusion of the synchrotron flare duration and flare onset time in the comoving frame of reference:
(1) The total duration of the synchrotron flare at all photon energies ϵ is $2R/c$, but it has to be noted that the resulting sharp cut-offs are a consequence of the adopted monochromatic approximation (4.5) of the synchrotron power.
(2) During this energy independent total duration, shorter synchrotron photon energy-dependent time variations are in principle possible. Therefore, the initial spatial distribution of the relativistic electrons according to b_k has to emerge the influence of single eigenvalues with $k > 1$ on the emergent synchrotron intensity, which requires quite special locations of the relativistic particle accelerators.

(3) The starting time of the synchrotron flare at photon energy ϵ is delayed with respect to the injection time of electrons t_0 by the photon energy dependent time scale t_s as defined in Eq. (4.20). This delay reflects the necessary cooling time which relativistic electrons need to radiate at photon energies below $E_0 \propto B\gamma_0^2$, but its discrete value is also a consequence of using the monochromatic approximation for the synchrotron power.
The temporal development of the emergent synchrotron intensity (4.21) is illustrated in Fig. (4.2) and (4.4) for the initial particle distribution due to Eq. (3.32) and (3.33), respectively.

4.4 Synchrotron radiation with respect to the broadband synchrotron power spectrum

The previous examinations have already given some characteristics of the temporal development of synchrotron flares, but a significant influence of the used monochromatic approximation of the synchrotron power spectrum could not be excluded. Furthermore, the established constant synchrotron flare total duration time is in conflict with recent observations of optical and X-ray synchrotron emission from flaring blazars. Simultaneous observations of the blazar PKS 2155-304 in the optical and X-ray regime have shown, that the optical emission starts at the same time as the X-ray flare, but reaches its maximal value about some hours later and lasts a significant longer timescale (Fig. 4.11). In order to remedy this conflicting theoretical result the monochromatic approximation of the synchrotron spectral power is discarded and an improved representation of the synchrotron power that accounts for the broadband nature of the synchrotron emission of a single electron is used instead.

4.4.1 Emergent synchrotron intensity by a monoenergetic, instantaneous electron injection

First, a monoenergetic, instantaneous electron injection $q_1(\gamma, t) = q_0\,\delta(\gamma - \gamma_0)\,\delta(t - t_0)$ is assumed, so that the spontaneous synchrotron emission coefficient (4.4) yields

$$\begin{aligned}\tilde{j}_s(r,\epsilon,t) =& \frac{P_0 q_0}{4\pi\, h} H[t-t_0] \left(\frac{\epsilon}{\epsilon_s}\right)^{\frac{1}{3}} \left(\frac{\gamma_0}{1+D_s\gamma_0(t-t_0)}\right)^{-\frac{2}{3}} \exp\left(-\frac{\epsilon(1+D_s\gamma_0(t-t_0))^2}{\epsilon_s\gamma_0^2}\right) \\ &\times \sum_{k=1}^{\infty} b_k \frac{\sin(\lambda_k r)}{r}\, e^{-\frac{cl_e\lambda_k^2}{3}(t-t_0)}\,.\end{aligned} \tag{4.22}$$

Substituting $y = s - R$ in Eq. (4.16) and inserting the production rate (4.17) by using Eq. (4.22), one obtains

$$\begin{aligned}I(R,\epsilon,\tau) =& \frac{P_0 q_0}{2hR} \left(\frac{\epsilon}{E_0}\right)^{\frac{1}{3}} \sum_{k=1}^{\infty} b_k \exp\left(-g(x) - \frac{\epsilon}{E_0}(1+D_s\gamma_0\tau)^2 - \frac{cl_e\lambda_k^2}{3}\tau\right) \\ &\times \int_0^R dr'\, \sin(\lambda_k r')\, J(\epsilon,\tau)\,,\end{aligned} \tag{4.23}$$

with the inner integral

$$J(\epsilon,\tau) = \int_{-r'}^{r'} dy\, H[\tau - y/c]\, \frac{(1 + D_s\gamma_0(\tau - y/c))^{\frac{2}{3}}}{R+y}\, \exp\left(-A\, y^2 + B_k(\tau)\, y\right), \quad (4.24)$$

where

$$\tau = t - t_0 - R/c, \quad (4.25)$$

$$A = \frac{\epsilon D_s^2 \gamma_0^2}{E_0 c^2}, \quad (4.26)$$

$$B_k(\tau) = \frac{2\epsilon}{cE_0}(D_s\gamma_0 + D_s^2\gamma_0^2\tau) + \frac{l_e\lambda_k^2}{3} - \frac{g(x)}{R} \quad (4.27)$$

and E_0 denotes the initial synchrotron photon energy according to Eq. (4.19). Integrating the Eq. (4.23) by parts (Appendix C.1) results in

$$I(R,\epsilon,\tau) = \frac{P_0\, q_0}{2\, h\, R}\left(\frac{\epsilon}{E_0}\right)^{\frac{1}{3}} e^{-g(x) - \frac{\epsilon}{E_0}(1+D_s\gamma_0\tau)^2}\, H[\tau + R/c] \sum_{k=1}^{\infty} \frac{b_k}{\lambda_k}\, \exp\left(-\frac{c l_e \lambda_k^2 \tau}{3}\right)$$
$$\times \int_{-R}^{U} dr'\, (\cos(\lambda_k r') - \cos(\lambda_k R)) \frac{(1 + D_s\gamma_0(\tau - r'/c))^{\frac{2}{3}}}{R + r'} \exp\left(-A\, r'^2 + B_k(\tau) r'\right), \quad (4.28)$$

where

$$U = \begin{cases} c\tau & \text{for} \quad \tau < R/c \\ R & \text{for} \quad \tau \geq R/c\,. \end{cases}$$

Analytical approximation

At $\tau \geq R/c$ the upper limit of the integral in Eq. (4.28) becomes independent of the time and the expression to the power of 2/3 is dominated by the time τ. In the full diffusion limit ($l_e \ll R$) the mean scattering length l_e has a minor influence on the emergent synchrotron intensity and $|B_k(\tau)| \ll 1/r'$ when

$$\left(5.0 \cdot 10^{-18}\, \gamma_6^{-1}(b + b^{-1} l_{EC}) + 1.9 \cdot 10^{-8}\right)\, (\epsilon/\mathrm{eV})\, \mathrm{cm}^{-1} \ll 1/r'\,,$$

as well as

$$\left(6.5 \cdot 10^{-21}\, (b^{3/2} + b^{-1/2}\, l_{EC})^2\right)\, (\epsilon/\mathrm{eV})\, (\tau/\mathrm{s})\, \mathrm{cm}^{-1} \ll 1/r'\,,$$

so that the last exponential term in Eq. (4.28) can be approximated by one. Additionally, the second exponential term is also negligible for $\tau \ll 10^{19} (l_e/\mathrm{cm})^{-1}\,\mathrm{s}$. In order to obtain an accurate approximation we choose $l_e = 10^{10}\, l_{10}\,\mathrm{cm}$. Due to the trigonometric functions and $(R + r')^{-1}$ in the integrand, the integral reaches its maximal value at $r' \ll R$. Thus,

the temporal development of the emergent synchrotron intensity can be approximated by

$$I(\epsilon, z > z_0) \simeq I_0 \left(\frac{\epsilon}{E_0}\right)^{\frac{1}{3}} z^{\frac{2}{3}} \exp\left(-\frac{\epsilon}{E_0} z^2\right), \tag{4.29}$$

with the dimensionless time scale $z = 1 + D_s \gamma_0 \tau$ and $z_0 = 1 + D_s \gamma_0 R/c$.
The synchrotron light curves reach its maximal value at a time z_{max} when $\partial I/\partial z = 0$, which yields the time of maximal synchrotron flare emission

$$z_{max} = \sqrt{E_0/(3\epsilon)}, \tag{4.30}$$

where

$$\epsilon < \epsilon_b = 3.0\, b^{-3} R_{15}^{-2}\,\mathrm{eV}, \tag{4.31}$$

so that $z_{max} > z_0$.

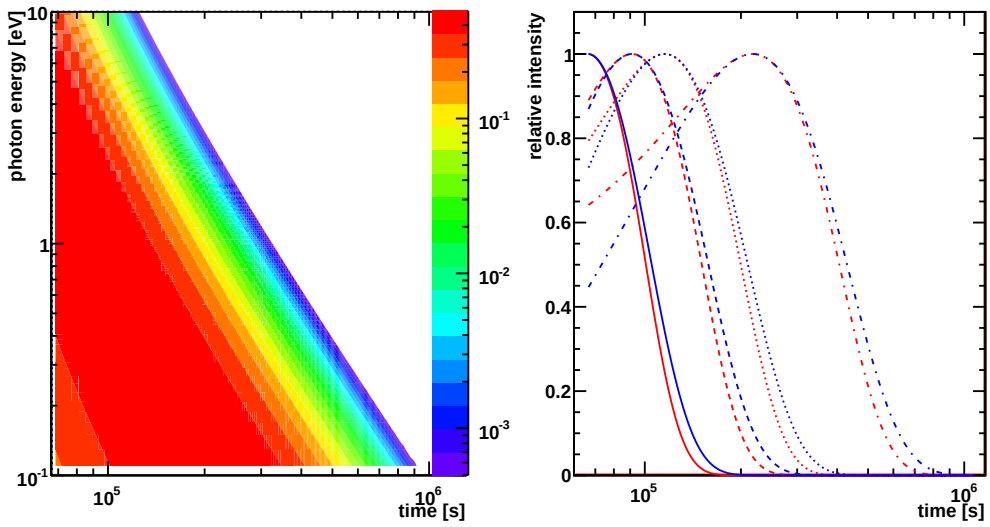

Figure 4.1: *Left panel:* The temporal and energy dependent behavior of I/I_0 according to Eq. (4.29).
Right panel: Approximation of the temporal synchrotron flare development $I/\bar{I}_0$ (blue line) and $\bar{I}/\bar{I}_0$ (red line), respectively, at $t \geq 2R/c + t_0$. Four different photon energies (3 eV (solid line), 1 eV (dashed line), 0.5 eV (dotted line), 0.1 eV (dash dotted line)) are used, as well as the default parameters.

Fig. 4.1 shows, that $I(\epsilon, z > z_0)$ decreases with increasing time or energy, so that it confines the flare duration of optical synchrotron photons. Using the method of the steepest descent the half-life and the half width of the synchrotron flare can be evaluated analytically. Therefore, the emergent intensity (4.29) is developed at $z = z_{max}$ in the argument of the exponential function (Appendix C.2), which results in

$$\bar{I}(\epsilon, z > z_0) \simeq \bar{I}_0 \exp\left(-\frac{2\epsilon}{E_0}\left(z - \sqrt{\frac{E_0}{3\epsilon}}\right)^2\right), \tag{4.32}$$

with

$$\bar{I}_0 = I_0/(3e)^{\frac{1}{3}} \,. \tag{4.33}$$

So the optical synchrotron light curves with $\epsilon < \epsilon_b$ have a Gaussian time distribution at $z > z_0$.
The equation $\bar{I}(\epsilon, z_{1/2})/\bar{I}(\epsilon, z_{max}) = 1/2$ yields the half-life

$$z_{1/2} = \sqrt{\frac{E_0}{3\epsilon}} \left(1 \pm \sqrt{\frac{3\ln 2}{2}}\right) \,, \tag{4.34}$$

and the half width

$$\Delta z_{1/2} = \sqrt{2\ln 2}\sqrt{\frac{E_0}{\epsilon}} \,. \tag{4.35}$$

Fig. 4.1 (right panel) illustrates the temporal development of Eq. (4.29) and its approximation (4.32) at different photon energies. With decreasing photon energy the delay of the time of maximal synchrotron emission increases, as well as the half-life and the half width of the light curves. In addition, it shows that Eq. (4.32) is an accurate approximation of Eq. (4.29), but $\bar{I}$ has a steeper slope at $z \ll z_{max}$ and a steeper descent at $z \gg z_{max}$.
In the following, the analytical approximated temporal behavior (4.32) of the optical flare will be compared with the results of a numerical evaluation of Eq. (4.28).

Numerical calculations

The temporal synchrotron flare development at $t < 2R/c + t_0$ and photon energies $\epsilon > \epsilon_b$, respectively, has to be calculated numerically. In order to derive the exact emergent synchrotron intensity, it is necessary to specify the spatial expansion coefficients b_k by Eq. (3.32) or (3.33). Finally, the Eq. (4.28) is evaluated by Romberg integration with an extended midpoint rule algorithm (see Appendix E.1 for more details).
Fig. (4.2) shows the temporal behavior of the emergent synchrotron intensity for two different photon energies that results from taking the spatial injection coefficient (3.32). Additionally, the emergent synchrotron intensity of the previous section is displayed (dotted lines), where a monochromatic synchrotron power spectrum is used. In consideration of the broadband nature of the synchrotron power spectrum according to Eq. (2.14) the light curves increase strictly right after the instantaneous electron injection at $t = t_0$ (independent of ϵ) till its maximal value is reached and decrease exponentially after the peak. Obviously, the X-ray flare (red solid line) is much better approximated by the Eq. (4.21) than the optical flare (blue solid line), which develops on much longer time scales because of the temporal behavior of the first exponential expression in Eq. (4.28). Thus, the X-ray light curve (red solid line) reaches the maximal intensity close to t_s at

$$t_{max}(\epsilon > \epsilon_b) \simeq t_0 + \frac{c_l(\epsilon)}{D_s\,\gamma_0}\left(\sqrt{\frac{E_0}{\epsilon}} - 1\right) \,, \tag{4.36}$$

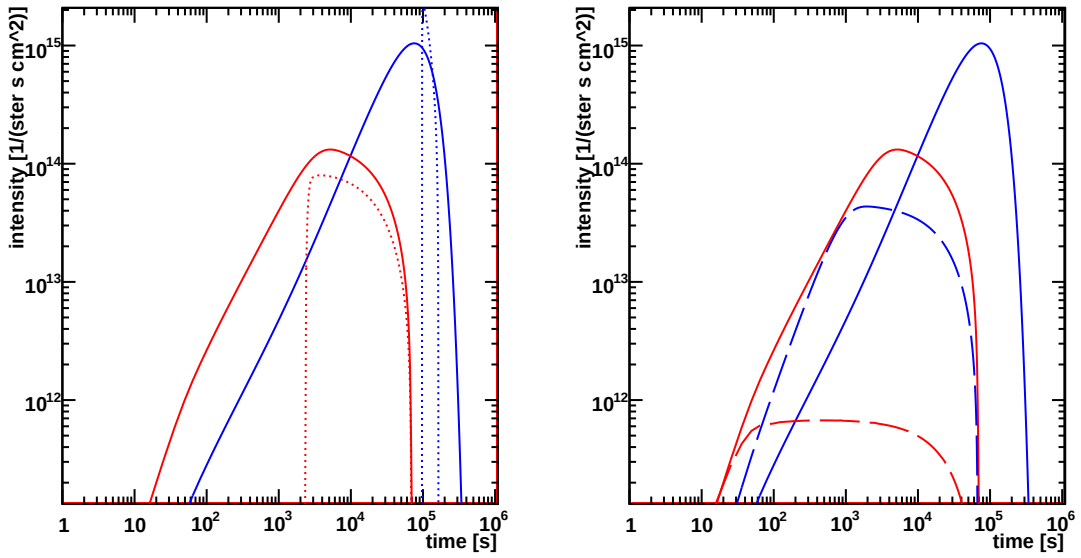

Figure 4.2: Temporal flare behavior of optical synchrotron photons at $\epsilon = 1\,\mathrm{eV}$ (blue lines) and soft X-rays at $\epsilon = 1\,\mathrm{keV}$ (red lines) after a homogeneous electron injection into the whole plasmoid volume with the default parameters in the full diffusion limit. Using a synchrotron dominated cooling rate with $b = 1$ and $l_{EC} \ll 1$, the left panel illustrates the light-curves according to Eq. (4.21) of the previous section (dotted line) and the new results (solid line), that account for the broadband nature of the synchrotron power spectrum. In addition to the light-curves dominated by synchrotron cooling (solid line) the right panel shows the light curves resulting from dominant EC cooling (dashed line) with $l_{EC} = 38$ and $b \ll 1$.

with the linear function $c_l(\epsilon) = 0.5\,(\epsilon/1\,\mathrm{keV}) + 1.8$, that yields a heuristic correction value of the time of maximal X-ray emission in relation to Eq. (4.20). Furthermore, the X-ray light curve decreases comparably to the light curve that are calculated with the monochromatic synchrotron power spectrum and the Eq. (4.21) is an accurate approximation for the X-ray synchrotron photon emission at $t_s < t < t_s + 2R/c$. Consequently, the total duration of the X-ray synchrotron flare is determined by

$$t_d(\epsilon > \epsilon_b) \simeq \frac{2R}{c} + t_s - t_0 = \frac{2R}{c} + \frac{1}{D_s \gamma_0}\left(\sqrt{\frac{E_0}{\epsilon}} - 1\right) . \tag{4.37}$$

The optical synchrotron flare is not accurately described by the results of Sect. 4.3, but the previously derived, analytical terms can be adopted. So Fig. (4.3) illustrates normalized light curves at near infrared to ultraviolet photon energies resulting from a numerical calculation (blue line) and an analytical approximation by Eq. (4.32) (red line). Apparently, the Eq. (4.32) is a suitable approximation of the temporal development of the emergent synchrotron intensity at $\epsilon < \epsilon_b$ and hence, Eq. (4.30) accurately determine that

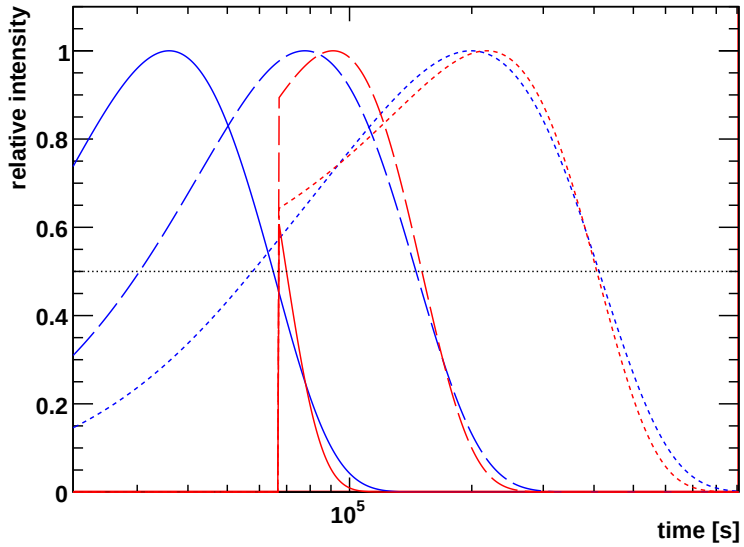

Figure 4.3: Normalized temporal development of the emergent synchrotron intensity at three different photon energies (10 eV (solid line), 1 eV (long dashed line), 0.1 eV (short dashed line)), calculated by the analytical approximation (4.32) (red lines) and the numerical integration of Eq. (4.28) (blue lines). The intersection with the black dotted line yields the half-life of the light curve, when the light curve has a maximal value of 1.

the optical light curve reaches its maximal intensity at

$$t_{max}(\epsilon < \epsilon_b) \simeq t_0 + \frac{R}{c} + \frac{1}{D_s \gamma_0} \left(\sqrt{\frac{E_0}{3\epsilon}} - 1 \right) . \tag{4.38}$$

With Eq. (4.34) the half-life of a synchrotron flare at photon energies $\epsilon < \epsilon_b$ yields

$$t_{1/2}(\epsilon < \epsilon_b) = t_0 + \frac{R}{c} + \frac{1}{D_s \gamma_0} \left(\sqrt{\frac{E_0}{3\epsilon}} \left(1 + \sqrt{\frac{3 \ln 2}{2}} \right) - 1 \right) . \tag{4.39}$$

At $\epsilon > \epsilon_b$ the half-life still decreases with increasing photon energy, but the integral in Eq. (4.28) admits no further analytical conclusions. However, as stated above the total synchrotron flare duration at $\epsilon \gg \epsilon_b$ converges to the light travel time $2R/c$.
Fig. (4.4) shows light-curves at $\epsilon = 1\,\text{eV}$ (left graphic) and $\epsilon = 1\,\text{keV}$ (right graphic), respectively, resulting from Eq. (4.28) with the spatial injection coefficient (3.33) for different electron injection shells with an inner radius r_1, as well as the corresponding light curves of Sect. 4.3 where a monochromatic approximation of the synchrotron spectrum is used. The features are similar to the case of an homogenous injection into the whole knot (black line), but the amplitudes of the light-curves are lower. However, the amplitude increases with decreasing r_1, as the total number of injected electrons increases. In case of X-ray photons the synchrotron light curves have a steeper descent after reaching its maximum,

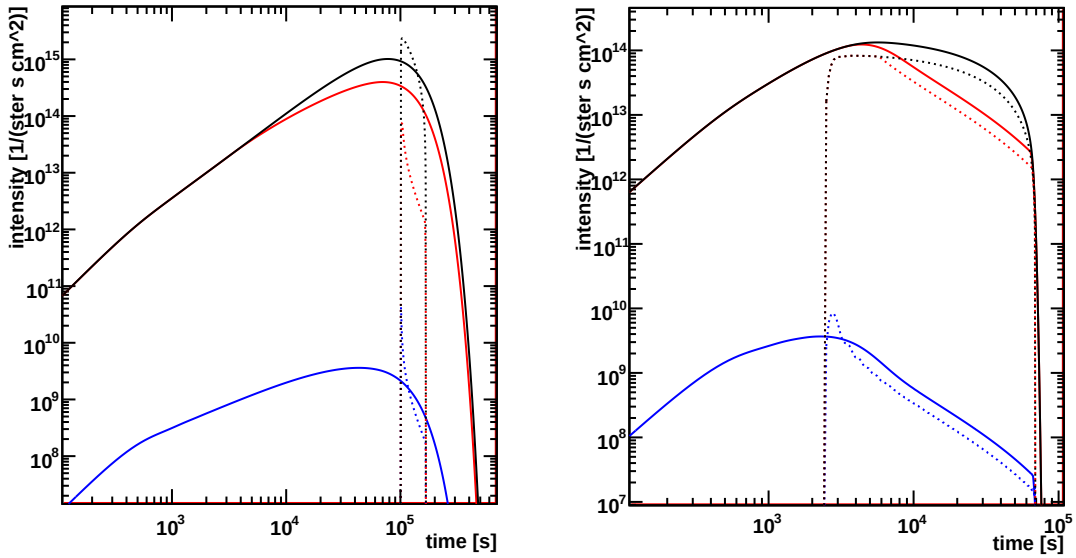

Figure 4.4: Synchrotron light-curves of photons with $\epsilon = 1\,\mathrm{eV}$ (left panel) and $\epsilon = 1\,\mathrm{keV}$ (right panel), respectively, resulting from a homogeneous electron injection over the outer shell of the plasmoid ($r_1 \leq r \leq R$). The solid lines are the result of the numerical integration of Eq. (4.28), whereas the dotted lines are calculated according to Eq. (4.21). It is illustrated for $r_1 = 0.9999\,R$ (blue line), $r_1 = 0.9\,R$ (red line) and $r_1 = 0$ (black line) with the default parameters in the full diffusion limit.

but the total flare duration stays the same. Consequently, the spatial distribution of an isotropic source has no influence on the duration of a synchrotron flare, but it sets the amplitude of the light curves.

4.4.2 Emergent synchrotron intensity by an instantaneous injection of electrons with power-law distributed energy

As next illustrative example, the case of an instantaneous injection of electrons with power-law distributed energy is considered, so that with Eq. (3.30) the spontaneous synchrotron emission coefficient (4.4) yields

$$\begin{aligned}\tilde{j}_s(r,\epsilon,t) =& \frac{P_0 q_0}{4\pi\, h}\left(\frac{\epsilon}{\epsilon_s}\right)^{\frac{1}{3}} \sum_{k=1}^{\infty} b_k \frac{\sin(\lambda_k r)}{r}\, H[t-t_0]\, H[(D_s(t-t_0))^{-1}-1]\, e^{-cl_e\lambda_k^2(t-t_0)/3} \\ &\times \int_1^{(D_s(t-t_0))^{-1}} d\gamma\; \gamma^{-\frac{2}{3}+\alpha} \exp\left(-\frac{\epsilon}{\epsilon_s\gamma^2}\right) (1-D_s\gamma(t-t_0))^{-\alpha-2}\,.\end{aligned} \tag{4.40}$$

Here the relativistic electrons emit no further synchrotron photons at $t > D_s^{-1} + t_0$, since also the most energetic electrons are cooled down to $\gamma = 1$. But according to Eq. (3.53)

the synchrotron emission already cuts off much earlier due to the effect of excitation losses. Using Eq. (4.40), (4.17) and (4.16) the emergent synchrotron intensity is given by

$$\begin{aligned} I(R,\epsilon,t) =& \frac{P_0 q_0}{2Rh}\left(\frac{\epsilon}{\epsilon_s}\right)^{\frac{1}{3}} \sum_{k=1}^{\infty} b_k \int_0^R dr' \, \sin(\lambda_k r') \\ & \times \int_{R-r'}^{R+r'} \frac{ds}{s} \, H\left[s - c(t-t_0-1/D_s)\right] H\left[c(t-t_0)-s\right] e^{-g(x)\frac{s}{R}} \, e^{-cl_e\lambda_k^2(t-\frac{s}{c}-t_0)/3} \\ & \times \int_1^{(D_s(t-t_0))^{-1}} d\gamma \; \gamma^{-\frac{2}{3}+\alpha} \exp\left(-\frac{\epsilon}{\epsilon_s\gamma^2}\right) (1 - D_s\gamma(t-\frac{s}{c}-t_0))^{-\alpha-2} \, . \end{aligned} \tag{4.41}$$

The Heaviside functions split the Eq. (4.41) in several integrals, as shown in the Appendix D, however, at $t < c/D_s + t_0$ the emergent synchrotron intensity is simplified to

$$\begin{aligned} I(R,\epsilon,t<c/D_s+t_0) = & \frac{P_0 q_0}{2Rh}\left(\frac{\epsilon}{\epsilon_s}\right)^{\frac{1}{3}} \sum_{k=1}^{\infty} b_k \\ & \times \Bigg(H[ct-R] \int_0^U dr' \, \sin(\lambda_k r') \int_{R-r'}^{R+r'} \frac{ds}{s} e^{-g(x)\frac{s}{R}} \, e^{-cl_e\lambda_k^2(t-\frac{s}{c}-t_0)/3} \\ & \times \int_1^{(D_s(t-t_0))^{-1}} d\gamma \; \gamma^{-\frac{2}{3}+\alpha} \exp\left(-\frac{\epsilon}{\epsilon_s\gamma^2}\right) (1 - D_s\gamma(t-\frac{s}{c}-t_0))^{-\alpha-2} \\ & + H[R-|R-ct|] \int_{|R-ct|}^{R} dr' \, \sin(\lambda_k r') \int_{R-r'}^{ct} \frac{ds}{s} e^{-g(x)\frac{s}{R}} \, e^{-cl_e\lambda_k^2(t-\frac{s}{c}-t_0)/3} \\ & \times \int_1^{(D_s(t-t_0))^{-1}} d\gamma \; \gamma^{-\frac{2}{3}+\alpha} \exp\left(-\frac{\epsilon}{\epsilon_s\gamma^2}\right) (1 - D_s\gamma(t-\frac{s}{c}-t_0))^{-\alpha-2} \Bigg) \end{aligned} \tag{4.42}$$

with

$$U = \begin{cases} c\,(t-t_0) - R & \text{for} \quad t < 2R/c + t_0 \\ R & \text{for} \quad t \geq 2R/c + t_0 \, . \end{cases}$$

The injection of power-law distributed electrons results in a more extensive expression than in the previous case of an instantaneous, monoenergetic electron injection and no analytical conclusion can be drawn about the temporal development of the synchrotron flare. After specifying the spatial injection coefficient b_k by Eq. (3.32) and (3.33), respectively, the three dimensional integral expression in Eq. (4.42) has to be solved by a numerical algorithm of integration. Assuming that most of the sinus and exponential functions in Eq. (4.42) have rather small arguments, the integrand can be well-approximated by a polynomial and the N-point Gaussian quadrature rule appears suitable (details of the concept of Gaussian quadrature is given in the Appendix E.2). The complexity of the three dimensional integral expression makes it hard to verify which degree of the polynomial gives an accurate approximation of the integrand, so that a trial-and-error method is used to determine a capable N. According to Fig. (4.5) a small N leads to distinct inaccuracies at the beginning of the flare, as well as unphysical fluctuations even at later times. These N

dependent differences in the light curves vanish for a Gaussian quadrature with $N \geq 40$ and in order to minimize the computation time $N = 40$ is used in the following.

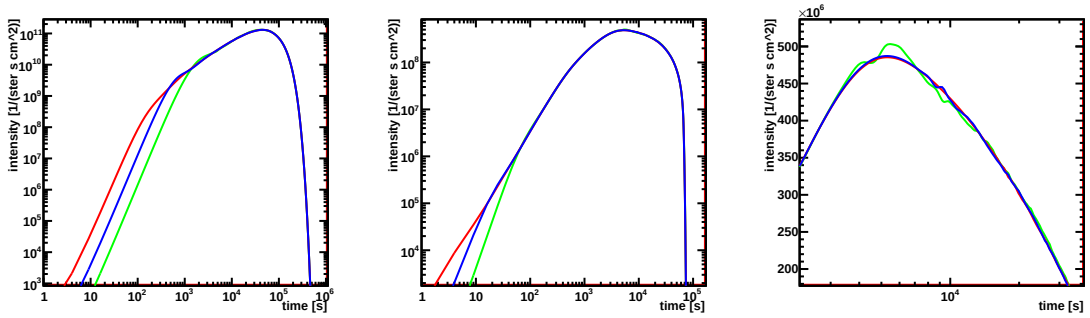

Figure 4.5: The emergent synchrotron intensity of optical photons at $\epsilon = 1\,\mathrm{eV}$ (left panel), as well as soft X-rays at $\epsilon = 1\,\mathrm{keV}$ (middle and right panel), that results from a N-point Gaussian quadrature, where $N = 10$ (green line), $N = 20$ (blue line) and $N = 40$ (red line). A homogenous electron injection into the whole plasmoid volume with a spectral index $\alpha = -2$, as well as the default parameters in the full diffusion limit are used.

First, the case of a homogeneous electron injection into the whole plasmoid volume is examined. Fig. (4.6) shows the resulting temporal development of the emergent synchrotron intensity by assuming a spectral index of $\alpha = -3$ (solid lines) and $\alpha = -2$ (long dashed lines), respectively. In addition, the light curves resulting from the previous injection assumption, i. e. a monoenergetic and instantaneous injection (short dashed lines), are illustrated. Due to the power-law distribution of the relativistic electrons the amplitude of the light curves increases with increasing α, but stays below the (dotted) light curves, which result from a monoenergetic electron injection. The general temporal development of the synchrotron flare is roughly independent of the spectral index. However, at low synchrotron photon energies the light curves differ from the previous results which refer to Eq. (4.28). The temporal flare behavior slightly shortens with decreasing photon energy and spectral index α, since the power-law distribution of the initial electrons provides an increasing number of relativistic electrons with decreasing Lorentz factor when $\alpha < 0$. Consequently, the time at which most of the relativistic electrons generate synchrotron photons with low energies becomes shorter due to less cooling time and this effect logically increases with decreasing α. But still the Eq. (4.39) and (4.38) give at least an upper limit of the flare duration and the time of maximal flare emission, respectively.
The second approach uses a homogeneous electron injection till different radii r_1 according to the expansion coefficient (3.33). Fig. (4.7) shows, that the amplitude of the new light curves increase with increasing source area, but the general temporal development is not effected by the spatial injection assumption, so that the temporal development stays the same.
To sum up, an initial particle distribution with a power-law distributed energy yields, compared with a monoenergetic injection, no significant difference in the synchrotron light curves at high energies, but at low synchrotron photon energies the temporal development is slightly shortened. This approves Zacharias & Schlickeiser (2010), who stated that an

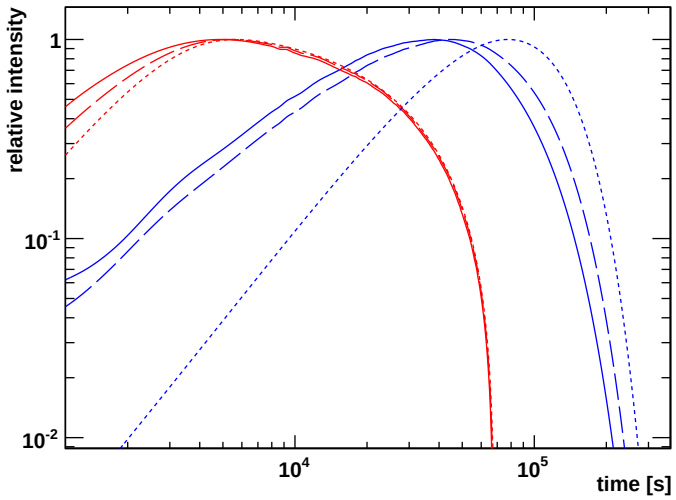

Figure 4.6: Temporal flare behavior of optical photons at $\epsilon = 1\,\mathrm{eV}$ (blue lines) and soft X-rays at $\epsilon = 1\,\mathrm{keV}$ (red lines) after a homogeneous electron injection into the whole plasmoid volume with the default parameters in the full diffusion limit. The solid and the long dashed lines are calculated by Eq. (4.42) with $\alpha = -3$, as well as $\alpha = -2$ and normalized afterwards. The short dashed lines show the normalized emergent intensity evaluated by Eq. (4.28) in the previous section. The maximal emergent intensities (in $\mathrm{ster}^{-1}\,\mathrm{s}^{-1}\,\mathrm{cm}^{-2}$) are in turn: $I_{max}(\epsilon = 1\,\mathrm{eV}, \alpha = -3) = 1.1 \cdot 10^{7}$, $I_{max}(\epsilon = 1\,\mathrm{keV}, \alpha = -3) = 1.1 \cdot 10^{3}$, $I_{max}(\epsilon = 1\,\mathrm{eV}, \alpha = -2) = 1.3 \cdot 10^{11}$, $I_{max}(\epsilon = 1\,\mathrm{keV}, \alpha = -2) = 4.9 \cdot 10^{8}$, $I_{max}(\epsilon = 1\,\mathrm{eV}, \alpha = 0\,\mathrm{s}) = 1.0 \cdot 10^{15}$ and $I_{max}(\epsilon = 1\,\mathrm{keV}, \alpha = 0\,\mathrm{s}) = 1.3 \cdot 10^{14}$.

initial power-law distribution of relativistic electrons becomes a δ-distribution when the electrons have cooled significantly.

4.4.3 Emergent synchrotron intensity by a monoenergetic electron injection of finite duration

In the following, the influence of a finite injection duration T is investigated and compared with the previous results. Therefore, the Eq. (3.31) is used, which results in power-law distributed relativistic electrons with a spectral index of -2 at the period $1/D_s(1/\gamma - 1/\gamma_0) < t < 1/D_s(1/\gamma - 1/\gamma_0) + T$ and the spontaneous synchrotron emission coefficient (4.4) yields

$$\tilde{j}_s(r,\epsilon,t) = \frac{P_0 q_0}{4\pi\, h D_s} \left(\frac{\epsilon}{\epsilon_s}\right)^{\frac{1}{3}} \sum_{k=1}^{\infty} b_k \frac{\sin(\lambda_k r)}{r} \exp\left(\frac{c l_e \lambda_k^2}{3 D_s \gamma_0}\right) \times \int_1^{\gamma_0} d\gamma\, H\left[\frac{\gamma_0}{1 + D_s\gamma_0(t-T)} - \gamma\right] \gamma^{-\frac{8}{3}} H\left[\gamma - \frac{\gamma_0}{1 + D_s\gamma_0 t}\right] \exp\left(\frac{c l_e \lambda_k^2}{3 D_s \gamma} - \frac{\epsilon}{\epsilon_s \gamma^2}\right). \tag{4.43}$$

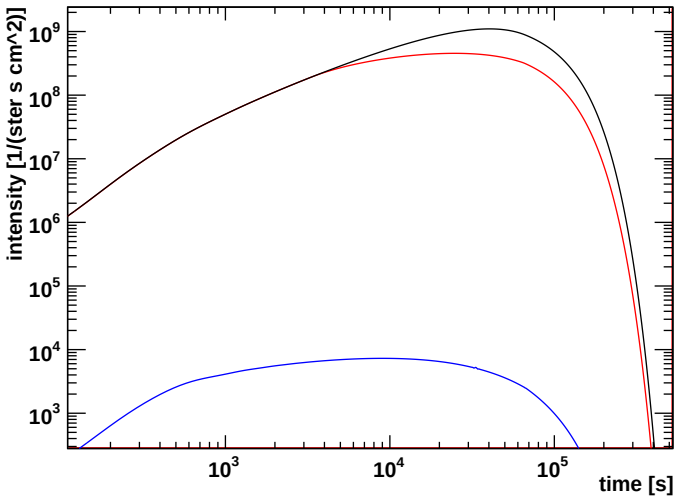

Figure 4.7: Synchrotron light-curves of optical photons ($\epsilon = 1\,\mathrm{eV}$) resulting from an instantaneous injection of power-law distributed electrons with $\alpha = -2.5$ over the outer shell of the plasmoid ($r_1 \leq r \leq R$). The light curves are shown for $r_1 = 0.9999\,R$ (blue line), $r_1 = 0.9\,R$ (red line) and $r_1 = 0$ (black line) with the default parameters in the full diffusion limit.

Inserting the emission coefficient (4.43) in the production rate (4.17), the emergent synchrotron intensity (4.16) becomes

$$\begin{aligned} I(R,\epsilon,t) =& \frac{P_0 q_0}{2RhD_s}\left(\frac{\epsilon}{\epsilon_s}\right)^{\frac{1}{3}} \sum_{k=1}^{\infty} b_k \exp\left(\frac{c l_e \lambda_k^2}{3D_s\gamma_0}\right) \int_0^R dr' \,\sin(\lambda_k r') \int_{R-r'}^{R+r'} \frac{ds}{s}\,\exp(-g(x)s/R) \\ &\times \int_1^{\gamma_0} d\gamma\, H\left[\frac{\gamma_0}{1+D_s\gamma_0(t-s/c-T)} - \gamma\right] H\left[\gamma - \frac{\gamma_0}{1+D_s\gamma_0(t-s/c)}\right] \gamma^{-\frac{8}{3}} \\ &\times \exp\left(\frac{c l_0 \lambda_k^2}{3D_s\gamma} - \frac{\epsilon}{\epsilon_s\gamma^2}\right). \end{aligned} \tag{4.44}$$

Like in the previous section, the three dimensional integral expression allows no analytical conclusion about the temporal development of the synchrotron flare and a 40-point Gaussian quadrature method is used to solve the expression. But first, the Heaviside functions have to be extricated from the three integrations, so that the limits of integration become partially time and energy dependent and the number of integrals amplifies to over one hundred (which is not shown because of the lack of space, but easy to anticipate with Appendix D). In addition, the spatial injection assumption has to be specified by taking Eq. (3.32) and Eq. (3.33), respectively.
Fig (4.8) illustrates the resulting temporal development of the emergent synchrotron intensity in two different energy regimes by assuming a homogeneous electron injection into the whole emission knot and an injection duration of $T = 10^4\,\mathrm{s}$ (solid lines) and $T = 10^5\,\mathrm{s}$ (long dashed lines), respectively. The new light curves have a temporal evolution, that is

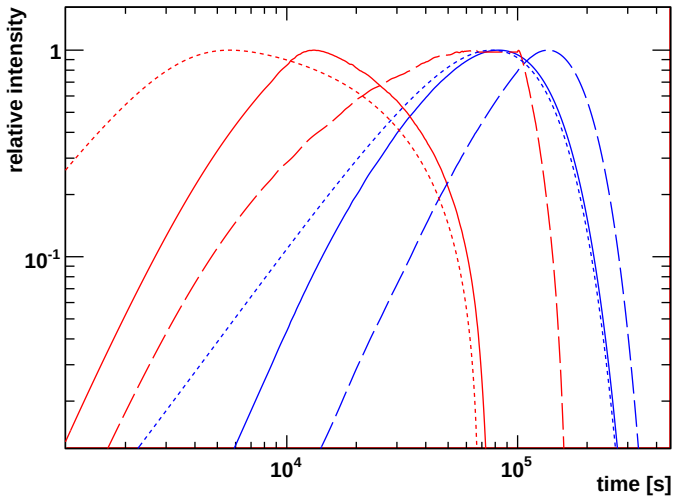

Figure 4.8: Temporal synchrotron flare behavior of optical photons at $\epsilon = 1\,\mathrm{eV}$ (blue lines) and soft X-rays at $\epsilon = 1\,\mathrm{keV}$ (red lines) after a homogenous electron injection into the whole plasmoid volume with the default parameters in the full diffusion limit. The normalized light curves are calculated by Eq. (4.44) with an injection duration of $T = 10^4\,\mathrm{s}$ (solid lines) and $T = 10^5\,\mathrm{s}$ (long dashed lines), respectively, whereas the short dashed light curves show the emergent intensity evaluated by Eq. (4.28) in the previous section. The maximal emergent intensity (in $\mathrm{ster}^{-1}\,\mathrm{s}^{-1}\,\mathrm{cm}^{-2}$) are in turn: $I_{max}(\epsilon = 1\,\mathrm{eV}, T = 10^4\,\mathrm{s}) = 1.0 \cdot 10^{19}$, $I_{max}(\epsilon = 1\,\mathrm{keV}, T = 10^4\,\mathrm{s}) = 1.2 \cdot 10^{18}$, $I_{max}(\epsilon = 1\,\mathrm{eV}, T = 10^5\,\mathrm{s}) = 8.7 \cdot 10^{19}$, $I_{max}(\epsilon = 1\,\mathrm{keV}, T = 10^5\,\mathrm{s}) = 3.6 \cdot 10^{18}$, $I_{max}(\epsilon = 1\,\mathrm{eV}, T = 0\,\mathrm{s}) = 1.0 \cdot 10^{15}$ and $I_{max}(\epsilon = 1\,\mathrm{keV}, T = 0\,\mathrm{s}) = 1.3 \cdot 10^{14}$.

quite similar to the light curves resulting from an instantaneous electron injection (dashed lines), but as expected is its maximal amplitude $T/1\,\mathrm{s}$ times bigger since $T/1\,\mathrm{s}$ times as many relativistic electrons are injected into the emission volume. In addition, the synchrotron flare temporally extends, so that the temporal features (4.36)–(4.39) are delayed about T and hence

$$t_{max}(\epsilon < \epsilon_b) \simeq \frac{R}{c} + \frac{1}{D_s \gamma_0}\left(\sqrt{\frac{E_0}{3\epsilon}} - 1\right) + t_0 + T\,. \tag{4.45}$$

$$t_{max}(\epsilon > \epsilon_b) \simeq \frac{c_l(\epsilon)}{D_s\,\gamma_0}\left(\sqrt{\frac{E_0}{\epsilon}} - 1\right) + t_0 + T\,, \tag{4.46}$$

$$t_{1/2}(\epsilon < \epsilon_b) \simeq \frac{R}{c} + \frac{2.02}{D_s\,\gamma_0}\sqrt{\frac{E_0}{3\epsilon}} + t_0 + T\,, \tag{4.47}$$

$$t_d(\epsilon > \epsilon_b) \simeq \frac{2\,R}{c} + \frac{1}{D_s\,\gamma_0}\left(\sqrt{\frac{E_0}{\epsilon}} - 1\right) + T\,. \tag{4.48}$$

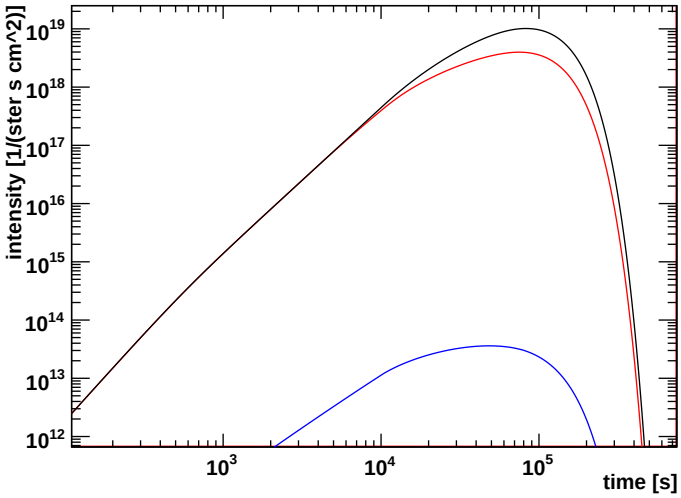

Figure 4.9: Synchrotron light-curves of optical photons ($\epsilon = 1\,\mathrm{eV}$) resulting from a homogeneous electron injection over the outer shell of the plasmoid ($r_1 \leq r \leq R$) and an injection duration of $T = 10^4\,\mathrm{s}$. It is illustrated for $r_1 = 0.9999\,R$ (blue line), $r_1 = 0.9\,R$ (red line) and $r_1 = 0$ (black line) with the default parameters in the full diffusion limit.

Fig. (4.9) shows the temporal development of the emergent synchrotron intensity, calculated by Eq. (4.44) with the spatial injection coefficient (3.33). Like in the previous sections, the amplitude of the light curves increase with increasing r_1, but neither the flare duration nor the time of maximal intensity is changed by this spatial injection assumption.

4.5 Synchrotron radiation with respect to excitation losses

The latter sections have exposed the importance of the broadband nature of the synchrotron power spectrum, as well as the mostly negligible influence of the different particle injection assumptions on the temporal development of a synchrotron flare. Below, another generalization is used: On the one hand, the influence of excitation losses on the relativistic electrons is investigated and on the other hand are the effects of the self excited electrostatic turbulences on the particle beam taken into account. However, the temporal behavior of the emergent synchrotron intensity is not expected to change significantly at photon energies $\epsilon > E_q$, since the temporal flare development is predominantly determined by the broadband nature of the synchrotron power spectrum, as well as the synchrotron

and EC cooling rate, respectively. But in case of $\epsilon < E_q$ a reduction of the synchrotron flare is anticipated because of the additional cooling effect.

4.5.1 Emergent synchrotron intensity by an instantaneous injection of electrons with plateau distributed energy

Here the relativistic electrons are quasi instantaneously plateau distributed in momentum space according to Eq. (3.28), so that the spontaneous synchrotron emission coefficient (4.3) yields

$$\begin{aligned} j_s(r,t,\epsilon) =& \frac{P_0\, q_0}{4\pi\, h(\gamma_0-1)} \left(\frac{\epsilon}{\epsilon_s}\right)^{\frac{1}{3}} \sum_{k=1}^{\infty} b_k \int_0^R dr' \, \frac{\sin(\lambda_k r)}{r} \\ & \times\, H[t-t_0]\, H\left[t_0 + \frac{1}{D_s\gamma_q} \arctan\left(\frac{\gamma_0\gamma_q-\gamma_q}{\gamma_q^2+\gamma_0}\right) - t\right] \\ & \times \int_1^{\gamma_u(t)} \mathrm{d}\gamma\, \gamma^{-\frac{2}{3}} \, \frac{1+(\gamma_{t,0}/\gamma_q)^2}{1+(\gamma/\gamma_q)^2} \, \frac{E_k^e(\gamma,\gamma_{t,0})}{\exp\left(\epsilon/(\epsilon_s\gamma^2)\right)}\,, \end{aligned} \tag{4.49}$$

where $\gamma_{t,0} = \gamma_t(\gamma,\, t,\, t'=t_0)$ and the upper limit of integration is due to the Heaviside function in Eq. (3.28) defined by

$$\gamma_u(t) = \frac{\gamma_q\gamma_0 - \gamma_q^2 \tan(D_s\gamma_q(t-t_0))}{\gamma_q + \gamma_0 \tan(D_s\gamma_q(t-t_0))}\,. \tag{4.50}$$

The omnidirectional photon production rate (4.17) is specified by Eq. (4.49), so that the emergent synchrotron intensity (4.16) is finally determined by

$$\begin{aligned} I_{Sy}(R,\epsilon,t) =& \frac{P_0\, q_0}{2Rh(\gamma_0-1)} \left(\frac{\epsilon}{\epsilon_s}\right)^{\frac{1}{3}} \sum_{k=1}^{\infty} b_k \int_0^R dr' \, \sin(\lambda_k r') \\ & \times \int_{R-r'}^{R+r'} \frac{ds}{s}\, H[c(t-t_0)-s]\, H\left[s - c\left(t - t_0 - \frac{1}{D_s\gamma_q}\arctan\left(\frac{\gamma_0\gamma_q-\gamma_q}{\gamma_q^2+\gamma_0}\right)\right)\right] \\ & \times \exp\left(-\frac{g(x)\, s}{R}\right) \int_1^{\gamma_u(t-s/c)} \mathrm{d}\gamma\, \gamma^{-\frac{2}{3}} \, \frac{1+(\gamma_{ret}/\gamma_q)^2}{1+(\gamma/\gamma_q)^2} \, \frac{E_k^e(\gamma,\gamma_{ret})}{\exp\left(\epsilon/(\epsilon_s\gamma^2)\right)}\,, \end{aligned} \tag{4.51}$$

with

$$\gamma_{ret} = \gamma_t(\gamma,\, t=t-s/c,\, t'=t_0) = \frac{\gamma_q\gamma + \gamma_q^2 \tan(D_s\gamma_q(t-t_0-s/c))}{\gamma_q - \gamma \tan(D_s\gamma_q(t-t_0-s/c))}\,, \tag{4.52}$$

which denotes the retarded $\gamma_{t,0}$. Once again, the Heaviside functions split the integral expression in several integrands (Appendix D), that can finally be solved by a numerical algorithm of integration. Like in the previous sections a 40-point Gaussian quadrature rule is the most stable algorithm, that yields accurate results, as the integrand is most likely adequate described by a polynomial of order 79.
The Fig. 4.10 shows the obtained emergent synchrotron intensity and compares it with the results of an instantaneous injection of monoenergetic electrons disregarding excitation

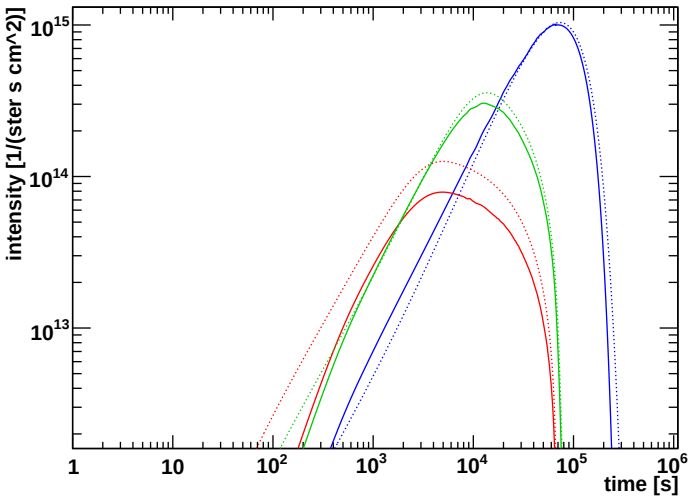

Figure 4.10: Temporal development of the emergent synchrotron intensity at an energy $\epsilon = 1\,\mathrm{eV}$ (blue line), $\epsilon = 100\,\mathrm{eV}$ (green line) and $\epsilon = 1\,\mathrm{keV}$ (red line) according to Eq. (4.51, solid line) and Eq. (4.28, dotted line) where a monoenergetic particle injection as well as no excitation losses are considered. In doing so, the default parameters in the full diffusion limit are used.

losses. Apparently, the additional assumptions have no influence on the temporal flare development of synchrotron photons with $\epsilon > E_q$, so that the Eq. (4.45)–(4.48) still give an accurate description of the flare duration and the time of maximal emission. However, in the case of $\epsilon < E_q$, which also occurs by increasing the background particle density N_b or decreasing the synchrotron and EC losses, the light curves in the affected energy range are shortened significantly. Here, the previously derived analytical formulas of the temporal features are not suitable.

4.6 Conclusions to the low energy data of PKS 2155-304

The previous sections have shown that the temporal development of a synchrotron flare differs at different energies due to the cooling time of the relativistic electrons. Hence, the flare duration, as well as the time of maximal emission increase (independent of the initial conditions of the seed electrons) with decreasing energy. In the following, the derived temporal features (4.45)–(4.48) are considered in the observer's frame (see Appendix A for the relevant invariance relations) and subsequently compared with the optical and X-ray observations of PKS 2155-304 in July 29-30 2006 (Fig. 4.11).
The observations of PKS 2155-304 in the optical V-band ($\epsilon_V^* = 10\,\epsilon_V\,\delta_1 = 2.25\,\mathrm{eV}$) show an increase starting at ∼20:30 on the 29th of July, that lasts several hours until ∼23:45 on the same day, but afterwards the flux hardly decrease and another peak is formed at ∼02:00 on the next day with a distinct subsequent slope. Thus, the minimal optical flare duration yields $t^*_{1/2,obs}(\epsilon_V^*) \geq 6.25\,\mathrm{hr}$, when the rising at ∼02:45 refers to another flare and the time of maximal flare emission is assumed to be dated somewhere between ∼23:45 and

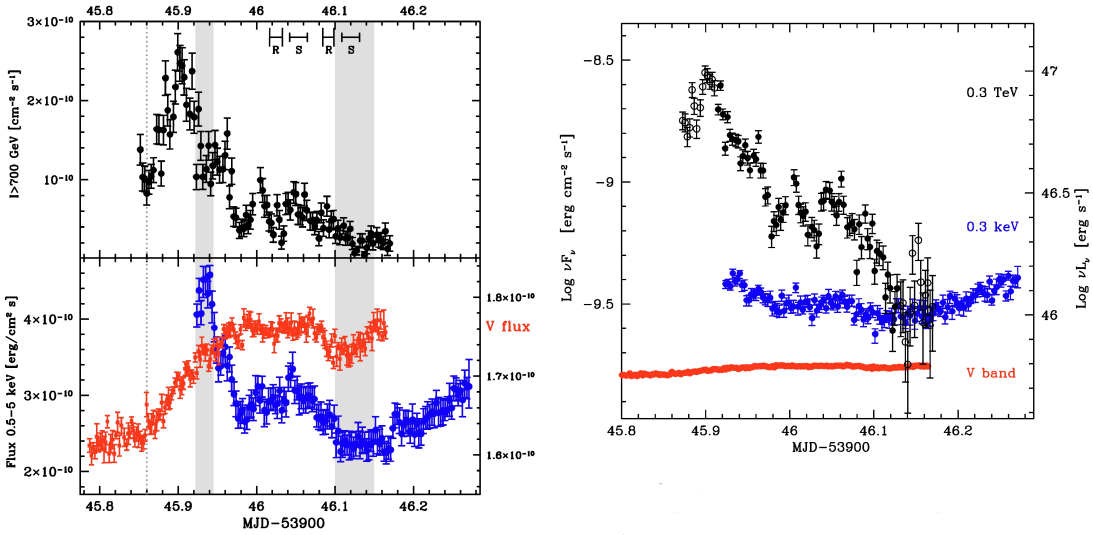

Figure 4.11: The optical (red), X-ray (blue) and γ-ray (black) light curves of PKS 2155-304 in July 29-30 2006. The *left panel* illustrates the observed flux at different scales in order to emphasize the temporal pattern in all wavelengths and the dotted line marks the starting time of the optical and γ-ray flare. In the *right panel* are the light curves of the flux at 0.3 TeV, 0.3 keV and 2.25 eV plotted on the same flux scale. Here the X-ray and optical flux are corrected for Galactic extinction ($A_V = 0.071$). For more details see Aharonian et al. (2009).

$\sim$02:00.
Unfortunately, the X-ray observations (with $\epsilon^*_X = 10\,\epsilon_X\,\delta_1 = \{0.5...5\}\,\mathrm{keV}$) starts almost at its flux maximum $\sim 2\,\mathrm{hr}$ after the onset of the optical flare. However, there is a clear correlation to the VHE flux during the whole time of observation and therefore the X-ray flare is assumed to behave similar to the VHE flux in these first two hours of missing data, too. Hence, the first three X-ray data points show probably rather a short time fluctuation (similar to the VHE data at that time) than a long scale slope. Consequently, the X-ray flux is considered to start simultaneously with the VHE flare (as well as the optical flare) at 20:38 on the 29th of July and have its maximum approximately at the same time as the VHE flare at $\sim$21:30 on the 29th of July. Right after the beginning of the X-ray observations the flux sharply decreases appropriate to the third root of the VHE flux (Aharonian et al., 2009), so that the X-ray flare duration yields at least 2 hours.
According to the previous interpretation of the low energy data the theoretical model has to account for the following temporal conditions: (i) The observed time lag between the flux maxima of the optical and X-ray light curves yields $2.25\,\mathrm{hr} \leq \Delta t^*_{obs} \leq 4.5\,\mathrm{hr}$, (ii) the maximal X-ray emission is supposed to be $\sim 1\,\mathrm{hr}$ after the beginning of the flare, and (iii) the lower limits of the flare duration are $t^*_{d,obs}(\epsilon^*_X) \geq 2\,\mathrm{hr}$, as well as $t^*_{1/2,obs}(\epsilon^*_V) \geq 6.25\,\mathrm{hr}$. Due to the large Compton dominance ($L_c/L_s \sim 10$) of this BL Lac object (Aharonian et al., 2009), dominant EC losses are assumed, so that $l_{EC} \gg b^2$. Furthermore, a Doppler factor $\delta = 10\,\delta_1$ is adopted, since the emission knot is transparent for TeV photons (Appendix F).

Using the Eq. (4.36) and (4.38) for an injection duration $T \ll R/c$ the delay between the peaks of the optical and the X-ray light curves in the observer's frame yields

$$\begin{aligned}\Delta t^* &= \frac{t_{max}(\epsilon_V^* < \epsilon_b^*) - t_{max}(\epsilon_X^* > \epsilon_b^*)}{10\,\delta_1} \\ &\simeq \Big(56\,R_{15}\,\delta_1^{-1} + \big[308\,(\epsilon_V^*/1\,\mathrm{eV})^{-\frac{1}{2}} - 0.2\,(\epsilon_X^*/1\,\mathrm{keV})^{\frac{1}{2}} \\ &\qquad - 30\,(\epsilon_X^*/1\,\mathrm{keV})^{-\frac{1}{2}}\big]\,l_{EC}^{-1}\,b^{1/2}\delta_1^{-1/2}\Big)\ \text{minutes},\end{aligned} \tag{4.53}$$

when $l_{EC} \gg b^2$, as well as $\sqrt{E_0^*/\epsilon_X^*} \gg 1$. Consequently, the EC cooling parameter becomes

$$l_{EC} \simeq \left(\frac{\frac{\Delta t^*_{obs}}{1\,\text{minutes}} - 56\,R_{15}\delta_1^{-1}}{205 - 30(\epsilon_X^*/1\,\mathrm{keV})^{-\frac{1}{2}}}\right)^{-1} b^{1/2}\,\delta_1^{-1/2} \tag{4.54}$$

in order to obtain the observed time lag Δt^*_{obs} according to the condition (i). In addition, the constraint (ii) determines the time of maximal X-ray emission, so that with Eq. (4.36) in the observer's frame

$$t^*_{max}(\epsilon_X^*) \simeq \frac{\left(10\,(\epsilon_X^*/1\,\mathrm{keV}) + 1.83\cdot 10^3\right)\,\mathrm{s}}{\delta_1^{1/2} b^{-1/2} l_{EC}\,(\epsilon_X^*/1\,\mathrm{keV})^{1/2}} \simeq 3.6\cdot 10^3\,\mathrm{s}\,, \tag{4.55}$$

when $l_{EC} \gg b^2$ and $\sqrt{E_0^*/\epsilon_X^*} \gg 1$ is still taken into account. Thus, the EC cooling parameter yields

$$l_{EC} \simeq 0.51\,b^{1/2}\,\delta_1^{-1/2}(\epsilon_X^*/1\,\mathrm{keV})^{-1/2} \tag{4.56}$$

for the considered X-ray energies $0.5\,\mathrm{keV} \leq \epsilon_X^* \leq 5\,\mathrm{keV}$. Equalizing this term with the Eq. (4.54) results in

$$\Delta t^*_{obs} = (56\,R_{15}\delta_1^{-1} + 402(\epsilon_X^*/1\,\mathrm{keV})^{1/2} - 59)\,\text{minutes}\,. \tag{4.57}$$

A physically meaningful solution requires $R_{15}\delta_1^{-1} > 0$ and with the time lags referred to (i), one finally obtains

$$0 < R_{15}\delta_1^{-1} \leq 5.87 - 7.18(\epsilon_X^*/1\,\mathrm{keV})^{1/2}\,, \quad \text{where } \epsilon_X^* \leq 0.67\,\mathrm{keV}\,. \tag{4.58}$$

Furthermore, the total duration (4.37) of the X-ray flare, as well as the half-life (4.39) of the flare in the V-band yields with Eq. (4.56), as well as an injection duration $T \ll 10\,R_{15}$ hr

$$t_d^*(\epsilon_X^*) \simeq \Big(111\,R_{15}\,\delta_1^{-1} + 33\Big)\ \text{minutes}\,, \tag{4.59}$$

and

$$t^*_{1/2}(2.25\,\mathrm{eV}) \simeq \Big(56\,R_{15}\,\delta_1^{-1} + 831(\epsilon_X^*/1\,\mathrm{keV})^{1/2}\Big)\ \text{minutes}\,, \tag{4.60}$$

respectively, in the observer's frame. In order to obey the minimal flare durations according to (iii) the Eq. (4.59) yields $R_{15}\delta_1^{-1} \geq 0.78$, so that all in all, the temporal flare development of the optical and X-ray flare is accurately described when

$$0.78 \leq R_{15}\delta_1^{-1} \leq 5.87 - 7.18(\epsilon_X^*/1\,\mathrm{keV})^{1/2}\,, \qquad \text{where } \epsilon_X^* \leq 0.50\,\mathrm{keV} \tag{4.61}$$

and the EC cooling parameter is determined by Eq. (4.56).
According to the strong slope in the X-ray spectrum, the photons with the lowest X-ray energies provide the dominant rate of the observed X-ray flux, so that the energetic confinement in Eq. (4.61) is in good agreement with the observations. However, the time lag between the maxima of the optical and X-ray light curves needs to be at least 4.5 hr when the maximal X-ray emission is about an hour after the beginning of the flare. But assuming a higher background particle density, excitation losses have to be taken into account, so that the time lag is decreased significantly, since the temporal features of the optical flare decrease (see Fig. 5.4) through the additional cooling effect. Based on the narrow range of the parameters R_{15}, δ_1, l_{EC} and b that accounts for the temporal flare development the ratio between the maxima of the emergent intensity (4.28) at $\epsilon_X^* = 0.3\,\mathrm{keV}$ and $\epsilon_V^* = 2.25\,\mathrm{eV}$ yields

$$I_{max}(\epsilon_X^* = 0.3\,\mathrm{keV})/I_{max}(\epsilon_V^* = 2.25\,\mathrm{eV}) \simeq 0.1\,. \tag{4.62}$$

The observed flux at a certain energy ϵ_c^* is defined by $F^* \propto \epsilon_c^*\, I^*(\epsilon_c^*)$ and with Eq.(4.62) one obtains

$$F_X^*/F_V^* = \frac{0.3\,\mathrm{keV}}{2.25\,\mathrm{eV}} \frac{I_{max}(\epsilon_X^*)}{I_{max}(\epsilon_V^*)} \simeq 13.3\,. \tag{4.63}$$

Hence, the theoretical flux ratio is exactly in line with the observations, as the measured flux at 0.3 keV varies about a factor 2, whereas the flux variation factor at 2.25 eV is only 0.15, so that its quotient also yields ~ 13.
Summing up, the theoretical model reasonably describes the flux variation ratio, as well as the temporal development of the major flare in the X-ray and the V-band of PKS 2155-304 on the 29th and 30th of July 2006 for realistic parameters that account for the Compton dominance of the source.

Chapter 5
Modeling high energy flares

As discussed in Sect. 1.1.1 and 1.1.2, the high energy flare is commonly explained by a leptonic or hadronic interaction scenario. Due to the mathematical complexity of SSC scattering the leptonic emission approach is in this thesis confined to the case of EC scattering, which refers to a dominant external photon field or an initial particle density $q_0 < 10^9\, R_{15}^{-1}\, \gamma_0^{-2}$ (Schlickeiser et al., 2010).
The considered pickup model where no further particle acceleration in the emission knot takes place yields rather small particle Lorentz factors, so that in consideration of the constraints (3.57) and (3.60), the relativistic protons can only generate gamma-rays by pion production through inelastic proton-proton interactions.

5.1 Propagation and retardation of gamma-rays and neutrinos

The production of high energy photons that results from EC scattering (pion production by inelastic proton-proton interactions) depends on the particle density (3.51) of relativistic electrons (particle density (3.63) of relativistic protons), as well as the properties of the external target photon field (the internal target proton field) and the corresponding cross-section. In addition to the generation of γ-rays, the hadronic pion production generates high energy neutrinos. Latter interact in contrast to the gamma-rays not by the electromagnetic force, but nevertheless both particle species can be treated by the same escape probability as subsequently shown. The background particle density of the plasmoid volume corresponds to a high vacuum, so that neutrino interactions are negligible without any difficulty. In the high energy regime where the dimensionless photon energy $x = E_\gamma / m_e c^2 \gg 1$, the photons are predominantly forward scattered. However, a single scattering event leads to a large energy shift, which approximately removes the γ-ray in proportion to its probability for scattering (Lightman & Zdziarski, 1987), that is described by the Klein-Nishina scattering depth (4.13) which yields $\tau_{KN}(x \gg 1) \ll 1$. Thus, a diffusive buildup of photons in the interior of the emission volume can not occur at γ-ray energies and the photon escape probability is dominated by the escape from the emission knot in a time $\sim R/c$. Therefore, the Eq. (4.12) results in $g(x) = 1$ and the escape probability is calculated by $\exp(-s/R)$ when high energy photons (with $x \geq 1$) or neutrinos are considered.

Consequently, the emergent intensity of gamma-rays ($j = \gamma$) and neutrinos ($j = \{\nu_e, \nu_\mu\}$), respectively, for an optical thin emission volume is determined, analogous to the case of the emergent synchrotron intensity (4.16), by

$$I_j(R, E_j, t) = \frac{1}{2R} \int_0^R \mathrm{d}r'\, r' \int_{R-r'}^{R+r'} \frac{\mathrm{d}s}{s}\, \rho_l(r', E_j, t - s/c)\, \exp(-s/R)\,. \tag{5.1}$$

Here $\rho_l(r', E_j, t - s/c)$ denotes the omnidirectional production rate of γ-rays or neutrinos with an energy E_j according to the considered leptonic EC scattering or hadronic pion production.
The previous examinations of the synchrotron radiation have already exposed the influence of the different initial particle distributions on the temporal development of the flare. Hence, the different initial particle approaches are not reapplied in the case of high energy emission, since its general influence is expected to stay the same. So, the subsequent investigations are confined to the favored case of an instantaneous and homogeneous injection into the whole plasmoid volume (3.32) of relativistic electrons and protons with a plateau distributed energy distribution (3.28) due to the influence of electrostatic turbulence. In doing so, the mathematical complexity of the leptonic and hadronic interaction, respectively, allows no analytical treatment.

5.2 External Compton radiation

5.2.1 Spontaneous external Compton emission

In this thesis a low number density of injected particles is considered in order to keep the nonlinear effects of SSC losses on the relativistic electron distribution negligible. Consequently, a significant γ-ray flare by inverse Compton scattering has to be initiated by an external photon field. Here, the photon field of the accretion disk is considered with a temperature $\theta' = 10\,\theta'_1$ eV and a Planckian distributed spectral luminosity (Dermer & Schlickeiser, 1993b)

$$L'(\epsilon') = \frac{15\, L_{ad}\, m_e c^2}{\pi^4\, \theta'^4}\, \frac{\epsilon'^3}{\exp\left(\frac{\epsilon'}{\theta'}\right) - 1} \tag{5.2}$$

where the total luminosity $L_{ad} = 10^{46}\, L_{46}\, \mathrm{erg\ s^{-1}}$. As shown in Sikora et al. (1994) the radiation field becomes at a large distance from the central engine a significant non-radial component as a result of scattering and reprocessing effects. Gas clouds and dust are assumed to be spherically distributed around the central nucleus, so that a roughly isotropic radiation field is obtained by line and thermal infrared emission of irradiated clouds and dust, respectively, as well as electron scattering in clouds and the intercloud medium. Subsequently, the latter mechanism is favored and hence, the photon density $n'_{Ph}(\epsilon')$ at a distance $\sqrt{R_{sc}^2 + R^2}$ is determined by

$$n'_{Ph}(\epsilon') = \frac{L'(\epsilon')\, \tau_{sc}}{4\pi\, (R_{sc}^2 + R^2)\, c\, \epsilon'}\,. \tag{5.3}$$

Here the parameters are the same as in Eq. (3.40) where the distance of significant scattering is given by $R_{sc} = 1\, R_{pc}$ pc and $\tau_{sc} = 10^{-2}\, \tau_{-2}$ denotes the mean scattering depth.

In the (unprimed) frame of the emission knot with a Doppler factor $\delta = 10\,\delta_1$ the external photon density yields (Dermer & Schlickeiser, 1993a)

$$n_{Ph}(\epsilon) = n_0 \frac{\epsilon^2}{\exp\left(\frac{\epsilon}{\theta}\right) - 1}\,, \tag{5.4}$$

with

$$n_0 = 1.4 \cdot 10^{10} \frac{\tau_{-2}\, L_{46}\, \delta_1^2}{\theta_1^4\,(R_{pc}^2 + R_{15}^2)}\,\mathrm{eV}^{-2}\mathrm{cm}^{-3} \tag{5.5}$$

and has a spectral maximum at

$$\epsilon_{max} \simeq 1.59\,\theta\,. \tag{5.6}$$

Integration of the photon density (5.4) according to Eq. (2.24) yields the previously used photon energy density (3.40).
Using the convenient δ-function approximation for inverse Compton scattering (Dermer & Schlickeiser, 1993a) in the limit $\gamma \gg 1 \gg \epsilon/(m_e c^2)$ the spontaneous EC emission coefficient results in

$$j_c(r, E_\gamma, t) = \frac{E_\gamma c \sigma_T}{12\pi^2\, m_e c^2} \int_0^\infty d\epsilon\, n_{ph}(\epsilon) \int_0^{m_e c^2/\epsilon} d\gamma\, n_e(r, \gamma, t) \delta\left(E_\gamma - \gamma^2 \epsilon\right)\,. \tag{5.7}$$

Hence, the scattering is most efficient when the relativistic electrons have a Lorentz factor $\gamma = \sqrt{E_\gamma/\epsilon}$.

5.2.2 Emergent gamma-ray intensity

According to Eq. (5.1) the emergent intensity of EC scattered photons at a time t and an energy E_γ is calculated by

$$I_{EC}(R, E_\gamma, t) = \frac{1}{2\,R} \int_0^R dr'\, r' \int_{R-r'}^{R+r'} \frac{\mathrm{d}s}{s}\, \rho_\gamma(r', E_\gamma, t - s/c)\, \exp\left(-s/R\right)\,. \tag{5.8}$$

Here the omnidirectional photon production rate is determined by

$$\rho_\gamma\left(r', E_\gamma, t - \frac{s}{c}\right) = 4\pi\, j_c\left(r', E_\gamma, t - \frac{s}{c}\right)\,, \tag{5.9}$$

since there is no preferred direction of the emergent gamma-ray intensity, as the relativistic electron, as well as the external photon distribution are spatially isotropic. Inserting the relativistic electron density (3.51) and including the Heaviside functions in the innermost integral, the emergent γ-ray intensity by EC scattering results in

$$\begin{aligned} I_{EC}(R, E_\gamma, t) = {} & \frac{\sqrt{E_\gamma}\, c\, \sigma_T\, q_0\, n_0}{12\pi\, R\, m_e c^2 (\gamma_0 - 1)} \sum_{k=1}^{\infty} b_k \int_0^R dr'\, \sin(\lambda_k r') \int_{R-r'}^{R+r'} \frac{ds}{s}\, H[c(t - t_0) - s] \\ & \times H\left[s - c\left(t - t_0 - \frac{1}{D_s \gamma_q} \arctan\left(\frac{\gamma_0 - \frac{E_\gamma}{m_e c^2}}{\frac{E_\gamma}{m_e c^2}\frac{\gamma_0}{\gamma_q} + \gamma_q}\right)\right)\right] \exp\left(-\frac{g(x)\, s}{R}\right) \\ & \times \int_{\epsilon_1(E_\gamma, t-s/c)}^{\epsilon_2(E_\gamma)} d\epsilon\, \epsilon^{\frac{3}{2}}\, \frac{E_k^e(\sqrt{E_\gamma/\epsilon}, \gamma_t(\sqrt{E_\gamma/\epsilon}, t - s/c))}{\exp(0.1\epsilon/\theta_1) - 1}\, \frac{\gamma_q^2 + \gamma_t^2(\sqrt{E_\gamma/\epsilon}, t - s/c)}{\gamma_q^2 + E_\gamma/\epsilon}, \end{aligned}$$

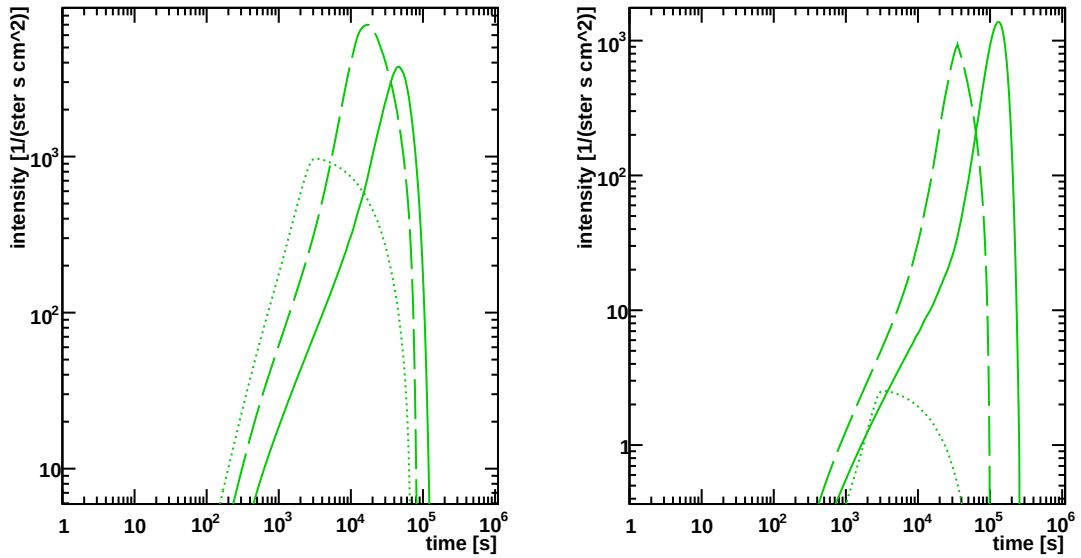

Figure 5.1: Temporal development of the emergent gamma-ray intensity by EC scattering at an energy $E_\gamma = 1\,\mathrm{GeV}$ (solid line), $E_\gamma = 10\,\mathrm{GeV}$ (dashed line) and $E_\gamma = 100\,\mathrm{GeV}$ (dotted line). Furthermore, we used an accretion disk temperature of $\theta_1 = 0.1$(left panel) and $\theta_1 = 1$, respectively, as well as the default parameters in the full diffusion limit.

(5.10)

when the considered energies are in the Thomson limit $4\sqrt{\epsilon\, E_\gamma} \ll m_e c^2$. Here the Heaviside functions yield the integration limits

$$\epsilon_1(E_\gamma, t - s/c) = E_\gamma \left(\frac{\gamma_0\gamma_q - \gamma_q^2 \tan(D_s\gamma_q(t - s/c - t_0))}{\gamma_q + \gamma_0 \tan(D_s\gamma_q(t - s/c - t_0))} \right)^2 , \tag{5.11}$$

as well as

$$\epsilon_2(E_\gamma) = m_e^2 c^4 / E_\gamma \,. \tag{5.12}$$

Subsequently, the Heaviside functions are charged against the integration limits corresponding to Appendix D and the resulting integral expression can be solved numerically. Therefore, a N-point Gaussian quadrature is used, where a trial-and-error method comparable to Fig. (4.5) yields suitable solution for $N = 40$. Fig. 5.1 shows that the temporal development of the emergent EC intensity is similar to the case of synchrotron radiation and the time of maximal flare emission, as well as the flare duration increases with decreasing photon energy E_γ. Furthermore, with increasing disk temperature θ the amplitude of the light curves decreases and the time of maximal flare emission shifts to later times, as well as the flare duration enlarges (especially at low gamma energies E_γ), due to the spectral dependence (5.6) of the maximal external photon density and the δ-approximation in Eq. (5.7).

5.3 Radiation by inelastic p-p interactions

5.3.1 Production rate of gamma-rays and neutrinos

In the following the relativistic protons of Eq. (3.63) with the energy $E_p = \gamma m_p c^2$ and their interactions with the non-relativistic protons of the background plasma of constant density $N_b \gg q_0$ are considered, so that one obtains a significant pion production rate.
Referred to Kelner et al. (2006) the resulting energy spectrum of the secondary pions of energy E_π and the ratio $x = E_\pi/E_p$ of the transferred energy is analytically well decribed, with an accuracy better than 10 % in the proton energy range $0.1\,\mathrm{TeV} \leq E_p \leq 10^5\,\mathrm{TeV}$, by

$$F_\pi(x,\, E_p) = 4\alpha B_\pi x^{\alpha-1} \left(\frac{1-x^\alpha}{1+rx^\alpha(1-x^\alpha)}\right)^4 \left(\frac{1}{1-x^\alpha} + \frac{r(1-2x^\alpha)}{1+rx^\alpha(1-x^\alpha)}\right) \sqrt{1-\frac{m_\pi}{x\,E_p}}\,, \tag{5.13}$$

with the fit parameters $B_\pi = a + 0.25$, $\alpha = 0.98\,a^{-1/2}$ and $r = 2.6\,a^{-1/2}$, where

$$a = 3.67 + 0.83\,\ln(E_p/1\,\mathrm{TeV}) + 0.075\,[\ln(E_p/1\,\mathrm{TeV})]^2\,. \tag{5.14}$$

In addition, a less significant rate of η-mesons is also produced, which can analytically be approximated (with a somewhat less accuracy) by

$$F_\eta(x,\, E_p) = (0.55 + 0.028\,\ln x)\left(1-\frac{m_\eta}{x\,E_p}\right) F_\pi(x,\, E_p) \tag{5.15}$$

with the condition $F_\eta(x,\, E_p) = 0$ at $x < m_\eta/E_p$. The presented energy spectra (5.13) and (5.15) are obtained by using numerical simulations of the SIBYLL code.
Both meson species decay quasi instantaneously. The main decay modes of the pion are already given in (1.2) and the main decay modes of the η-meson are presented by (Eidelman et al. 2004)

$$\eta \rightarrow \begin{cases} 2\gamma, & \text{with a probability of } 39,4\%, \\ 3\pi^0, & \text{with a probability of } 32,5\%, \\ \pi^+\pi^-\pi^0, & \text{with a probability of } 22,6\%, \\ \pi^+\pi^-\gamma, & \text{with a probability of } 5\%. \end{cases} \tag{5.16}$$

The energy losses of the intermediate particles (i. e. π-, η-mesons and muons) are negligible, according to their high masses (in reference to the electron mass) and their short mean lifetime. In case of the (longer-living) muons the mean lifetime in the rest frame of the plasmoid yields $\tau_\mu \simeq 2.2\gamma_\mu\,\mu\mathrm{s}$ and the energy losses at high Lorentz factors γ_μ are dominated by synchrotron cooling with the rate $|\dot\gamma|_\mu = 1.3\cdot10^{-9}\,b^2(m_e/m_\mu)^3\,\gamma_\mu^2\,\mathrm{s}^{-1}$. Thus, the mean total muon energy loss Γ_μ can be approximated in first order by

$$\Gamma_\mu \simeq |\dot\gamma|_\mu\,\tau_\mu = 3.3\cdot10^{-22}\,b^2\,\gamma_\mu^3 \tag{5.17}$$

so that the approach $\Gamma_\mu/\gamma_\mu \simeq 0$ is even accurate at the highest considered Lorentz factors ($\gamma_\mu \leq \gamma_0$) when $b \ll 100$.

Finally, the energy spectra $F_j(E_j/E_p, E_p)$ of the decay products ($j = \{\gamma,\, e,\, \nu_e,\, \nu_\mu\}$) are determined after integration of the energy spectrum (5.13) and (5.15), respectively, over the pion energy (see Kelner et al., 2006 for more details). Consequently, the total spectrum of γ-rays, that describes at $x \gtrsim 10^{-3}$ the numerical calculations with an accuracy better than a few percent, yields

$$F_\gamma(x,\, E_p) = B_\gamma \frac{\ln(x)}{x} \left(\frac{1 - x^{\beta_\gamma}}{1 + k_\gamma x^{\beta_\gamma}(1 - x^{\beta_\gamma})} \right)^4 \left[\frac{1}{\ln(x)} - \frac{4\beta_\gamma x^{\beta_\gamma}}{1 - x^{\beta_\gamma}} - \frac{4k_\gamma \beta_\gamma x^{\beta_\gamma}(1 - 2x^{\beta_\gamma})}{1 + k_\gamma x^{\beta_\gamma}(1 - x^{\beta_\gamma})} \right] . \tag{5.18}$$

Here $x = E_\gamma/E_p$ and the best least square fits to the numerical calculations in the energy range $0.1\,\mathrm{TeV} \leq E_p \leq 10^5\,\mathrm{TeV}$ determine the proton energy dependent parameters

$$\begin{aligned} B_\gamma =& 1.30 + 0.14\ln(E_p/1\,\mathrm{TeV}) + 0.011[\ln(E_p/1\,\mathrm{TeV})]^2 , \\ \beta_\gamma =& \left(1.79 + 0.11\ln(E_p/1\,\mathrm{TeV}) + 0.008[\ln(E_p/1\,\mathrm{TeV})]^2\right)^{-1} , \\ k_\gamma =& \left(0.801 + 0.049\ln(E_p/1\,\mathrm{TeV}) + 0.014[\ln(E_p/1\,\mathrm{TeV})]^2\right)^{-1} . \end{aligned} \tag{5.19}$$

The slight imbalance between the generation of π^+ and π^- is below the accuracy of both the measurement and the analytical approximation, so that in the following $\nu = \bar{\nu}$ and $e^+ = e^-$ is adopted. Furthermore, the spectrum of secondary electron-neutrinos is subsequently estimated with good correctness (less than 5 %) by the secondary electrons and thus

$$F_{\nu_e}(x,\, E_p) \simeq F_e(x,\, E_p) = B_e \frac{(1 + k_e[\ln x]^2)^3}{x\,(1 + 0.3/x^{\beta_e})} (-\ln(x))^5 . \tag{5.20}$$

Here $x = E_{\nu_e}/E_p$ and $x = E_e/E_p$, respectively, and the fit parameters yield

$$\begin{aligned} B_e =& \left(69.5 + 2.65\ln(E_p/1\,\mathrm{TeV}) + 0.3[\ln(E_p/1\,\mathrm{TeV})]^2\right)^{-1} , \\ \beta_e =& \left(0.201 + 0.062\ln(E_p/1\,\mathrm{TeV}) + 0.00042[\ln(E_p/1\,\mathrm{TeV})]^2\right)^{-1/4} , \\ k_e =& \frac{0.279 + 0.141\ln(E_p/1\,\mathrm{TeV}) + 0.0172[\ln(E_p/1\,\mathrm{TeV})]^2}{0.3 + (2.3 + \ln(E_p/1\,\mathrm{TeV}))^2} . \end{aligned} \tag{5.21}$$

The spectrum of muon-neutrinos that results directly from $\pi^\pm$-decays is determined by

$$F_{\nu_\mu^{(1)}}(x,\, E_p) = B_\mu \frac{\ln(y)}{y} \left(\frac{1 - y^{\beta_\mu}}{1 + k_\mu y^{\beta_\mu}(1 - y^{\beta_\mu})} \right)^4 \left[\frac{1}{\ln(y)} - \frac{4\beta_\mu y^{\beta_\mu}}{1 - y^{\beta_\mu}} - \frac{4k_\mu \beta_\mu y^{\beta_\mu}(1 - 2y^{\beta_\mu})}{1 + k_\mu y^{\beta_\mu}(1 - y^{\beta_\mu})} \right] , \tag{5.22}$$

where $x = E_{\nu_\mu}/E_p$ and $y = x/0.427$, so that the spectrum cuts off at $x = 0.427$. The fit parameters are given by

$$\begin{aligned} B_\mu =& 1.75 + 0.204\ln(E_p/1\,\mathrm{TeV}) + 0.010[\ln(E_p/1\,\mathrm{TeV})]^2 , \\ \beta_\mu =& \left(1.67 + 0.111\ln(E_p/1\,\mathrm{TeV}) + 0.0038[\ln(E_p/1\,\mathrm{TeV})]^2\right)^{-1} , \\ k_\mu =& 1.07 - 0.086\ln(E_p/1\,\mathrm{TeV}) + 0.002[\ln(E_p/1\,\mathrm{TeV})]^2 . \end{aligned} \tag{5.23}$$

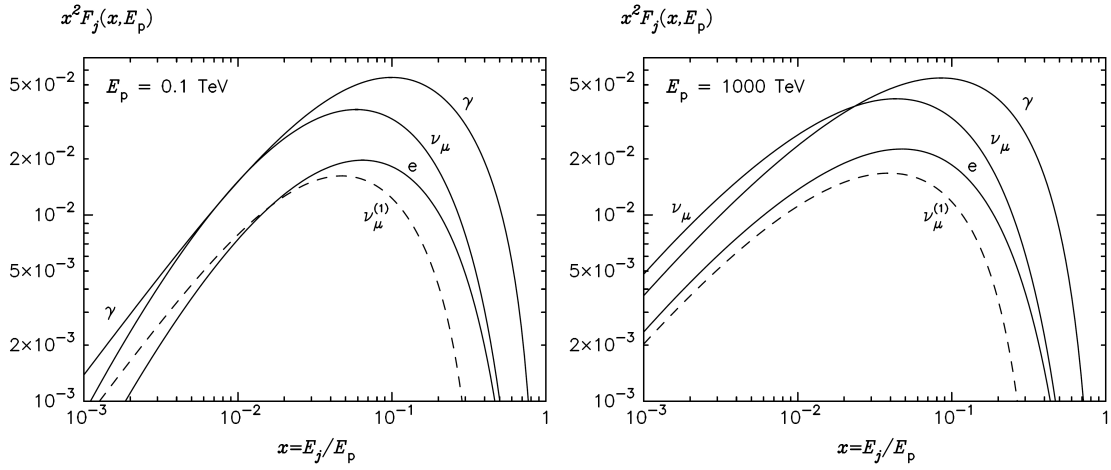

Figure 5.2: Energy spectra of all decay products (electron-neutrino spectra are quasi equal to the electron spectra) produced at inelastic proton-proton interactions when the incident proton has an energy of 0.1 TeV (left panel) and 1000 TeV (right panel), respectively (Kelner et al., 2006).

The spectrum of the resulting muon-neutrinos from the muon decay can be described by Eq. (5.20) and thus, the total muon-neutrino spectrum yields

$$F_{\nu_\mu}(E_{\nu_\mu}/E_p,\, E_p) = F_{\nu_\mu^{(1)}}(E_{\nu_\mu}/E_p,\, E_p) + F_e(E_{\nu_\mu}/E_p,\, E_p)\,. \tag{5.24}$$

Using the energy spectra $F_j(E_j/E_p, E_p)$ of secondary particles in the energy range $E_j \geq 100\,\mathrm{GeV}$, as well as the cross-section (2.43) of hadronic pion production the omnidirectional production rate of the particle species j is calculated by (Kelner et al., 2006)

$$\rho_j^{pp}(r, E_j, t) = c\, N_b \int_{E_j}^{\infty} \frac{dE_p}{E_p}\, \sigma_\pi^{pp}(E_p)\, n_p(r, E_p, t)\, F_j(E_j/E_p, E_p)\,, \tag{5.25}$$

where $n_p(r, E_p, t)$ denotes the isotropic relativistic proton density referred to Eq. (3.63). Due to the mathematical complexity, this first approach neglects additional photon products from the secondary electrons (and positrons), which result from the decay of the generated charged pions. However, as the energy spectra of secondary electrons are with good accuracy approximated by the electron-neutrinos, the temporal behavior of the electron-neutrino intensity shows also when the influence of secondary electrons kicks in.

5.3.2 Emergent intensity of gamma-rays and neutrinos

Using the production rate (5.25) for relativistic protons according to Eq. (3.63), the emergent intensity (5.1) of gamma-rays ($j = \gamma$) and neutrinos ($j = \{\nu_e, \nu_\mu\}$), respectively, with an energy E_j is determined by

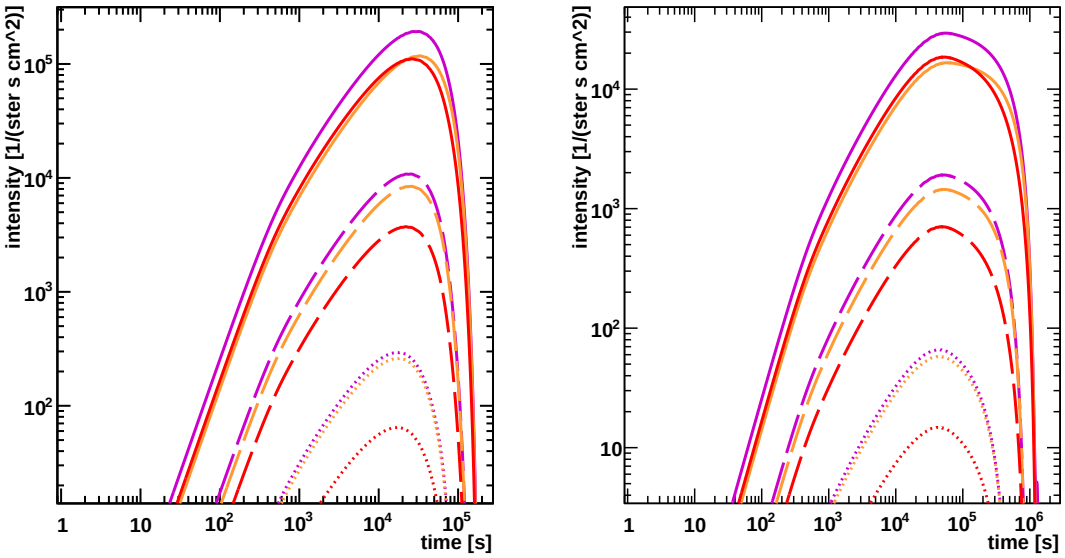

Figure 5.3: Temporal development of the emergent intensity of gamma-rays (red), muon-neutrinos (magenta) and electron-neutrinos (orange) by inelastic p-p interactions with a background particle density of $N_{10} = 10$ (left panel) and $N_{10} = 1$ (right panel), respectively. The emission is considered at an energy $E_l = 0.1\,\mathrm{TeV}$ (solid line), $E_l = 1\,\mathrm{TeV}$ (dashed line) and $E_l = 10\,\mathrm{TeV}$ (dotted line), where the default parameters in the full diffusion limit are used.

$$
\begin{aligned}
I_j^{pp}(R, E_j, t) &= \frac{1}{2\,R} \int_0^R dr'\, r' \int_{R-r'}^{R+r'} \frac{\mathrm{d}s}{s}\, \rho_j^{pp}(r', E_j, t - s/c)\, \exp(-s/R) \\
&= \frac{c\, N_b\, q_0}{2R(\gamma_0 - 1)} \sum_{k=1}^{\infty} b_k \int_0^R dr'\, \sin(\lambda_k r') \int_{R-r'}^{R+r'} \frac{ds}{s}\, H[c(t - t_0) - s] \\
&\quad \times H\left[s - c\left(t - t_0 - \frac{\ln(\gamma_0 m_p c^2 / E_j)}{D_c}\right)\right] \exp(D_c(t - s/c - t_0) - s/R) \\
&\quad \times \int_{E_j}^{E_u(t-s/c)} \frac{dE_p}{E_p}\, \sigma_\pi^{pp}(E_p)\, F_j(E_j/E_p, E_p)\, E_k^p\left(\frac{E_p}{m_p c^2}, \gamma_r\left(\frac{E_p}{m_p c^2}, t - \frac{s}{c}\right)\right),
\end{aligned}
\tag{5.26}
$$

with the upper limit of integration

$$
E_u(t - s/c) = \gamma_0\, m_p c^2\, \exp(-D_c(t - s/c - t_0))\,. \tag{5.27}
$$

Like in the previous sections, the Heaviside functions are charged against the integration limits according to the Appendix D and subsequently the integral is solved accurately (on the same ground as in the previous cases) with a 40-point Gaussian quadrature.
Due to the slower cooling mechanism (3.59) of the relativistic protons, the flare duration

of gammas and neutrinos considerably increases with a decreasing number density N_b of background protons. Furthermore, the flare duration slightly increase with decreasing E_j, which refers to the energy spectra of the secondary particles, whose maximum is around $E_j/E_p \simeq 0.05 - 0.1$, so that the cooling time of relativistic protons increases with decreasing secondary particle energy in order to obtain this quotient for most of the primary particles. However, the time of maximal emission hardly increases with decreasing E_j (see Fig. 5.3). Except for the amplitudes of the emergent intensities there is only a marginal difference in the emission of gammas and neutrinos due to the similar behavior of the energy spectra $F_j(E_j/E_p, E_p)$. However, the logarithmic scaling only exposes huge differences, so that the temporal features become a single issue in the subsequent section.
In order to observe the calculated neutrino flare with the half-completed IceCube 40 detector the muon-neutrino flux has to be above $F_{\nu_\mu} = 10^{-12}\,\phi^{90}_{\nu_\mu}\,\mathrm{TeV}^{-1}\,\mathrm{cm}^{-2}\,\mathrm{s}^{-1}$, where the factor $\phi^{90}_{\nu_\mu}$ has a 90% confidence level and depends on the declination of the neutrino source (Abbasi et al., 2011c). Assuming a Doppler factor of $\delta = 10\,\delta_1$, as well as the distance source-observer of $D = 1\,D_{Mpc}\,\mathrm{Mpc}$, the intensity of neutrinos with an energy $E^*_\nu = \delta\,E_\nu$ in the observers frame yields $I^*_\nu(E^*_\nu) = 1.1 \cdot 10^{-16}\,\delta_1^3\,R_{15}^2\,D_{Mpc}^{-2}\,I_\nu(E_\nu = E^*_\nu/\delta)$ at the detector. A crude comparison with the detection limit demonstrates that the maximal muon-neutrino intensity $I_{\nu_\mu,max}$ has to satisfy the following relation

$$I_{\nu_\mu,max}(E_{\nu_\mu} = E^*_{\nu_\mu}/\delta) \geq 9.1 \cdot 10^3 \phi^{90}_{\nu_\mu}(E^*_{\nu_\mu}/\mathrm{TeV})\,\delta_1^{-3}\,D^2_{Mpc}\,R_{15}^{-2}\,\mathrm{cm}^{-2}\,\mathrm{s}^{-1}\,. \tag{5.28}$$

Using Fig. 5.3 the minimal background proton density in order to obtain a detectable neutrino flare with the energy $E^*_{\nu_\mu} = 1\,\mathrm{TeV}$ of a source at 1 Mpc distance and optimal declination condition ($\phi^{90}_{\nu_\mu} \simeq 1$) yields $N_{10} \simeq 1$. However, the emergent neutrino intensity also increases by increasing the injected proton density q_0, according to Eq. (5.26) and the upper flux limit of the recently completed IceCube 86 detector is expected to decrease slightly (Argüelles, Bustamante & Gago, 2010).

5.4 Time lags

In this section the temporal development of the leptonic and hadronic flares are summarized with a focus on the differences in the time of maximal emission, as well as on the half-life of the flare, i. e. the time at which the emergent intensity is decreased to the half of its maximum. The amplitude of the emergent intensity by the leptonic and hadronic scenarios, respectively, strongly depends on several unknown parameters, like the properties of the emission volume (R, N_b, B) or the external photon field (n_0, θ), the (spatial, temporal and energetic) distribution of seed particles, as well as its particle density q_0. However, the temporal development of the emergent intensity is mainly defined by the parameters B, θ and N_b of the particular cooling and emission process, as well as the size R of the emission volume.
Based on the leptonic and hadronic scenario, respectively, Fig. 5.4 shows the half-life of the emergent intensity and the time of maximal flare emission at an energy range from 1 eV up to 100 TeV for a set of standard parameters. In addition to the temporal features of the high energy flare according to Eq. (5.10) and (5.26), the temporal features of the synchrotron flare based on Eq. (4.51) are illustrated in Fig. 5.4.
The flare duration, as well as the time of maximal emission of each radiation scenario

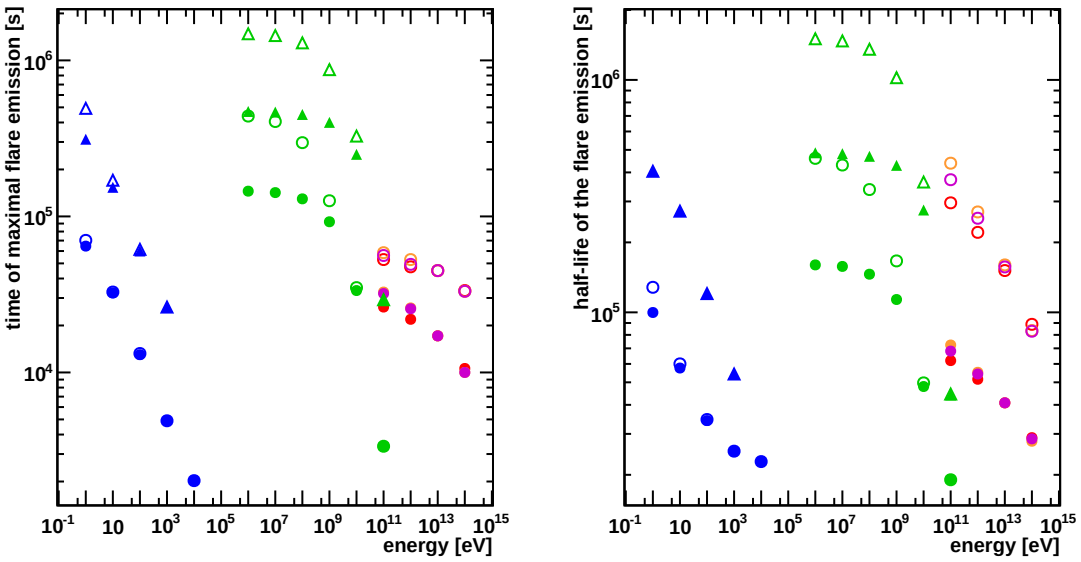

Figure 5.4: Characteristical temporal features of the emission of synchrotron photons (blue symbols), EC gammas (green symbols), as well as gammas (red symbols), muon-neutrinos (magenta symbols) and electron-neutrinos (orange symbols) by inelastic proton-proton interactions. The features are calculated by using two different plasma densities: $N_{10} = 1$ (non-filled symbols) and $N_{10} = 10$ (filled symbols) and in case of the leptonic emission scenario the magnetic field strength is additionally varied, so that $b^2 + l_{EC} \simeq 1$ (circles) and $b^2 + l_{EC} \simeq 0.1$ (triangles), respectively. Furthermore, the default parameters in the full diffusion limit are used.

increases with decreasing photon (neutrino) energy and / or decreasing cooling parameters B and N_b, respectively. Especially, the EC emission gets increasingly delayed at low E_γ with decreasing plasma density N_b, whereas the high energy synchrotron emission is independent of N_b. Furthermore, there is a distinct difference between the hadronic and the leptonic scenario, since the time of maximal emission of gammas and neutrinos by pion production hardly differs by changing the cooling parameter N_b or the energy E_j. The minimal flare duration is limited by the radius of the emission knot due to the light crossing time R/c and the maximal flare duration is limited by the cooling mechanism of the primary particles according to Eq. (3.53) and (3.65), respectively.
Another important feature of Fig. 5.4 is the time lag in the half-life between the neutrino and the gamma-ray emission by p-p interactions, which decreases with increasing cooling and particle density N_b, respectively. So, the spectral half-life development has a steeper decay in the case of neutrinos which probably results from the bigger difference in the maximal value of their energy spectra F_{ν_e} and F_{ν_μ}, respectively, at different proton energies (see Fig. 5.2). In addition, the time of maximal emission shows also a time lag between neutrino and gamma-ray emission but in the same way the slope around the maximal intensity decreases with decreasing cooling parameter N_b (see Fig. 5.3). Thus,

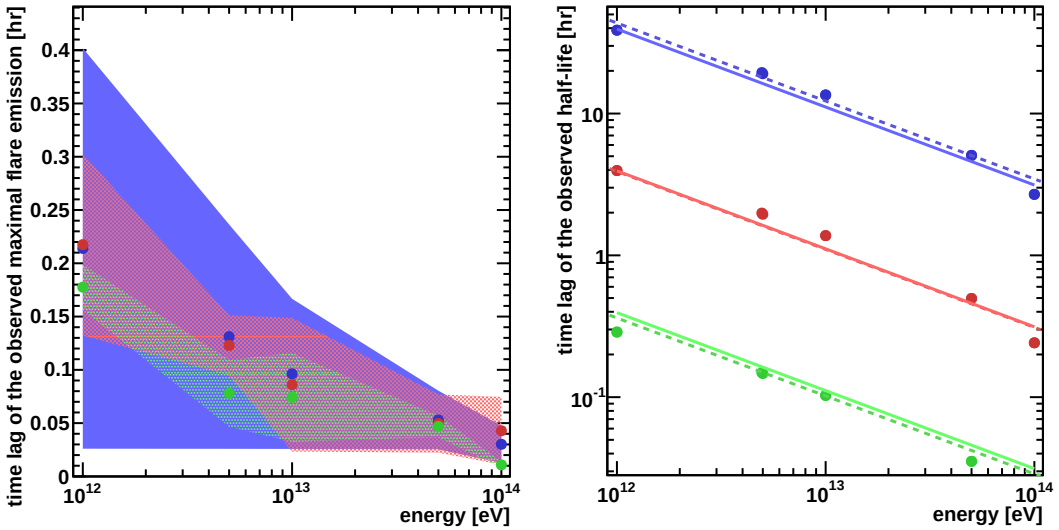

Figure 5.5: Time lags (in the time of maximal flare emission, as well as the half-life of the flare) between gammas and neutrinos from hadronic pion production in the observer's frame with $\delta_1 = 1$. The different colors denote a background particle density of $N_{10} = 0.1$ (blue), $N_{10} = 1$ (red), as well as $N_{10} = 10$ (green) and the corresponding colored areas display the range of error that results from the inaccuracy of the emergent intensity of 1 %. In the right panel the inaccuracy has a vanishing influence. Thus, different power law fits (dashed lines) with the parameters of Tab. 5.1 and the generalized power law according to Eq. 5.29 (solid line) are depicted. The remaining AGN parameters are used in the default setting.

the temporal differences between gamma-rays and neutrinos are predominantly defined by the background particle density. Assuming a rather high particle density in order to obtain an observable neutrino signal (see Sect. 5.3.2), the Fig. 5.5 displays the time lag between gamma-rays and (electron-) neutrinos over their particle energy E_j^* in the observer's frame with a Doppler factor of $\delta = 10\,\delta_1$. Based on neutrino oscillation the neutrino flavor changes while the particle propagates to the observer, so that at large distances (compared to the oscillation length) the initial electron-neutrino is with the same probability detected as muon- or tau-neutrino. Therefore, the time lag between gamma-rays and primary muon-neutrinos, that is according to Fig. 5.4 about a factor of ~ 0.5 smaller, are neglected here. A detailed look at the light curves in Fig. 5.3 shows that an inaccuracy of the emergent intensity of $\sim 1\,\%$ due to the numerical integration algorithm has to be taken into account. Hence, the time at which the intensity differs by 1 % from its maximum and the subsequent half of its maximum, respectively, is used to give an error estimate. So the time lag of the maximal flare emission leads to a huge range of error, especially in the case of a small slope around the maximum of the light curve, which refers to a small background particle density. However, the differences in the half-life of gamma-ray and neutrino flares in the observer's frame can be determined with a range of

Table 5.1: The resulting fit parameters p_0 of a power law approximation of the time lags appropriate to $\Delta t^*_{1/2}(E^*_j) = p_0\, {E^*_j}^{-0.55}$ for three different background particle densities $N_b = 10^{10}\, N_{10}\,\mathrm{cm}^{-3}$.

N_{10}	p_0 [hr]
0.1	$(1.7306 \pm 0.0027) \cdot 10^8$
1	$(1.5560 \pm 0.0018) \cdot 10^7$
10	$(1.4323 \pm 0.0021) \cdot 10^6$

error that is already hidden by the markers. Small time lags $\Delta t^*_{1/2} < 10^{-2}\,\mathrm{hr}$ are neglected due to the limited degree of accuracy of Gaussian quadrature. Using the displayed time lags in the half-life, a trial-and-error method yields an accurate fit by assuming a power law according to $\Delta t^*_{1/2}(E^*_j) = p_0\, {E^*_j}^{p_1}$ with a spectral index $p_1 = -0.55$. The Tab. 5.1 shows the resulting values of p_0, which quasi-linearly depend on the background particle density N_b. Consequently, a general, analytical description of the observed time-lags in the half-life of gamma-ray and neutrino flares is given by

$$\Delta t^*_{1/2}(E^*_j) = 3.9\, N_{10}^{-1} \left(E^*_j / 1\,\mathrm{TeV}\right)^{-0.55}\,\mathrm{hr}\,. \tag{5.29}$$

In a nutshell, at a particle energy of about 1 TeV the maximal neutrino intensity from a flaring AGN with a standard emission radius $R_{15} \simeq 1$ is expected to be delayed, with reference to the γ-ray intensity maximum, for at most half an hour, whereas the half-life of gamma and neutrino emission yields a distinct time lag ranging from several minutes to several hours. At higher energies of some hundreds of TeV the intrinsic time lags between gamma and neutrino emission vanish.
In summary, the Fig. 5.4 and 5.5 demonstrate that the theoretical model yields significant time lags between the light curves that arise from leptonic and hadronic emission scenarios, as well as temporal differences of gammas and neutrinos resulting from hadronic pion production. However, apart from the calculated intrinsic time lags between photons and neutrinos there are two further possible temporal effects on the propagation of these particles, which will be shortly discussed in turn.

5.4.1 Photon-photon pair attenuation of γ-rays

There are several different matter and photon fields of the inter- or extragalactic medium, that can be discussed in reference to the attenuation of the emitted gamma-rays, however, only a temporal correlated and varying particle field can change the general temporal development (flare duration, time of maximal flare emission) of the high energy photon intensity (5.10) or (5.26). Consequently, the number of relevant particle interactions reduces to those that are related to the initial pickup of the relativistic electrons and protons, respectively. Thus, the effect of photon-photon pair attenuation by the low energy synchrotron photons of Sect. 4.4 is investigated. According to the Appendix F, the emission knot is optical thin for gamma-rays independent of the temporal and spatial development of the synchrotron photon density. Hence, an analytical estimation is obtained by

using Eq. (F.13) and neglecting the spatial, temporal and energetic dependence of the synchrotron photon density $M_{Sy} = I_{Sy}/c$, so that the maximal optical depth yields

$$\tau_{\gamma\gamma}^{max} \simeq \frac{2\,\sigma_T\,R\,m_e c^2}{3\,E_\gamma\,c}\,I_{Sy}^{max}\,, \tag{5.30}$$

where I_{Sy}^{max} denotes the maximum of the synchrotron intensity $I_{Sy}(R, \epsilon = 2m_e^2c^4/E_\gamma, t)$. Based on observations of flaring blazars, a maximal luminosity of $L^* \simeq 10^{46}\,\mathrm{erg\,s^{-1}}$ is considered at low synchrotron photon energies and with a Doppler factor $\delta = 10\,\delta_1$ the emergent synchrotron intensity in the frame of the emission knot becomes $I_{Sy}^{max} \simeq 9 \cdot 10^{23}\,(E_\gamma/1\,\mathrm{TeV})\,R_{15}^{-2}\,\delta_1^{-3}\,\mathrm{s^{-1}\,cm^{-2}}$. Thus, the maximal optical depth is given by

$$\tau_{\gamma\gamma}^{max} \simeq 0.007\,R_{15}^{-1}\,\delta_1^{-3} \tag{5.31}$$

and the emission knot is optically thin for gamma-rays independent of their energy E_γ. Consequently, there is no relevant systematic influence on the temporal behavior of the emergent gamma-ray intensity.

5.4.2 Retardation effects of heavy neutrinos

Another possible effect on the time lags between gamma-rays and neutrinos results from a non-vanishing neutrino mass since the propagation speed becomes retarded, so that an additional delay between the photon and the neutrino observation occurs. Due to the large distance between the emission knot and the observer, the structure of the four dimensional space-time has to be considered. In case of an homogeneous and isotropic expansion of the Universe, Einstein's field equations yield the Robertson-Walker metric, so that a particle k with the rest mass m_k and the energy E_k has at a distance z the delay (Visser, 2004)

$$\Delta t \simeq \frac{15.42\,\mathrm{s}}{H_0/\frac{\mathrm{km}}{\mathrm{sMpc}}}\left(\frac{m_k c^2}{\mathrm{eV}}\right)^2\left(\frac{\mathrm{GeV}}{E_k}\right)^2 z\left[1 - \frac{3+q_0}{2}z + \frac{12 - j_0 + 8q_0 + 3q_0^2}{6}\,z^2 + \mathcal{O}(z^3)\right], \tag{5.32}$$

to a simultaneously produced massless particle. According to the analysis of 307 supernovae type Ia in the redshift range $0.015 \leq z \leq 1.62$ by Guimarães et al. (2009), the Hubble constant yields $H_0 = 72\,\mathrm{km\,s^{-1}\,Mpc^{-1}}$, the deceleration parameter $q_0 = -0.57$ and the jerk parameter $j_0 = -1$.

The pion decay generates different neutrino flavors with the mixing ratio $\nu_e : \nu_\mu : \nu_\tau = 1 : 2 : 0$, however, the ratio changes as a result of neutrino oscillation and one obtains $\nu_e : \nu_\mu : \nu_\tau = 1 : 1 : 1$ at a distance much larger than the oscillation length $L_{osc} = 4\pi\hbar c E\,\Delta m_{ij}^{-2}$. Consequently, the mean neutrino mass $\bar{m}_\nu = \sqrt{\frac{1}{3}m_{\nu_e}^2 + \frac{1}{3}m_{\nu_\mu}^2 + \frac{1}{3}m_{\nu_\tau}^2}$ has to be considered. To date there are only upper limits of the three neutrino masses, so that just an upper limit of the delay (5.32) can be calculated. The experimental observed upper limits (Altarelli & Winter, 2003) yield the mean neutrino mass $\bar{m}_\nu^{exp} = 10.5\,\mathrm{MeV}/c^2$, whereas theoretical considerations claim a maximal neutrino mass of $2.5\,\mathrm{eV}/c^2$ independent of the flavor (Fukugita & Yanagida, 2003). The

Fig. 5.6 shows that in case of the theoretical upper limit the delay is negligible even at large redshifts and small neutrino energies, but in case of the experimental upper limit the delay (5.32) can increase to several months or years. Thus, the mean neutrino mass is the crucial parameter and only an improved accuracy of the muon- and tau-neutrino mass can resolve whether the delay (5.32) is significant or not. Vice versa the observation of a delay between a correlated gamma and neutrino flare can be used to determine the mean neutrino mass.

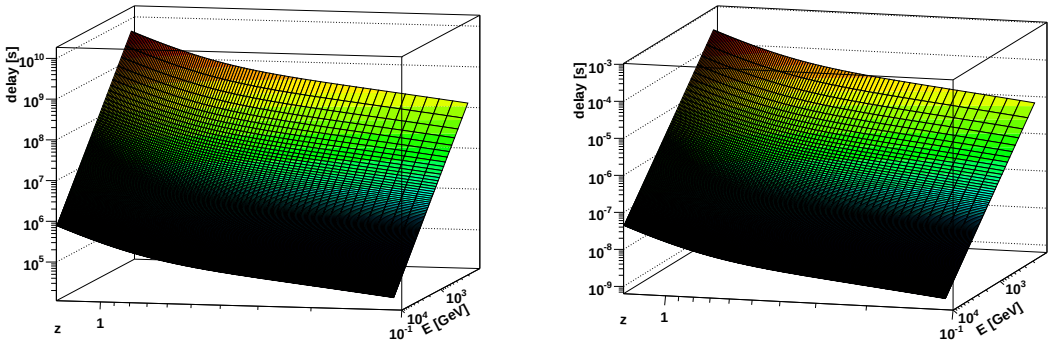

(a) $\bar{m}_\nu^{exp} = 10.5\,\mathrm{MeV}/c^2$ (b) $\bar{m}_\nu^{theo} = 2.5\,\mathrm{eV}/c^2$

Figure 5.6: Delay between simultaneously generated neutrinos and photons dependent of the redshift and the neutrino energy.

5.5 Conclusions to the high energy data of PKS 2155-304

Simultaneous to the low energy flare observations of PKS 2155-304 in July 29-30 2006 there was an extraordinary high γ-ray flare observed by H.E.S.S. and MAGIC (Aharonian et al., 2009). As stated in Sect. 4.6 the high energy flare at an energy $E_\gamma^* \geq 700\,\mathrm{GeV}$ starts simultaneously with the optical flare, but develops on considerably smaller timescales. According to Fig. 4.11 it has a distinct global maximum at ∼21:30 on the 29th of July, i. e. ~ 1 hour after the onset, which is probably simultaneous with the X-ray flux maximum. The rise and decay timescales are similar, so that the minimal flare duration of the main γ-ray flare yields $t_{d,obs}^*(E_\gamma^*) \geq 2\,\mathrm{h}$. The data show at least two other smaller-amplitude flares at later times, which are not going to be discussed here.
Since PKS 2155-304 is generally classified as an HBL the high energy emission is most likely explained by SSC scattering when a leptonic scenario is used. However, the high Compton dominance is more typical for a powerful FSRQ and in addition, the γ-ray flux decreases with the cube of the X-ray flux (when correlated) which is hard to explain by a one-zone SSC scenario. Hence, a more unconventional approach should be used in order to explain the observation.
Guided by the results of the lower energetic counterpart (see Sect. 4.6) a comparison of the temporal features of the observed γ-ray flare with the previously derived EC and pion production model is made in the following. Due to the strong correlation to the observations at lower energies (especially at X-ray energies) the γ-ray fit should also take the

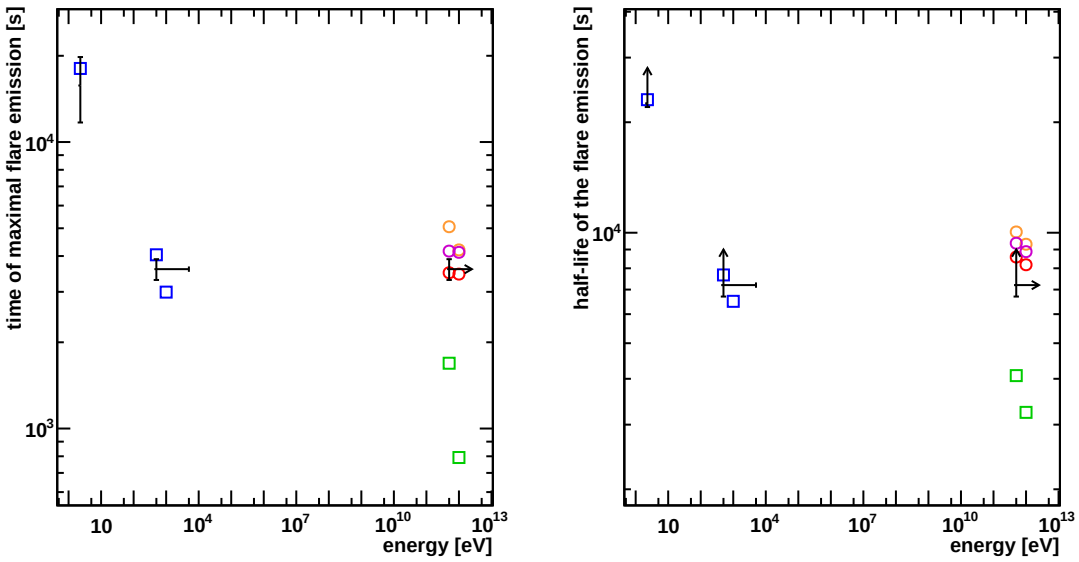

Figure 5.7: Best fit results of the temporal features of the optical, X-ray and γ-ray flare resulting from the theoretical model (colored markers) with the observations of PKS 2155-304 in July 2006 (black bars and arrows). Blue rectangles illustrate the temporal features of synchrotron radiation according to Eq. (4.51), green rectangles display the results of the EC model after Eq. (5.10) and the circles refer to γ-rays (red), muon-neutrinos (magenta) and electron-neutrinos (orange) generated by hadronic pion production according to Eq. (5.26). The parameters, that are not used in the default setting of full diffusion are in turn: $R_{15} = 1.58$, $b = 0.25$, $l_{EC} = 0.36$, $N_{10} = 8.9$ and $\theta_1 = 10$.

constraints (i)–(iii) of Sect. 4.6 into account.
Thus, the Fig. 5.7 displays the observed temporal features (black error bars and arrows) of PKS 2155-304 that accounts for a temporal inaccuracy of about 5 minutes due to the binning of the data. Based on the steep slope in the observed spectra at X-ray and TeV energies the flares at these ranges are expected to be generated at the low energy limits of observation. Using a trial-and-error method the figure also shows the best fit (colored markers) of the half-life, as well as the time of maximal emission of the γ-ray flare that results from the leptonic (green rectangles) and hadronic (red circles) scenario which are calculated with the Eq. (5.10) and (5.26) in the observer's frame, respectively, where $E^*_\gamma = 10\,\delta_1 E_\gamma$. The hadronic scenario yields about 10 minutes after the maximal gamma-ray emission its maximal muon-neutrino (magenta circles) emission and after further 10 minutes the electron-neutrino (orange circles) intensity is maximal. The flare durations behave in a similar manner.
In addition, the temporal features of the resulting synchrotron emission (blue rectangles) at optical and X-ray energies are fitted. Thereby, the match with the observations is even better than in Sect. 4.6 calculated, since the high density N_b of background particles yields an additional cooling of the electrons with $\gamma < \gamma_q$ that contribute to the optical

synchrotron emission.
In the case of the γ-ray flare the results of the hadronic scenario are in good agreement with the observations, whereas the EC scenario needs an extraordinary high accretion disk temperature $\theta_1 \gg 1$ corresponding to a low flux, that is in conflict with the Compton dominance of the observations. Based on Fig. 4.11 the maximal flux is $F_\gamma^* \simeq 10^{-8.6}\,\mathrm{erg\,cm^{-2}\,s^{-1}}$ at $E_\gamma^* = 0.3\,\mathrm{TeV}$ and $F_X^* \simeq 10^{-9.4}\,\mathrm{erg\,cm^{-2}\,s^{-1}}$ at $\epsilon_X^* = 0.3\,\mathrm{keV}$. In both cases the flux variation is considerably more than one, so that the ratio of this flux has also to be described by the theoretical model. Using a monochromatic approximation of the observed flux at the lowest observed X-ray and γ-ray energies, the ratio of the emergent intensities yields

$$I_{obs}(\epsilon_X^*)/I_{obs}(E_\gamma^*) = \frac{F_X^*\,E_\gamma^*}{F_\gamma^*\,\epsilon_X^*} \simeq 1.6 \cdot 10^8 \tag{5.33}$$

according to the observations. Since the expected X-ray flux maximum is one hour before the onset of the observations in this energy band, the ratio (5.33) is assumed to increase about a factor x with $1 < x < 3$. Calculating the intensities after Eq. (4.51) and (5.26) with the best fit parameters determines the ratio

$$I_{Sy}^{max}(\epsilon_X^*)/I_{pp}^{max}(E_\gamma^*) \simeq 3 \cdot 10^8\,, \tag{5.34}$$

which is in consideration of the inaccuracy x quite close to the observed ratio (5.33).
Summing up, the temporal features, as well as the variation ratios of the observed flare are at the low and high energy range well described by the theoretical model that takes relativistic electrons and protons simultaneously into account.

Chapter 6
Summary and conclusions

The theoretical examinations in this thesis have given several useful and verifiable predictions of the temporal development of flaring blazars from optical to γ-ray energies.
Starting with the pickup of electrons and protons from the intergalactic medium the emission knot gets enriched with relativistic particles, which subsequently generate non-thermal radiation at different wavelengths in their interactions with the environment. In general, there are multiple possible acceleration and emission scenarios in AGN, as discussed in Sect. 1.1.1 and 1.1.2. However, the used pickup model explains the generation of relativistic particles without much speculations about the unknown microphysical details of the streaming plasmas in the jet of an AGN and furthermore one can exclude several emission scenarios due to a reasonable confinement of the parameter space. Though, the observed particle energies above some PeV can hardly be explained by a simple pickup scenario without subsequent particle acceleration in the emission knot.
After investigation of the different influences of the relativistic particles, Sect. 3.1 yields the general solution of the particle transport equation

$$n_{e,p}(r,\gamma,t) = \sum_{k=1}^{\infty} b_k \, \frac{\sin(\lambda_k\, r)}{r} \; |\dot{\gamma}|^{-1} \int_{-\infty}^{t} \mathrm{d}t' \; \sum_i |\dot{\gamma}_i| \; q_1(\gamma_i, t') \, E_k^{e,p}(\gamma, \gamma_i) \,, \tag{6.1}$$

where spatial diffusion (with an energy dependent diffusion coefficient $D(\gamma)$), continuous energy losses with a loss rate $|\dot{\gamma}|$ and a separable source term $q_1(\gamma,\, t)\, q_2(r)$ are taken into account. Here, γ_i denotes the i'th zero of

$$f(\gamma') = t' - t + \int \mathrm{d}\gamma' \, \left|\dot{\gamma}'\right|^{-1} - \int \mathrm{d}\gamma \; |\dot{\gamma}|^{-1} \;, \tag{6.2}$$

which also occurs in the function

$$E_k^{e,p}(\gamma, \gamma_i) = \exp\left[-\lambda_k^2 \left(\int \mathrm{d}\gamma_i \, \frac{D(\gamma_i)}{|\dot{\gamma}_i|} - \int \mathrm{d}\gamma \, \frac{D(\gamma)}{|\dot{\gamma}|} \right)\right] . \tag{6.3}$$

In the full diffusion limit the eigenvalues are defined by $\lambda_k = k\,\pi/R$ and the spatial source coefficients yield

$$b_k = \frac{2}{R} \int_0^R \mathrm{d}r \; q_2(r)\, r \, \sin(\lambda_k r) \,. \tag{6.4}$$

This general formalism has in the following been specified based on the pickup scenario with no subsequent particle acceleration in order to draw quantitative conclusions.
Hence, the considered particles' Lorentz factors are limited by $\gamma < 7.3 \cdot 10^7 \, (\theta/1\,\mathrm{eV})^{-1}$, where θ denotes the photon energy of a thermal radiation field, so that photo-hadronic pion production, as well as high energy proton synchrotron radiation are negligible. Consequently, the favored hadronic emission scenario is pion production by inelastic p-p interactions. For the relativistic electrons the synchrotron and inverse Compton scattering losses, respectively (that scale with the magnetic field strength $B = 1\,b\,\mathrm{G}$ and the scattering parameter l_{EC} according to Eq. (3.41)), are dominant when $\gamma > 2481 \, (b^2 + l_{EC})^{-1/2} \, N_{10}^{1/2}$, whereas the constant excitation losses (which are proportional to the background particle density $N_b = 10^{10} \, N_{10} \, \mathrm{cm}^{-3}$) become significant in the opposite case. The nonlinear effects of initial SSC cooling are due to its mathematical complexity restrained in this thesis by using an injected particle density of $q_0 < 10^9 \, R_{15}^{-1} \, \gamma_0^{-2}$ or assuming a stronger external than internal photon energy density.
Hence, the continuous particle cooling yields for hadronic and leptonic emission scenarios a maximal flare duration, that is given by

$$\tau_{ul}^{p} = 2.0 \cdot 10^6 \, N_{10}^{-1} \, (1 + \ln(\gamma_6)/\ln(10^6)) \, \mathrm{s} \tag{6.5}$$

and

$$\tau_{ul}^{e} \simeq 4.9 \cdot 10^5 \, (b^2 + l_{EC})^{-1/2} \, N_{10}^{-1/2} \, \mathrm{s} \, , \tag{6.6}$$

respectively. Thus, the relativistic protons can generate significantly longer flare durations than the relativistic electrons, when the background particle density obeys $N_{10} < 16.7 \, (b^2 + l_{EC}) \, (1 + \ln(\gamma_6)/\ln(10^6))^2$.
In addition to continuous energy losses, the particle transport equation takes energy dependent spatial diffusion into account, but in the considered case of full diffusion ($R \gg \gamma_0^{\beta} \, l_{e,p}$) the diffusion coefficient has no impact on the relativistic particle distribution, as well as the resulting leptonic or hadronic flare emission.
In order to obtain more detailed information about the temporal flare development of AGN the Chap. 4 and 5 have examined the radiation that results from the interactions of the primary relativistic particles. However, the influence of secondary electrons that arise from hadronic interactions has been neglected, however, the timescale of its appearance can be well approximated by the temporal behavior of the corresponding electron neutrino intensity.
Low energy (i. e. from optical to X-ray energies) flares of AGN are described by synchrotron radiation that is generated by relativistic electrons. In a first crude approach analytical results of the emergent synchrotron intensity are obtained by using a monochromatic approximation of the synchrotron power spectrum, as well as an instantaneous and monoenergetic electron injection. Subsequently, the influence of the broadband nature of the synchrotron emission on the temporal flare development is investigated and at late times $t > t_0 + 2R/c$ and photon energies $\epsilon < \epsilon_b = 3.0 \, b^{-3} R_{15}^{-2}$ eV the emergent synchrotron intensity (4.28) can be approximated by a Gaussian time distribution (4.32). This reveals the half-life of the synchrotron flare, as well as the time of maximal emission. However, at earlier times or photon energies $\epsilon > \epsilon_b$, as well as in case of mathematical less convenient injection assumptions the emergent synchrotron intensity has to be calculated by a

numerical integration algorithm like Romberg's method or Gaussian quadrature. There is no a priori knowledge about the exact initial particle distribution, and hence a particle injection with a finite duration T, a power-law distributed energy and a spatially confinement on the outer shell of the emission knot, respectively, is considered with regard to its influence on the temporal flare development. In contrast to the broad synchrotron emission spectrum and the continuous synchrotron and EC cooling, respectively, of the relativistic electrons, the different initial particle assumptions have a negligible effect on the temporal flare behavior. Only a steep power law with a spectral index $\alpha < 0$ slightly shortens the temporal flare development at low synchrotron photon energies, as well as an injection duration $T \gg R/c$ extends the flare appropriate to T. Consequently, the theoretical examinations in the energy range $E_q^* < \epsilon^* < E_0^*$ of the observer's frame with $\delta = 10\,\delta_1$, where $E_q^* = 1.1\,(b^2 + l_{EC})^{-1}\,N_{10}\,\delta_1\,\mathrm{eV}$ and $E_0^* = 174\,b\gamma_6^2\,\delta_1\,\mathrm{keV}$ yield three remarkable general features about a synchrotron flare that are listed (in the observer's frame) in turn:

1. The flare starts at all photon energies when the injection of relativistic electrons into the knot begins.

2. At photon energies $\epsilon^* < \epsilon_b^*$ the synchrotron flare reaches its maximal intensity at

$$t_{max}^*(\epsilon^* < \epsilon_b^*) \simeq \left((3.3 \cdot 10^3\,R_{15} + 0.1\,(t_0 + T)/1\,\mathrm{s})\,\delta_1^{-1} + \frac{1.85 \cdot 10^4\,(\epsilon^*(\mathrm{eV}))^{-1/2}}{\delta_1^{1/2}(b^{3/2} + b^{-1/2} l_{EC})}\right)\ \mathrm{s} \tag{6.7}$$

   and the half-life of the flare is computed by

$$t_{1/2}^*(\epsilon^* < \epsilon_b^*) \simeq \left((3.3 \cdot 10^3\,R_{15} + 0.1\,T/1\,\mathrm{s})\,\delta_1^{-1} + \frac{3.74 \cdot 10^4\,(\epsilon^*(\mathrm{eV}))^{-1/2}}{\delta_1^{1/2}(b^{3/2} + b^{-1/2} l_{EC})}\right)\ \mathrm{s}\,. \tag{6.8}$$

3. At photon energies $\epsilon^* > \epsilon_b^*$ the synchrotron flare reaches its maximal intensity at

$$t_{max}^*(\epsilon^* > \epsilon_b^*) \simeq \left(0.1\,\delta_1^{-1}\,((t_0 + T)/1\,\mathrm{s}) + \frac{10\,(\epsilon^*/1\,\mathrm{keV}) + 1.83 \cdot 10^3}{\delta_1^{1/2}(b^{3/2} + b^{-1/2} l_{EC})\,(\epsilon^*(\mathrm{keV}))^{1/2}}\right)\ \mathrm{s} \tag{6.9}$$

   and the total flare duration yields

$$t_d^*(\epsilon^* > \epsilon_b^*) \simeq \left((6.7 \cdot 10^3\,R_{15} + 0.1\,T/1\,\mathrm{s})\,\delta_1^{-1} + \frac{1.0 \cdot 10^3\,(\epsilon^*(\mathrm{keV}))^{-1/2}}{\delta_1^{1/2}(b^{3/2} + b^{-1/2} l_{EC})}\right)\ \mathrm{s}\,. \tag{6.10}$$

Here $\epsilon_b^* = \delta\,\epsilon_b$ gives the upper limit of the photon energy in the observer's frame, for which the analytical approximation of the synchrotron flare is accurate. The last term in the Eq. (6.7)–(6.10) accounts for the EC and synchrotron losses by the parameters l_{EC} and b, respectively. The radius R_{15} of the emission knot and the duration T of the initial electron injection give a lower limit of the flare duration.
Summing up in few words, the synchrotron flare duration considerably extends over the

light travel time $2R/(c\delta)$ at optical photon energies and converges towards $2R/(c\delta)$ with increasing photon energy when the additive effect of the injection duration is negligible. The origin of the high energy flares is in contrast to low energy flares still under debate, so that two different possible scenarios were discussed here. Since SSC emission, as well as proton synchrotron radiation and photo-hadronic pion production could be reasonably excluded, the most favored scenarios were EC scattering and inelastic proton-proton interactions. The emergent intensities of both scenarios were calculated in turn by assuming an instantaneous and homogeneous injection into the whole plasmoid volume (3.32) of particles (i. e. electrons and protons) with a plateau distributed energy distribution (3.28) according to the influence of the expected electrostatic turbulence in the emission knot. The effect of other initial particle distributions on the high energy radiation was assumed to be similar to the case of synchrotron radiation and therefore not investigated again. Due to the mathematical complexity of the considered interactions the final results were only obtained by a numerical integration method (Gaussian quadrature), so that general statements about the high energy emission were hard to express. Especially, the amplitude of the emergent intensity depends on several unknown parameters of the AGN, whereas its temporal development is mainly defined by the particular cooling and emission process, as well as the size of the emission volume. In doing so, the high energy emission shows:

1. A temporal behavior that is similar to the case of synchrotron radiation is exposed, where the flare starts right after the particle injection and the flare duration, as well as the time of maximal emission increases with decreasing photon (or neutrino) energy or decreasing cooling parameter (l_{EC} and N_b, respectively).

2. According to the corresponding particle cooling the temporal features also exhibit distinct differences between the leptonic and hadronic emission scenarios as illustrated in Fig. 5.4. So, in contrast to the leptonic emission behavior the time of maximal emission of gammas and neutrinos by hadronic pion production only slightly differs by changing the cooling parameter N_b or the energy E_j of the considered particle.

3. Another important temporal feature is the intrinsic time lag between the neutrino and the gamma-ray emission by p-p interactions as depicted in Fig. 5.5. In particular the half-life of the neutrino emission at low energies (of some TeV) is considerably delayed with reference to the corresponding gamma-ray flare and the corresponding time lag is determined by

$$\Delta t^*_{1/2}(E^*_j) = 3.9\, N_{10}^{-1} \left(E^*_j / 1\,\mathrm{TeV}\right)^{-0.55} \mathrm{hr}\,. \tag{6.11}$$

Thus, in the observer's frame with $\delta_1 = 1$ the neutrino flare at $E^*_\nu = 1\,\mathrm{TeV}$ is expected to last about ∼4 hr longer than the γ-ray flare at $E^*_\gamma = 1\,\mathrm{TeV}$, and also its maximal intensity is delayed for several minutes (at most ∼0.3 hr). In doing so, a standard emission knot volume around $R_{15} \simeq 1$ and a minimal background particle density of $N_{10} = 1$ is used in order to obtain a detectable neutrino flux with IceCube from a source at 1 Mpc distance and optimal declination condition. Further systematic retardation effects on the gamma-rays and neutrinos could be excluded at the considered parameter space and a mean neutrino mass beyond the upper limit of theoretical calculations.

In addition, the theoretical results were finally used to explain the flaring of PKS 2155-304 on 2006 July 29-30. For this purpose, the temporal features (time of maximal flux, flare duration) of the observed optical, X-ray and γ-ray flares were exposed and subsequently compared with the theoretical predictions. Thus, the Eq. (6.7)–(6.10) yield an accurate fit with the observations in the optical and X-ray band for a quite narrow range of parameters. However, the inclusion of the γ-ray data required a higher background particle density $N_{10} > 1$, so that the optical synchrotron photons were in addition cooled by excitation losses which finally led to an even better agreement with the observations. Consequently, the whole observations are accurately described using relativistic electrons and protons simultaneously, so that the synchrotron radiation of the electrons generate the flaring in the optical and X-ray band and the protons produce the γ-ray flare through inelastic collisions with the protons of the background plasma.
Summing up, the thesis exposes several verifiable predictions of the flaring behavior of blazars from optical to γ-ray energies with reference to the primary particle nature and its radiation mechanism, respectively.
According to the small amount of a priori knowledge about this class of astrophysical objects, some of the basic assumptions in this thesis are still under debate, like the assumed pickup model, the constant cooling parameters, as well as the simple diffusion model and the range of the parameters of an AGN jet in general. Another remaining question is the influence of significant particle acceleration within the emission region and during the flare development. However, the effect of a continuous energy gain according to $\dot{\gamma} = \gamma/t_{acc}$ can easily be applied to the general formalism (6.1) of the relativistic particle density when the effects of momentum diffusion are still negligible. Thus, there surely remains room for improvements: On the one hand, the theoretical calculations could be extended by (i) significant particle acceleration, (ii) nonlinear cooling effects, (iii) the consideration of SSC radiation and (iv) complexer diffusion models. On the other hand, the theoretical predictions have to be tested more sophisticatedly (by using also the spectral features) on the increasing number of multiwavelength observations of blazars.
However, most of these approaches require the room of another thesis and as the very beginning has already exhibited the epistemological confinement of a physical explanation, the presented analysis has also shown that a useful explanation is only obtained by a physical confinement. An important step towards the possible mechanisms of these most giant cosmic accelerators is made and most certainly more will follow.

Appendix A
Invariance relations

Throughout the thesis the calculations are in some places switched from the rest frame of the emission knot to the rest frame of the observer. For this purpose, a Doppler transformation with a Doppler factor $\delta = [\Gamma(1-\beta\,\cos\alpha)]^{-1}$ is adopted, where the emission knot has a bulk velocity βc, the corresponding Lorentz factor Γ and moves with an angle α to the line of sight. The transformation formulas regarding photon intensities result from the Lorentz invariance of the photon phase space density (Begelman et al., 1984)

$$\mathcal{P} = \frac{dN}{d\mathcal{V}} = \mathcal{P}^* \,. \tag{A.1}$$

With the photon energy-momentum relation $\epsilon = p\,c$ and spherical momentum coordinates (i.e. $d^3p = p^2\,dp\,d\Omega$) the invariance relation (A.1) can be expressed by

$$\mathcal{P} = \frac{c^3\,dN}{\epsilon^2\,d\epsilon\,d\Omega\,d^3x} \,. \tag{A.2}$$

For the differential photon density $M(r,\epsilon,t) = \frac{dN}{d\Omega\,d^3x}$ this gives the invariant

$$\frac{M}{\epsilon^2\,d\epsilon} = \frac{M^*}{\epsilon^{*2}\,d\epsilon^*} \,, \tag{A.3}$$

so that the intensity $I = c\,M$ relation yields

$$I^*(R,\epsilon^*,\,t^*) = \delta^3\,I(R,\epsilon = \frac{\epsilon^*}{\delta},\,t = t^*\,\delta). \tag{A.4}$$

Times and photon energies transform as $t^* = \delta^{-1}\,t$ and $\epsilon^* = \delta\,\epsilon$, respectively.

Appendix B
Additional calculations to the primary particle distribution

B.1 Solution of the three dimensional spatial diffusion equation

Here a more rigorous derivation is presented of how to proceed from the general transport equation

$$\frac{\partial n_a(\mathbf{r},\gamma,t)}{\partial t} = \Delta\, D(\gamma)\, n_a(\mathbf{r},\gamma,t) + \frac{\partial}{\partial \gamma}\left[|\dot{\gamma}| n_a(\mathbf{r},\gamma,t)\right] + q_1(\gamma,t) q_2(\mathbf{r})\,. \tag{B.1}$$

to obtain a differential number density of relativistic particles $n_a(\mathbf{r},\gamma,t)$ at every point $\mathbf{r} = r(\sqrt{1-\mu^2}\cos\phi, \sqrt{1-\mu^2}\sin\phi, \mu)$ within the source where r, ϕ and $\mu = \cos\theta$ are the spherical coordinates. Using the ansatz of separation

$$n_a(r,\mu,\phi,\gamma,t) = F(r)\, G(\mu,\phi)\, n(\gamma,t) \tag{B.2}$$

the spatial diffusion operator of the particle kinetic transport Eq. (B.1) is of Sturm-Liouville type and its eigenfunction form an orthonormal base in position space. The eigenfunctions are defined by

$$\Delta(F(r)\, Y(\mu,\phi)) + \lambda^2\, F(r)\, Y(\mu,\phi) = 0, \tag{B.3}$$

with the boundary conditions $F(0) < \infty$ and $F(R) = 0$, as well as $Y(\phi + 2\pi) = Y(\phi)$ and $Y(\mu)$ is regular at $\mu = 1, -1$. Consequently, the eigenfunction Eq. (B.3) is separated into the angular dependent equation

$$\frac{\partial^2 Y}{\partial Y^2} + (1-\mu^2)\frac{\partial}{\partial \mu}\left((1-\mu^2)\frac{\partial Y}{\partial \mu}\right) + S(1-\mu^2)\, Y = 0 \tag{B.4}$$

and the radial dependent equation

$$\frac{\partial}{\partial r}\left(r^2 \frac{\partial F}{\partial r}\right) + \left(\lambda^2 r^2 - S\right)\, F = 0 \tag{B.5}$$

Table B.1: First ten Zeros $y_{l,k}$ of the spherical Bessel functions j_l.

l	$y_{l,1}$	$y_{l,2}$	$y_{l,3}$	$y_{l,4}$	$y_{l,5}$	$y_{l,6}$	$y_{l,7}$	$y_{l,8}$	$y_{l,9}$	$y_{l,10}$
0	3.14	6.28	9.42	12.57	15.71	18.85	22.00	25.13	28.27	31.42
1	4.49	7.73	10.90	14.07	17.22	20.37	23.52	26.67	29.81	32.96
2	5.76	9.10	12.32	15.51	18.69	21.85	25.01	28.17	31.32	34.47
3	6.99	10.42	13.70	16.92	20.12	23.30	26.48	29.64	32.80	35.96
4	8.18	11.70	15.04	18.30	21.53	24.72	27.92	31.09	34.27	37.43

where S is the constant of separation.
The well-known differential equation (B.4) is solved by the Laplace's spherical harmonics

$$Y_{l,m}(\mu,\phi) = N_{l,m}\, P_l^m(\mu)\, e^{im\phi}\,, \tag{B.6}$$

with the associated Legendre polynomials $P_l^m(\mu)$ and the normalization constant $N_{l,m}$. Using the boundary conditions for $Y_{l,m}(\mu,\phi)$ the constant of separation yields $S = l(l+1)$ for the non-negative integer $l \geq |m|$.
Accordingly, $x = \lambda r$ is substituted in the radial equation (B.5) and the differential equation yields

$$x^2 \frac{\partial^2 F}{\partial x^2} + 2x\,\frac{\partial F}{\partial x} + (x^2 - l(l+1))\,F = 0, \tag{B.7}$$

which is solved by the spherical Bessel functions $j_l(\lambda r)$ and $y_l(\lambda r)$. But only the functions j_l are finite at the center and using the second boundary condition ($j_l(\lambda_{l,k}R) = 0$) one obtains the eigenvalues $\lambda_{l,k} = y_{l,k}/R$, where $y_{l,k}$ is the k-th zero of j_l.
Due to the two partial differential equations (B.4) and (B.5) the particle density and the spatial source term is of the form

$$n_a(r,\mu,\phi,\gamma,t) = \sum_{l=0}^{\infty}\sum_{k=1}^{\infty}\sum_{m=-l}^{l} n_{l,k,m}(\gamma,t)\, Y_{l,m}(\mu,\phi)\, j_l(\lambda_{l,k}r)\,, \tag{B.8}$$

and

$$q_2(r,\mu,\phi) = \sum_{l=0}^{\infty}\sum_{k=1}^{\infty}\sum_{m=-l}^{l} b_{l,k,m}\, Y_{l,m}(\mu,\phi)\, j_l(\lambda_{l,k}r)\,. \tag{B.9}$$

Using the orthonormality relation of spherical Bessel functions

$$\int_0^R dr\; r^2\, j_l(\lambda_{l,k}r)\, j_l(\lambda_{l,k'}r) = \frac{R^3}{2}[j_{l+1}(\lambda_{l,k}R)]^2\,\delta_{k,k'}\,, \tag{B.10}$$

the coefficients $b_{l,k,m}$ are determined by

$$b_{l,k,m} = \frac{2}{R^3\,[j_{l+1}(\lambda_{l,k}R)]^2}\int_0^{2\pi} d\phi \int_{-1}^{1} d\mu \int_0^R dr\, r^2 q_2(r,\phi,\mu) Y_{l,m}(\mu,\phi)\, j_l(\lambda_{l,k}r)\,. \tag{B.11}$$

Inserting the expansions (B.8) and (B.9) into the transport equation (B.1) yields for the particle expansion functions $n_{l,k,m}(\gamma,t)$ the equation

$$\sum_{l=0}^{\infty}\sum_{k=1}^{\infty}\sum_{m=-l}^{l} Y_{l,m}\, j_l(\lambda_{l,k} r)\Big[\frac{\partial n_{l,k,m}(\gamma,t)}{\partial t} - \frac{\partial}{\partial\gamma}\left[|\dot{\gamma}| n_{l,k,m}(\gamma,t)\right] + D(\gamma)\lambda_{l,k}^2 n_{l,k,m}(\gamma,t) - b_{l,k,m} q_1(\gamma,t)\Big] = 0\,. \tag{B.12}$$

In order to generate an isotropic production rate of non-thermal emission, an isotropic density of relativistic particles is needed, so that the three dimensional spatial dependence (B.8) reduces to its radial component and the expansion coefficients with $l = 0$ have a dominating influence, respectively. At radii $r \ll R$ the spherical Bessel function can be approximated by

$$j_l(\lambda_{l,k} r \ll 1) \simeq 2^l\,(\lambda_{l,k} r)^l\,\frac{l!}{(2l+1)!} \tag{B.13}$$

and hence the first eigenfunction (with $l = 0$) is dominant at the inner part of the emission volume. Furthermore, the spherical harmonics $Y_{l,m}$ are apart from $Y_{0,0}$ oscillating functions with positive and negative values. Additionally, the differential equation of the particle expansion functions $n_{l,k,m}(\gamma,t)$ corresponds to Eq. (3.14), which yields according to Eq. (3.26) an exponentially decreasing behavior of $n_{l,k,m}(\gamma,t)$ with increasing eigenvalue $\lambda_{l,k}$. Since $y_{0,k}$ is the smallest zero (see Tab. (B.1)) the full solution is accurately approximated by its isotropic part when the argument of the exponential function (3.26) is less than -1. Thus, the spatial diffusion assumption, as well as the continuous energy loss process have to be specified in order to obtain a more quantitative result.
For example in the case of relativistic electrons that suffer continuous synchrotron losses, i. e. $|\dot{\gamma}| = D_s\,\gamma^2$ and have a constant diffusion coefficient D_0, the expansion function is given by

$$n_{l,k,m}(\gamma,t) = b_{l,k,m}\int_{-\infty}^{t} \mathrm{d}t'\,\frac{e^{-D_0\lambda_{l,k}^2(t-t')}}{(1-D_s\gamma(t-t'))^2}\,q_1\left(\gamma' = \frac{\gamma}{1-D_s\gamma(t-t')},\, t'\right)\,. \tag{B.14}$$

Consequently, at a time

$$t - t' \geq \frac{R^2}{D_0\, y_{l,k}^2} \tag{B.15}$$

the relativistic electron distribution $n_e(r,\mu,\phi,\gamma,t)$ is spatially isotropized.
Neglecting the eigenfunctions with $l \geq 1$ the angular dependence disappears and the differential number density of relativistic particles turns from Eq. (B.8) to (3.11). However, using the one dimensional idealization of the diffusion problem, one has to take into account that a possible anisotropic initial particle distribution only vanishes with increasing time due to the influence of spatial diffusion.

B.2 Final approach to solve the transport equation

In order to obtain the expansion coefficients of the relativistic particle density (3.11) the differential Eq. (3.20) has to be solved. For this purpose a Laplace transformation in t

and x domain is adopted. The latter yields the function

$$F_k^{e,p}(s,t) = \mathcal{L}\left\{G_k^{e,p}(x,t)\right\} = \int_0^\infty \mathrm{d}x\, G_k^{e,p}(x,t) e^{-x\,s} \tag{B.16}$$

in the Laplace space where the differential $\partial G_k^{e,p}(x,t)/\partial x$ is determined by

$$\int_0^\infty \mathrm{d}x\, \frac{\partial G_k^{e,p}}{\partial x} e^{-x\,s} = s\, F_k^{e,p}(s,t) - G_k^{e,p}(x=0,t)\,. \tag{B.17}$$

Since the Green's function has to vanish in the limits of its arguments x and t, one obtains $G_k^{e,p}(x=0,t) = 0$, so that the differential Eq. (3.20) can be written as

$$\frac{\partial F_k^{e,p}}{\partial t} + s\, F_k^{e,p} = \delta(t-t') e^{-x'\,s}. \tag{B.18}$$

A further Laplace transformation of $F_k^{e,p}(s,t)$ defines

$$C_k^{e,p}(s,T) = \mathcal{L}\left\{F_k^{e,p}(s,t)\right\} = \int_0^\infty \mathrm{d}x\, F_k^{e,p}(s,t) e^{-t\,T} \tag{B.19}$$

and thus

$$\int_0^\infty \mathrm{d}t\, \frac{\partial F_k^{e,p}}{\partial t} e^{-t\,T} = T\, C_k^{e,p}(s,T) - F_k^{e,p}(s,t=0)\,. \tag{B.20}$$

Once again, the last term vanishes due to the general condition $G_k^{e,p}(x,t=0) = F_k^{e,p}(s,t=0) = 0$ and the differential Eq. (B.18) yields

$$T\, C_k^{e,p}(s,T) + s\, C_k^{e,p}(s,T) = \int_0^\infty \mathrm{d}t\, \delta(t-t') e^{-x'\,s} e^{-t\,T}\,, \tag{B.21}$$

which can be merged to

$$C_k^{e,p}(s,T) = \frac{1}{s+T} e^{-x'\,s} e^{-t'\,T}\,. \tag{B.22}$$

Converting this term back into the t domain results in

$$F_k^{e,p}(s,t) = \mathcal{L}^{-1}\left\{C_k^{e,p}(s,T)\right\} = H(t-t') e^{-s\,(x'+t-t')}\,, \tag{B.23}$$

with the Heaviside step function $H(t-t')$ and another transformation into the x domain yields

$$G_k^{e,p}(x,t) = \mathcal{L}^{-1}\left\{F_k^{e,p}(s,t)\right\} = H(t-t')\,\delta\left(x-(x'+t-t')\right)\,. \tag{B.24}$$

Appendix C
Additional calculations to the emergent synchrotron intensity

C.1 Partial Integration of Eq. (4.23)

In order to simplify to integral expression

$$K = \int_0^R dr' \, \sin(\lambda_k \, r') \, J(r') \,, \tag{C.1}$$

the term is partially integrated, i. e.

$$K = -\frac{\cos(\lambda_k \, R)}{\lambda_k} \, J(r' = R) + \int_0^R dr' \, \frac{\cos(\lambda_k \, r')}{\lambda_k} \, \frac{\partial J}{\partial r'}, \tag{C.2}$$

as $J(r' = 0) = 0$. Using Eq. (4.24) and its differential

$$\begin{aligned} \frac{\partial J}{\partial r'} =& H \left[c\tau - r' \right] \, \frac{\left(1 + D_s \gamma_0 (\tau - \frac{r'}{c}) \right)^{\frac{2}{3}}}{R + r'} \\ & \times \exp \left(-A \, r'^2 + B_k(\tau) \, r' \right) \\ & + H \left[c\tau + r' \right] \, \frac{\left(1 + D_s \gamma_0 (\tau + \frac{r'}{c}) \right)^{\frac{2}{3}}}{R - r'} \\ & \times \exp \left(-A \, r'^2 - B_k(\tau) \, r' \right) , \end{aligned} \tag{C.3}$$

one obtains

$$\begin{aligned} K = \frac{1}{\lambda_k}\Bigg(& \int_0^R dr' \, \cos(\lambda_k r') \, H\left[c\tau - r'\right] \\ & \times \frac{\left(1 + D_s\gamma_0(\tau - \frac{r'}{c})\right)^{\frac{2}{3}}}{R + r'} \exp\left(-A\, r'^2 + B_k(\tau)\, r'\right) \\ & + \int_0^R dr' \, \cos(\lambda_k r') \, H\left[c\tau + r'\right] \\ & \times \frac{\left(1 + D_s\gamma_0(\tau + \frac{r'}{c})\right)^{\frac{2}{3}}}{R - r'} \exp\left(-A\, r'^2 - B_k(\tau)\, r'\right)\Bigg) \\ & - \frac{\cos(\lambda_k R)}{\lambda_k} \int_{-R}^R dy \, H\left[c\tau - y\right] \\ & \times \frac{\left(1 + D_s\gamma_0(\tau - \frac{y}{c})\right)^{\frac{2}{3}}}{R + y} \exp\left(-A\, r'^2 + B_k(\tau)\, r'\right) \end{aligned} \tag{C.4}$$

After substituting r' to $-r'$ in the second integral, the first two integrals can be merged, as the cosine is an even function. In the third integral the variable of integration y is replaced by r', which finally yields

$$\begin{aligned} K = & \frac{1}{\lambda_k} \int_{-R}^R dr' \, \left(\cos(\lambda_k r') - \cos(\lambda_k R)\right) H\left[c\tau - r'\right] \\ & \times \frac{\left(1 + D_s\gamma_0(\tau - \frac{r'}{c})\right)^{\frac{2}{3}}}{R + r'} \exp\left(-A\, r'^2 + B_k(\tau)\, r'\right). \end{aligned} \tag{C.5}$$

C.2 Approximate Eq. (4.29) by method of steepest descent

Due to Eq. (4.29) the temporal development of the emergent synchrotron intensity can be approximated by

$$I(\epsilon, z > z_0) \simeq I_0(\epsilon) \exp(-f(\epsilon, z)), \tag{C.6}$$

with

$$f(\epsilon, z) = \frac{\epsilon}{E_0} z^2 - \frac{2}{3} \ln z \,. \tag{C.7}$$

The first and second derivation of $f(\epsilon, z)$ yield

$$\begin{aligned} \frac{\partial f}{\partial z} &= \frac{2\epsilon}{E_0} z - \frac{2}{3} z^{-1}, \\ \frac{\partial^2 f}{\partial z^2} &= \frac{2\epsilon}{E_0} + \frac{2}{3} z^{-2}. \end{aligned}$$

In the following, the function $f(\epsilon, z)$ is developed at its maximum $z_{max} = \sqrt{E_0/(3\epsilon)}$ by a Taylor series, so that

$$f(\epsilon, z) \simeq \frac{1}{3}\left(1 - \ln\left(\frac{E_0}{3\epsilon}\right)\right) + \frac{2\epsilon}{E_0}\left(z - \sqrt{\frac{E_0}{3\epsilon}}\right)^2 \tag{C.8}$$

and the emergent synchrotron intensity becomes

$$I(\epsilon, z > z_0) \simeq I_0(\epsilon) \left(\frac{E_0}{3\epsilon}\right)^{\frac{1}{3}} e^{-\frac{1}{3}} \exp\left(-\frac{2\epsilon}{E_0}\left(z - \sqrt{\frac{E_0}{3\epsilon}}\right)^2\right) . \tag{C.9}$$

Appendix D
General split of a two dimensional integral by Heaviside functions

In order to calculate the two dimensional spatial integral expressions of the emergent intensity (4.51), (5.10) and (5.26), respectively, the limitation of the integrals by the Heaviside functions have to be taken into account. This yields a multiple of integrals, since the integration limits of the inner integral depend on the outer integral. Hence, the general Heaviside functions $H[A-s]$ and $H[s-B]$ are considered, so that multiple simple calculations yield

$$
\begin{aligned}
&\int_0^R dr' \int_{R-r'}^{R+r'} ds\, H[A-s]\, H[s-B] \\
&\quad = H[A]\Bigg(H[A-2R]\, H[2R-B]\Big[H[R-B]\Big(H[-B] \int_0^R dr' \int_{R-r'}^{R+r'} ds \\
&\qquad\qquad + H[B]\Big(\int_0^{R-B} dr' \int_{R-r'}^{R+r'} ds + \int_{R-B}^{R} dr' \int_{B}^{R+r'} ds \Big) \Big) \\
&\qquad + H[B-R]\, H[B] \int_{B-R}^{R} dr' \int_{B}^{R+r'} ds \Big] \\
&\quad + H[A-R]\, H[2R-A]\, H[A-B]\Big[H[R-B]\Big(H[2R-A-B] \int_0^{A-R} dr' \int_{R-r'}^{R+r'} ds \\
&\qquad\qquad + H[A+B-2R]\Big(\int_0^{R-B} dr' \int_{R-r'}^{R+r'} ds + \int_{R-B}^{A-R} dr' \int_{B}^{R+r'} ds \Big) \Big) \\
&\qquad + H[B-R]\, H[A+B-2R] \int_{B-R}^{A-R} dr' \int_{B}^{R+r'} ds \\
&\qquad + H[2R-A-B]\Big(H[-B] \int_{A-R}^{R} dr' \int_{R-r'}^{A} ds \\
&\qquad\qquad + H[B]\Big(\int_{A-R}^{R-B} dr' \int_{R-r'}^{A} ds + \int_{R-B}^{R} dr' \int_{B}^{A} ds \Big) \Big) \\
&\qquad + H[A+B-2R]\, H[B] \int_{A-R}^{R} dr' \int_{B}^{A} ds \Big]
\end{aligned}
$$

$$+ H[R-A]H[A-B]\Big[H[-B]\int_{R-A}^{R} dr' \int_{R-r'}^{A} ds + H[B]\Big(\int_{R-A}^{R-B} dr' \int_{R-r'}^{A} ds + \int_{R-B}^{R} dr' \int_{B}^{A} ds\Big)\Big]\Big) . \tag{D.1}$$

After specifying the parameters A and B the emergent intensities can be calculated by a numerical algorithm of integration.

Appendix E
Numerical integration methods

In general, a numerical integration method (or quadrature rule) gives an approximation of a definite integral of a function $f(x)$ by constructing an interpolation of $f(x)$ within the domain of integration $[a, b]$, that is more easy to integrate. Usually one uses polynomials as interpolation function and in order to increase the precision of the evaluation the interval of integration is split into multiple sub-intervals, where the approximation is calculated and summed up with the results of the other sub-intervals afterwards. Obviously the accuracy of the numerical integration depends very much on the abscissas at which $f(x)$ is evaluated. In general, one differentiate between methods with equally spaced and unequally spaced abscissas, where the first are generally called the Newton-Cotes quadrature rules and the latter mostly refer to Gaussian quadrature. Below, are the basic concepts of the used quadratures investigated, but in order to obtain a detailed insight into the numerical algorithm of integration the reader is referred to Press et al. (2007).

E.1 Romberg's method

The Romberg's method estimates the definite integral by applying a Richardson extrapolation repeatedly on a Newton-Cotes quadrature rule, like the trapezium or the midpoint rule. In order to avoid the evaluation at the endpoints of the interval the midpoint rule is used, where N equal sub-intervals of length $h = (b - a)/N$ are considered, so that

$$\int_a^b \mathrm{d}x\, f(x) \simeq h \sum_{i=0}^{N-1} f(x_i)\,, \tag{E.1}$$

with $x_i = a + (i + 0.5)\, h$. Romberg's method is subsequently adopted to increase the accuracy of the quadrature. Here the length of the sub-intervals develops by the sequence $h_n = (b - a)/2^n$ and the quadrature uses an iterative calculation according to

$$R(n, m) = \frac{1}{4^m - 1}(4^m\, R(n, m - 1) - R(n - 1, m - 1))\,, \tag{E.2}$$

where the zeroth extrapolation $R(n, 0)$ equals the result of the midpoint rule when $N = 2^n$. The iteration formula leads to an exact calculation of the integral by $R(n, m)$ in case of

$n, m \to \infty$. Thus, a great advance of the iterative method is the regulation of the error of the extrapolation, which is set to 10^{-6} in this thesis.

E.2 Gaussian quadrature

The Gaussian quadrature uses that the optimal abscissas are the roots x_i of the orthogonal polynomials of degree N which have to be a capable approximation of the function in the considered interval $[a, b]$. Thus, the integrand can generally be expressed by $f(x) = W(x)\, g(x)$, where $W(x)$ denotes a known weight function and $g(x)$ is approximately polynomial, so that

$$\int_a^b \mathrm{d}x\, f(x) = \int_a^b \mathrm{d}x\, W(x)\, g(x) \simeq \frac{b-a}{2} \sum_{i=1}^{N} w_i\, g\left(\frac{1}{2}(b-a)x_i + \frac{1}{2}(b+a)\right) , \tag{E.3}$$

with the weights w_i. This approximation is exact if $g(x)$ is a polynomial of degree $2N-1$ or less.
Here the simplest case of a weight function $W(x) = 1$ is considered and hence the associated polynomials are the Legendre polynomials $P_N(x)$, where the weights are given by (Abramowitz & Stegun, 1984)

$$w_i = \frac{2}{(1-x_i^2)[P_N'(x_i)]^2} . \tag{E.4}$$

Appendix F
The optical depth by photon-photon pair attenuation

Here the effect of pair attenuation on the target photons of the EC process, as well as the generated synchrotron photons is examined in order to obtain a significant rate of TeV photons. According to Dermer and Schlickeiser (1993b) the photon density n_{ad} in the comoving frame of the emission knot at a dimensionless energy $\tilde{\epsilon} = \epsilon/(m_e c^2)$ and a distance $\sqrt{z^2 + R^2}$ from the accretion disk with the total luminosity $L_{ad} = 10^{46} L_{46}\,\mathrm{erg\,s^{-1}}$ yields

$$n_{ad}(\tilde{\epsilon}, z) \simeq \frac{15}{4\pi^5\,\theta^4}\,\frac{\tau_{sc}\,L_{ad}}{m_e c^3 (z^2+R^2)}\,\frac{\tilde{\epsilon}^2}{\exp(\tilde{\epsilon}/\theta)-1}\,, \tag{F.1}$$

where the spectral luminosity is Planckian distributed with the dimensionless accretion disk temperature θ (in units of $m_e c^2$). Using the accretion disk photons the pair attenuation optical depth is calculated by

$$\tau_{\gamma\gamma}(\tilde{\epsilon}_1) = \int_{z_i}^{\infty} dz \int_{2/\tilde{\epsilon}_1}^{\infty} d\tilde{\epsilon}\,\sigma_{\gamma\gamma}(\tilde{\epsilon_1}, \tilde{\epsilon}) n_{ad}(\tilde{\epsilon}, z)\,, \tag{F.2}$$

for a photon with dimensionless energy $\tilde{\epsilon}_1 = \epsilon_1/(m_e c^2)$, that is radially emitted at a distance z_i. A convenient approximation of the cross-section $\sigma_{\gamma\gamma}$ is given by (Zdziarski & Lightman, 1985)

$$\sigma_{\gamma\gamma}(\tilde{\epsilon}_1, \tilde{\epsilon}) = \frac{\sigma_T}{3}\,\tilde{\epsilon}\,\delta\left(\tilde{\epsilon} - \frac{2}{\tilde{\epsilon}_1}\right)\,. \tag{F.3}$$

Inserting Eq. (F.1), as well as Eq. (F.3) the optical depth becomes

$$\tau_{\gamma\gamma}(\tilde{\epsilon}_1) = \frac{10}{\pi^5}\,\frac{\tau_{sc}\,L_{ad}\sigma_T\,(\pi/2 - \arctan(z_i/R))}{\theta^4\,m_e c^3\,R}\,F_1(\tilde{\epsilon}_1)\,, \tag{F.4}$$

with

$$F_1(\tilde{\epsilon}_1) = \tilde{\epsilon}_1^{-3}\left(\exp\left(\frac{2}{\tilde{\epsilon}_1\theta}\right) - 1\right)^{-1}\,. \tag{F.5}$$

The function $F_1(\tilde{\epsilon}_1)$ reaches its maximum $F_{1,max} = 0.178\,\theta^3$ at $\tilde{\epsilon}_{1,max} = 0.709\,\theta^{-1}$ (Dermer & Schlickeiser, 1993b) and at the distance $z_i \gg R$ the arc tangent function is approximated by $\arctan(z_i/R) \simeq \pi/2 - R/z_i$, so that the maximal optical depth yields

$$\tau_{\gamma\gamma,\,max} = 5.1 \cdot 10^{-2}\,\frac{\tau_{-2}\,L_{46}\,\theta_{-4}^{-1}}{z_i/1\,\mathrm{pc}}\,, \tag{F.6}$$

when the temperature $\theta = 10^{-4}\theta_{-4}$.
In case of energies $\tilde{\epsilon}_1 \gg \tilde{\epsilon}_{1,max}$ one obtains $F_1(\tilde{\epsilon}_1 \gg \tilde{\epsilon}_{1,max}) \simeq 0.5\,\theta\,\tilde{\epsilon}_1^{-2}$ and thus

$$\tau_{\gamma\gamma}(\tilde{\epsilon}_1 \gg \tilde{\epsilon}_{1,max}) = \tau_{\gamma\gamma,max}\frac{F_1(\tilde{\epsilon}_1 \gg \tilde{\epsilon}_{1,max})}{F_{1,max}} \simeq 0.28\,\frac{\tau_{-2}\,L_{46}\,\theta_{-4}^{-1}}{z_i/1\,\mathrm{pc}}\left(\frac{\tilde{\epsilon}_{1,max}}{\tilde{\epsilon}_1}\right)^2\,. \tag{F.7}$$

However, at energies $\tilde{\epsilon}_1 \ll \tilde{\epsilon}_{1,max}$ with $F_1(\tilde{\epsilon}_1 \ll \tilde{\epsilon}_{1,max}) \simeq \tilde{\epsilon}_1^{-3}\,\exp(-2.8\,\tilde{\epsilon}_{1,max}/\tilde{\epsilon}_1)$ the optical depth becomes

$$\begin{aligned}\tau_{\gamma\gamma}(\tilde{\epsilon}_1 \ll \tilde{\epsilon}_{1,max}) &= \tau_{\gamma\gamma,max}\frac{F_1(\tilde{\epsilon}_1 \ll \tilde{\epsilon}_{1,max})}{F_{1,max}} \\ &\simeq 0.80\,\frac{\tau_{-2}\,L_{46}\,\theta_{-4}^{-1}}{z_i/1\,\mathrm{pc}}\left(\frac{\tilde{\epsilon}_{1,max}}{\tilde{\epsilon}_1}\right)^3\,\exp\left(-2.8\frac{\tilde{\epsilon}_{1,max}}{\tilde{\epsilon}_1}\right).\end{aligned} \tag{F.8}$$

An observed gamma-ray energy $\epsilon_1^* = 1\,\mathrm{TeV}$ results in $\tilde{\epsilon}_1(\mathrm{TeV}) = 1.96 \cdot 10^5\,\delta_1^{-1}$ in the comoving frame of the emission knot with a Doppler factor $\delta = 10\,\delta_1$. Consequently, the optical depth yields

$$\tau_{\gamma\gamma}(\tilde{\epsilon}_1(\mathrm{TeV})) \simeq 3.7 \cdot 10^{-4}\,\frac{\tau_{-2}\,L_{46}\,\theta_{-4}^{-1}\,\delta_1^2}{z_i/1\,\mathrm{pc}} \tag{F.9}$$

and thus the emission knot is optical thin for TeV energies at a distance
$z_i \gg 3.7 \cdot 10^{-4}\,\tau_{-2}\,L_{46}\,\theta_{-4}^{-1}\,\delta_1^2\,\mathrm{pc}$.
Finally, the optical depth due to the soft synchrotron photons of energy ϵ is examined. Here the calculations are constrained to the case of an instantaneous and monoenergetic electron injection, since the Chap. 4 showed that only with a total number of injected electrons of $Q \gg 10^{41}\,R_{15}^3\,q_{-4}$, which is obtained by assuming a finite injection duration $T \gg 1\,s$, the resulting synchrotron intensities of this case are exceeded. The synchrotron photon density at the radius r inside of the emission knot is determined by

$$n_{sy}(r,\epsilon,t) = \frac{2\pi}{c\,r}\int_0^R dr'\;r'\int_{|r-r'|}^{r+r'}\frac{ds}{s}\,\exp\left(-\frac{g(x)\,s}{R}\right)\,j_s(r',\epsilon,t-s/c) \tag{F.10}$$

and with the emission coefficient (4.22) one obtains

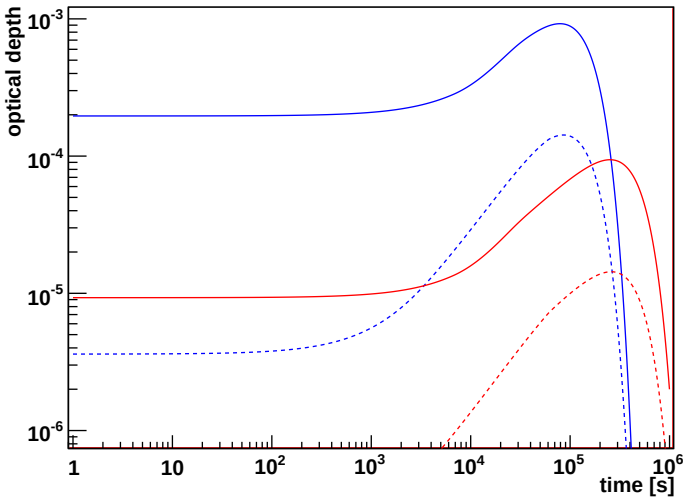

Figure F.1: The pair attenuation optical depth due to the low energy synchrotron radiation. Considered are gamma-rays with $\epsilon_1 = 1\,\mathrm{TeV}$ (blue lines) and $\epsilon_1 = 10\,\mathrm{TeV}$ (red lines), as well as the initial location $r = 0.1\,R$ (solid lines) and $r = 0.9\,R$ (dashed lines), respectively. Furthermore, $b^2 + l_{EC} = 1$, $\gamma_6 = 1$, $R_{15} = 1$ and $q_{-4} = 10^8$ is used.

$$
\begin{aligned}
n_{sy}(r,\epsilon,t) = & \frac{P_0\, q_0}{2\, c\, h\, r} \left(\frac{\epsilon}{E_0}\right)^{\frac{1}{3}} \exp\left(-\frac{\epsilon}{E_0}\,(1 + D_s \gamma_0 \tau)^2\right) \sum_{k=1}^{\infty} \frac{b_k}{\lambda_k} \exp\left(-\frac{g(x)\, r}{R} - \frac{c\, l_0\, \lambda_k^2}{3}\,\tau\right) \\
& \times H[t - t_0] \Bigg(H[c\tau - r] \int_{-r}^{r} dr'\, \cos(\lambda_k r')\, f_1(r', \epsilon, \tau) \\
& \quad + H[r - c\tau] \int_{-r}^{c\tau} dr'\, \cos(\lambda_k r')\, f_1(r', \epsilon, \tau) \\
& \quad - \cos(\lambda_k R)\, H[c\tau - R + 2r] \Big(H[c\tau - R] \int_{R-2r}^{R} dr'\, f_1(r', \epsilon, \tau) \\
& \qquad + H[R - c\tau] \int_{R-2r}^{c\tau} dr'\, f_1(r', \epsilon, \tau) \Big) \\
& \quad + H[c\tau - r] \Big(H[c\tau - R] \int_{r}^{R} dr'\, \cos(\lambda_k r')\, f_1(r', \epsilon, \tau) \\
& \qquad + H[R - c\tau] \int_{r}^{c\tau} dr'\, \cos(\lambda_k r')\, f_1(r', \epsilon, \tau) \Big) \\
& \quad - H[c\tau + 2r - R] \int_{r}^{R} dr'\, \cos(\lambda_k r')\, f_1(r' - 2r, \epsilon, \tau) \\
& \quad - H[R - 2r - c\tau] \int_{r}^{c\tau+2r} dr'\, \cos(\lambda_k r')\, f_1(r' - 2r, \epsilon, \tau) \Bigg)\,,
\end{aligned}
\tag{F.11}
$$

where

$$f_1(r', \epsilon, \tau) = \frac{(1 + D_s \gamma_0 (\tau - r'/c))^{\frac{2}{3}}}{r + r'} \exp(-A\, r'^2 + B_k(\tau)\, r') \,. \tag{F.12}$$

Using the approximation (F.3) the time dependent pair attenuation optical depth between r and R for a gamma-ray with the energy ϵ_1 is calculated by

$$\begin{aligned} \tau_{\gamma\gamma}(\epsilon_1, r, t) &= \int_R^r dr' \int_{-\infty}^{\infty} dt' \int_{2m_e c^2/\epsilon_1}^{\infty} d\epsilon\; \sigma_{\gamma\gamma}(\epsilon_1, \epsilon)\, n_{sy}(r', \epsilon, t')\, \delta(t - t' + |r' - r|/c) \\ &= \frac{2\,\sigma_T\, m_e c^2}{3\,\epsilon_1} \int_R^r dr'\, n_{sy}\left(r',\, 2m_e^2 c^4/\epsilon_1,\, t + (r' - r)/c\right) \,. \end{aligned} \tag{F.13}$$

Predominantly, the low energy synchrotron photons attenuate the TeV photons and in order to obtain the intrinsic optical luminosity $L_{opt} \simeq 10^{42.5}\, \delta_1^{-3}$ erg s^{-1} the corresponding photon density yields

$$n_{Sy}(R, \epsilon_{opt}, t_{max}) = \frac{L_{opt}}{4\,\pi\, R^2\, \epsilon_{opt}\, c} \simeq 5 \cdot 10^{12}\, (1\,\mathrm{eV}/\epsilon_{opt})\, R_{15}^{-2}\, \delta_1^{-3}\,\mathrm{cm}^{-3} \,. \tag{F.14}$$

The number of injected electrons is the main parameter that sets the amplitude of the synchrotron density and thus $Q \simeq 4.2 \cdot 10^{49}\, R_{15}^3$ is needed to realize the observed optical luminosity of PKS 2155-304. Using $q_0\, T \simeq 10^4\,\mathrm{cm}^{-3}\,\mathrm{s}$ the Fig. F.1 shows that the resulting optical depth (F.13) correlates to the synchrotron radiation of energy $\epsilon = 2m_e^2 c^4/\epsilon_1$ and has a energy dependent maximum several hours after the injection of relativistic electrons. However, the emission knot stays optical thin for TeV photons during the whole time of synchrotron emission when $q_0\, T \ll 10^7\,\mathrm{cm}^{-3}\,\mathrm{s}$.

List of Figures

List of Tables

Bibliography

The references are appearing in the alphabetic order of the abbreviations and thus not necessarily in the alphabetic order of the name of the first author.

Abbasi, R., et al. Limits on Neutrino Emission from Gamma-Ray Bursts with the 40 String IceCube Detector. *Physical Review Letters*, 106:141101, 2011a.

Abbasi, R., et al. Measurement of the atmospheric neutrino energy spectrum from 100 GeV to 400 TeV with IceCube. *Physical Review D*, 83:012001, 2011b.

Abbasi, R., et al. Time-integrated Searches for Point-like Sources of Neutrinos with the 40-string IceCube Detector. *Astrophysical Journal*, 732:18, 2011c.

Abdo, A. A., et al. Fermi Large Area Telescope Observations of Misaligned Active Galactic Nuclei. *Astrophysical Journal*, 720:912–922, 2010.

Abramowitz, M., & Stegun, I. A. *Pocketbook of Mathematical Functions.* Harri Deutsch, Frankfurt am Main, 1984.

Aharonian, F. A. TeV gamma rays from BL Lac objects due to synchrotron radiation of extremely high energy protons. *New Astronomy*, 5:377–395, 2000.

Aharonian, F. A., Akhperjanian, A. G., Anton, G., et al. Simultaneous multiwavelength observations of the second exceptional γ-ray flare of PKS 2155-304 in July 2006. *Astronomy & Astrophysics*, 502:749–770, 2009.

Aharonian, F. A., et al. An Exceptional Very High Energy Gamma-Ray Flare of PKS 2155-304. *Astrophysical Journal Letters*, 664:L71–L74, 2007.

Aharonian, F. A., et al. Discovery of Very High Energy γ-Ray Emission from Centaurus a with H.E.S.S. *Astrophysical Journal*, 695:L40–L44, 2009.

Albert, J., et al. Variable Very High Energy γ-Ray Emission from Markarian 501. *Astrophysical Journal*, 669:862–883, 2007.

Altarelli, G., & Winter, K., editor. *Neutrino Mass.* Springer, Berlin, 2003.

Antonucci, R. Unified Models for Active Galactic Nuclei and Quasars. *Annual Reviews in Astronomy and Astrophysics*, 31:473–521, 1993.

Argüelles, C. A., Bustamante, M., & Gago, A. M. IceCube expectations for two high-energy neutrino production models at active galactic nuclei. *Journal of Cosmology and Astroparticle Physics*, 12:5, 2010.

Becker, J. K. High-energy neutrinos in the context of multimessenger astrophysics. *Physical Reports*, 458:173–246, 2008.

Begelman, M. C., Blandford, R. D., &Rees, M. J. Theory of extragalactic radio sources. *Reviews of Modern Physics*, 56:255–351, 1984.

Bethe, H., &Heitler, W. On the Stopping of Fast Particles and on the Creation of Positive Electrons. *Proceedings of the Royal Society of London*, 146:83–112, 1934.

Blażejowski, M., et al. A Multiwavelength View of the TeV Blazar Markarian 421: Correlated Variability, Flaring, and Spectral Evolution. *Astrophysical Journal*, 630:130–141, 2005.

Blumenthal, G. R. Energy Loss of High-Energy Cosmic Rays in Pair-Producing Collisions with Ambient Photons. *Physical Review D*, 1:1596–1602, 1970.

Blumenthal, G. R., & Gould, R. J. Bremsstrahlung, Synchrotron Radiation, and Compton Scattering of High-Energy Electrons Traversing Dilute Gases. *Reviews of Modern Physics*, 42:237–271, 1970.

Böttcher, M. Modeling the emission processes in blazars. *Astrophysics and Space Science*, 309:95–104, 2007.

Böttcher, M., Reimer, A., & Marscher, A. P. Implications of the very High Energy Gamma-Ray Detection of the Quasar 3C279. *Astrophysical Journal*, 703:1168–1175, 2009.

Chodorowski, M. J., Zdziarski, A. A., & Sikora, M. Reaction rate and energy-loss rate for photopair production by relativistic nuclei. *Astrophysical Journal*, 400:181–185, 1992.

Compton, A. H. A Quantum Theory of the Scattering of X-Rays by Light Elements. *Physical Review*, 21:483–502, 1923.

Coppi, P. S. Time-dependent models of magnetized pair plasmas. *Monthly Notices of the Royal Astronomical Society*, 258:657–683, 1992.

Crusius, A., & Schlickeiser, R. Synchrotron radiation in random magnetic fields. *Astronomy & Astrophysics*, 164:L16–L18, 1986.

Crusius, A., & Schlickeiser, R. Synchrotron radiation in a thermal plasma with large-scale random magnetic fields. *Astronomy & Astrophysics*, 196:327–337, 1988.

Dermer, C., & Schlickeiser, R. On the location of the acceleration and emission sites in gamma-ray blazars. *Astrophysical Journal*, 90:945–948, 1994.

Dermer, C. D., & Menon, G. *High Energy Radiation from Black Holes: Gamma Rays, Cosmic Rays, and Neutrinos*. Princeton University Press, Princeton, 2009.

Dermer, C. D., & Schlickeiser, R. Model for the High-Energy Emission from Blazars. *Astrophysical Journal*, 416:458, 1993a.

Dermer, C. D., & Schlickeiser, R. Photon Attenuation from Scattered Radiation in Gamma-Ray Blazars. In *International Cosmic Ray Conference*, volume 1 of *International Cosmic Ray Conference*, page 156, 1993b.

Donnarumma, I., Pucella, G., Vittorini, V., et al. Multiwavelength Observations of 3C 454.3. II. The AGILE 2007 December Campaign. *Astrophysical Journal*, 707:1115–1123, 2009.

Eichmann, B. *Synchrotron- und Röntgenvariabilitäten von Blazaren*. Diplomarbeit, Ruhr-Universität Bochum, 2009.

Eidelman, S., et al. Review of Particle Physics. *Physics Letters B*, 592:1+, 2004.

Fabian, A. C., Guilbert, P. W., Blandford, R. D., Phinney, E. S., & Cuellar, L. Pair-induced spectral changes and variability in compact X-ray sources. *Monthly Notices of the Royal Astronomical Society*, 221:931–945, 1986.

Felten, J. E. and Morrison, P. Omnidirectional Inverse Compton and Synchrotron Radiation from Cosmic Distributions of Fast Electrons and Thermal Photons. *Astrophysical Journal*, 146:686, 1966.

Fermi, E. High Energy Nuclear Events. *Prog. Theor. Phys.*, 5:570–583, 1950.

Fossati, G., Maraschi, L., Celotti, A., Comastri, A., & Ghisellini, G. A unifying view of the spectral energy distributions of blazars. *Mon. Not. R. Astron. Soc.*, 299:433–448, 1998.

Fukugita, M., & Yanagida, T., editor. *Physics of Neutrinos an Applications to Astrophysics*. Springer, Berlin, 2003.

Gerbig, D., & Schlickeiser, R. Relativistic Pickup of Interstellar Neutrals by Hadronic Jets. *Astrophysical Journal*, 664:750–760, 2007.

Ghisellini, G., Celotti, A., Fossati, G., Maraschi, L., & Comastri, A. A theoretical unifying scheme for gamma-ray bright blazars. *Mon. Not. R. Astron. Soc.*, 301:451–468, 1998.

Ghisellini, G., Padovani, P., Celotti, A., & Maraschi, L. Relativistic Bulk Motion in Active Galactic Nuclei. *Astrophysical Journal*, 407:65–82, 1993.

Gould, R. J. Compton and synchrotron processes in spherically-symmetric non-thermal sources. *Astronomy & Astrophysics*, 76:306–311, 1979.

Guimarães, A. C. C., Cunha, J. V., & Lima, J. A. S. . Bayesian analysis and constraints on kinematic models from union SNIa. *Journal of Cosmology and Astroparticle Physics*, 10:10, 2009.

Hertz, H. *Die Constitution der Materie*. Springer, Berlin, 1999.

Homan, D. C. Polarization of AGN Jets. In J. Romney & M. Reid, editor, *Future Directions in High Resolution Astronomy*, volume 340 of *Astronomical Society of the Pacific Conference Series*, page 133, 2005.

Kelner, S. R., Aharonian, F. A., & Bugayov, V. V. Energy spectra of gamma rays, electrons, and neutrinos produced at proton-proton interactions in the very high energy regime. *Physical Review D*, 74(3), 2006.

Krawczynski, H., et al. Multiwavelength Observations of Strong Flares from the TeV Blazar 1ES 1959+650. *Astrophysical Journal*, 601:151–164, 2004.

Krolik, J. H. *Active galactic nuclei : from the central black hole to the galactic environment.* Princeton University Press, Princeton, 1999.

Lightman, A. P., & Zdziarski, A. A. Pair production and Compton scattering in compact sources and comparison to observations of active galactic nuclei. *Astrophysical Journal*, 319:643–661, 1987.

Longair, M. S. *High energy astrophysics. Vol.1: Particles, photons and their detection.* Cambridge University Press, Cambridge, 1992.

Mannheim, K., & Schlickeiser, R. Interactions of cosmic ray nuclei. *Astronomy & Astrophysics*, 286:983–996, 1994.

Medvedev, M. V. Theory of "Jitter" Radiation from Small-Scale Random Magnetic Fields and Prompt Emission from Gamma-Ray Burst Shocks. *Astrophysical Journal*, 540: 704–714, 2000.

Mücke, A., & Protheroe, R. J. A proton synchrotron blazar model for flaring in Markarian 501. *Astroparticle Physics*, 15:121–136, 2001.

Mücke, A., Protheroe, R. J., Engel, R., Rachen, J. P., & Stanev, T. BL Lac objects in the synchrotron proton blazar model. *Astroparticle Physics*, 18:593–613, 2003.

Pohl, M., & Schlickeiser, R. On the conversion of blast wave energy into radiation in active galactic nuclei and gamma-ray bursts. *Astronomy & Astrophysics*, 354:395–410, 2000.

Pohl, M., Schlickeiser, R., & Lerche, I. Longitudinal, electrostatic instabilities in the channeled blast wave model. *Proceedings of the 27th International Cosmic Ray Conference*, 2001.

Press, W. H., Teukolsky, S. A., Vetterling, W. T., & Flannery, B. P. *Numerical Recipes (Third Edition).* Cambridge University Press, New York, 2007.

Puget, J. L., Stecker, F. W., & Bredekamp, J. H. Photonuclear interactions of ultrahigh energy cosmic rays and their astrophysical consequences. *Astrophysical Journal*, 205: 638–654, 1976.

Schlickeiser, R. *Cosmic Ray Astrophysics.* Springer, Berlin, 2002.

Schlickeiser, R., & Crusius, A. On the influence of a thermal plasma on the energy loss rates of single relativistic electrons and the formation of electron energy spectra in cosmic radio sources. *Astrophysical Journal*, 328:578–587, 1988.

Schlickeiser, R., & Lerche, I. Nonlinear cooling of relativistic particles under equipartition conditions. II. Instantaneous power law injection. *Astronomy & Astrophysics*, 485:315–325, 2008.

Schlickeiser, R., & Röken, C. Synchrotron self-Compton flaring of TeV blazars. I. Linear electron cooling. *Astronomy & Astrophysics*, 477:701–715, 2008.

Schlickeiser, R., Böttcher, M., & Menzler, U. Combined synchrotron and nonlinear synchrotron-self-Compton cooling of relativistic electrons. *Astronomy & Astrophysics*, 519:A9, 2010.

Schmidt, M. 3C 273: A star-like object with large red-shift. *Nature*, 197:1040, 1963.

Schneider, P. *Einführung in die Extragalaktische Astronomie und Kosmologie*. Springer, Berlin Heidelberg, 2006.

Seyfert, C. K. Nuclear Emission in Spiral Nebulae. *Astrophysical Journal*, 97:28, 1943.

Sikora, M., Begelman, M. C., & Rees, M. J. Comptonization of diffuse ambient radiation by a relativistic jet: The source of gamma rays from blazars? *Astrophysical Journal*, 421:153–163, 1994.

Sikora, M., Kirk, J. G., Begelman, M. C., & Schneider, P. Electron injection by relativistic protons in active galactic nuclei. *Astrophysical Journal*, 320:L81–L85, 1987.

Soler Gil, Francisco José. *Discovery or construction? Astroparticle Physics and the search for physical reality*. Peter Lang, Frankfurt am Main, 2012.

Sunyaev, R. A., & Titarchuk, L. G. Comptonization of X-rays in plasma clouds - Typical radiation spectra. *Astronomy & Astrophysics*, 86:121–138, 1980.

The Pierre Auger Collaboration. The Pierre Auger Observatory I: The Cosmic Ray Energy Spectrum and Related Measurements. *ArXiv e-prints:1107.4809*, 2011.

Turner, M. S., et al. *Connecting quarks with the cosmos: eleven science questions for the new century*. National Academies Press, Washington, D.C., 2003.

Urry, P., & Padovani, P. Unified Schemes for Radio-Loud Active Galactic Nuclei. *Publications of the Astronomical Society of the Pacific*, 107:803–845, 1995.

Vainio, R., Pohl, M., & Schlickeiser, R. Conversion of bulk kinetic energy into radiation in AGNs and GRBs: Particle transport effects. *Astronomy & Astrophysics*, 414:463–474, 2004.

Vercellone, S., D'Ammando, F., Vittorini, V., et al. Multiwavelength Observations of 3C 454.3. III. Eighteen Months of Agile Monitoring of the "Crazy Diamond". *Astrophysical Journal*, 712:405–420, 2010.

Visser, M. Jerk, snap and the cosmological equation of state. *Classical and Quantum Gravity*, 21:2603–2615, 2004.

Voigt, H.-H., et al. *Landolt-Börnstein: Numerical Data and Functional Relationships in Science and Technology.* Springer, 1999.

Wagner, W. *Design and Realisation of a new AMANDA Data Aquisition System with Transient Waveform Recorders.* Phd thesis, Technische Universität Dortmund, 2004.

Zacharias, M., & Schlickeiser, R. Blazar synchrotron emission of instantaneously power-law injected electrons under linear synchrotron, non-linear SSC, and combined synchrotron-SSC cooling. *Astronomy & Astrophysics*, 524:A31, 2010.

Zdziarski, A. A., & Lightman, A. P. Nonthermal electron-positron pair production and the 'universal' X-ray spectrum of active galactic nuclei. *Astrophysical Journal*, 294: L79–L83, 1985.

Zhang, Y.-W., & Fan, J.-H. Statistics of Superluminal Motion in Active Galactic Nuclei. *Chinese Journal of Astronomy and Astrophysics*, 8:385–394, 2008.

Acknowledgment/ Danksagung

An dieser Stelle möchte ich mich bei allen bedanken, die durch ihre direkte oder indirekte Unterstützung einen wesentlichen Beitrag zu dieser Arbeit geleistet haben:

- Einen herzlichen Dank an PROF. DR. DR. WOLFGANG RHODE für die Ermöglichung dieser Arbeit, wie auch die vielen Möglichkeiten und Freiheiten während meines Promotionsstudiums. Desweiteren hatte er in jeglichen Belangen immer ein offenes Ohr für mich und konnte mir einen umfangreichen Einblick in die Welt der experimentellen Astroteilchenphysik vermitteln.
- Ebenso möchte ich meinen Dank an PROF. DR. REINHARD SCHLICKEISER zum Ausdruck bringen für seine zahlreichen fachlichen, wie menschlichen Hilfestellungen und seine kompetente Betreuung mit vielen anregenden Gesprächen seit dem Beginn meiner Diplomarbeit.
- Zudem danke ich der gesamten Arbeitsgruppe E5b für die vielen kleinen und großen Dinge, die eine äußerst angenehme Arbeitsatmosphäre geschaffen haben.
- Insbesondere möchte ich DR. MICHAEL BACKES, MALWINA UELLENBECK, MARLENE DOERT sowie FREDERIC EFFENBERGER von TP4 danken für die vielen interessanten (Fach-) Gespräche und das Korrektur lesen dieser Arbeit.
- Nicht zuletzt gilt mein Dank auch meiner Familie sowie meinen Freunden und meiner Freundin, die die außerfachlichen Grundlagen für diese Arbeit gelegt haben.